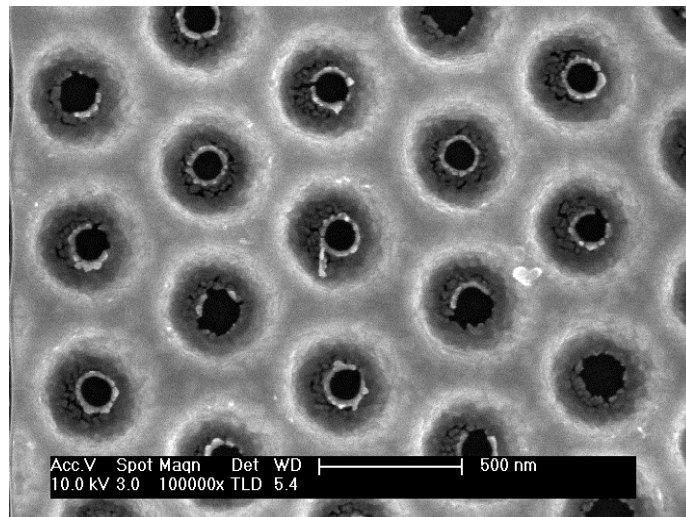


UNIVERSIDAD AUTÓNOMA DE MADRID
Departamento de Física Aplicada

FABRICATION OF 2D COLLOIDAL CRYSTALS OVER
LARGE AREAS FOR BIOSENSING



Memoria presentada por: Paola PELLACANI

Para optar al grado de: DOCTOR

Directores: Prof. Miguel MANSO SILVÁN

Prof. Franco MARABELLI

Madrid, Junio 2017

ACKNOWLEDGMENTS

Once upon a time there was a thesis...and many persons to thank for having contributed in different manners to its realization and although the question is still open, during these years everyone has helped to clarify a little bit more what I wanted “to be or not be” ...

First of all, I would like to thank Prof. Miguel Manso Silván, for giving me the opportunity to work in his lab at Universidad Autónoma de Madrid, for inspiring me with his passion for science, for motivating and supporting me in a lot of situations also outside the working environment. Thanks Miguel, I am really grateful!

I would also like to acknowledge Prof. Franco Marabelli, for his scientific support in co-supervising this thesis and for giving me the possibility to collaborate with Plasmore Srl (Italy). Having experience within the industrial field has been an additional value for my growth as a researcher. Thanks to the other people who worked at Plasmore in different periods: Dr. Andrea Valesia, for being my mentor at the beginning of my career and for introducing me to the fascinating world of colloidal lithography; Dr. Laura Ceriotti, Dr. Gerardo Marchesini and Dr. Francesca Carpignano for their help in the lab and the interesting discussions. A special thanks to Ana Frangolho (the best colleague ever!) and Laura Lopez...it was great to work in the same team!

Thanks also to Dr. Silvia Giudicatti and Dr. Lucia Fornasari from the University of Pavia (Italy) for their technical help with reflectance measurements and SPR experiments.

Thanks to Dr. Francois Rossi and Dr. Pascal Colpo for hosting me at the Nanobiotechnology Laboratory of the Joint Research Centre (Italy), it was a great opportunity to learn a lot. Thanks also to the people from their group for sharing nice moments over these years. Special thanks to Paula Caldeira for her friendship and administrative support, Giovanni Maselli for the technical help, Dr. Jan Hanus for teaching me the basics of ellipsometry and plasma processes, Dr. Radek Bombera for his continuous help in the lab and for making me smile even on bad days, Dr. Giacomo Ceccone and Dr. Valentina Spampinato for the XPS measurements.

Thanks to Dr. Vicente Torres Costa from UAM, for his help in the lab and for teaching me the basics of porous silicon and laser irradiation. Thanks to Luis García Pelayo, for his continuous help in small and big things in the lab and, of course, for the Spanish lessons (aunque me siga costando utilizar correctamente “por” y “para” ...).

Thanks to Dr. Manuel Rodriguez from IMDEA for his support (and patience) in the clean room and for the Italian-Spanish exchange moments. Thanks to Dr. Carmen Morant Zacaes y Dr. Beatriz Hernández Juárez for giving me the possibility to use the Langmuir Blodgett equipment at UAM. Thanks to Isi Poveda from SIDL for the SEM images.

Thanks to the people from the group of Dr. Furio Gramatica at Labion-Fondazione Don Carlo Gnocchi Onlus (Italy), especially to Dr. Carlo Morasso, Dr. Dora Mehn and Silvia Picciolini for their high level of competence with SERS experiments.

Thanks to my colleagues at UAM, for the lunches and the nice time spent chatting together: Esther, Chloé, Arancha, Darío, Sergio, Edu, Dani, Rosalía. A special thanks to Esther (and her family) for making great and more comfortable my stay in Madrid.

Thanks also to the people involved in the Thinface project, it was a great opportunity to improve my knowledge in a stimulating multicultural network.

I would also like to acknowledge the external international reviewers: Dr. Dora Mehn (Joint Research Centre, Ispra, Italy), Dr. Morten Madsen (University of Southern Denmark, Sonderborg, Denmark) and Dr. Emmanuelle Lacaze (Université Pierre et Marie Curie, Paris, France) for giving me the possibility to apply for the international PhD degree with their evaluations.

Grazie ai miei amici (troppi per nominarli tutti senza rischiare di dimenticare qualcuno!), per il loro sostegno ed interessamento anche quando le distanze ci separavano.

E alla fine...il grazie piú grande e importante va alla mia famiglia. A mia sorella e a mio papá, per la loro presenza discreta, ma costante, per l'aiuto nelle questioni logistiche e per avermi sempre sostenuta nelle mie scelte. A mia mamma, per esserci sempre e comunque, anche se non fisicamente. A GB, per la forza e l'entusiasmo con cui condivide il mio cammino, rendendolo meraviglioso. A Pietro, il miglior risultato che avrei mai potuto desiderare, che con la tenerezza delle sue manine e dei suoi sorrisi illumina le mie giornate.

*Alla mia famiglia
A me stessa, per averci creduto nonostante tutto*

...PER ASPERA AD ASTRA...

ACKNOWLEDGMENTS	III
LIST OF ACRONYMS	IX
ABSTRACT	XI
RESUMEN	XIII
CHAPTER 1 INTRODUCTION	15
1.1 NANOSTRUCTURED PLASMONIC SURFACES	15
1.1.1 <i>Introduction to plasmonics.....</i>	<i>15</i>
1.1.2 <i>Plasmonic based biosensing.....</i>	<i>17</i>
1.1.3 <i>Plasmonic nanohole arrays</i>	<i>18</i>
1.2 NANOFABRICATION TECHNIQUES.....	19
1.2.1 <i>Overview on nanofabrication</i>	<i>19</i>
1.2.2 <i>Fabrication based on colloidal crystal monolayers</i>	<i>20</i>
1.2.3 <i>Langmuir-Blodgett monolayers.....</i>	<i>21</i>
1.3 THESIS MOTIVATION, OBJECTIVES AND OUTLINE.....	22
1.3.1 <i>Motivation and objectives.....</i>	<i>22</i>
1.3.2 <i>Thesis outline.....</i>	<i>23</i>
CHAPTER 2 EXPERIMENTAL METHODS.....	25
2.1 NANOFABRICATION PROCESS	25
2.1.1 <i>Polymeric layer deposition</i>	<i>26</i>
2.1.2 <i>Langmuir Blodgett technique</i>	<i>29</i>
2.1.3 <i>Reactive ion etching</i>	<i>32</i>
2.1.4 <i>Gold deposition</i>	<i>34</i>
2.2 2D COLLOIDAL CRYSTAL CHARACTERIZATION	36
2.2.1 <i>Crystal domains and surface analysis</i>	<i>36</i>
2.2.2 <i>Optical analysis</i>	<i>45</i>
2.3 BIOSENSING TECHNIQUES.....	48
2.3.1 <i>Imaging Nanoplasmonics.....</i>	<i>48</i>
2.3.2 <i>Surface Enhanced Raman Spectroscopy.....</i>	<i>50</i>
CHAPTER 3 COLLOIDAL MONOLAYER DEVELOPMENT	53
3.1 ISOTHERM CURVE OPTIMIZATION	54
3.1.1 <i>Suspension related parameters.....</i>	<i>57</i>
3.1.2 <i>Different particle size</i>	<i>60</i>
3.2 CONTROL OVER PARTICLE ORGANIZATION.....	61

3.2.1	<i>Subphase pH</i>	61
3.2.2	<i>Subphase temperature</i>	65
3.2.4	<i>Inorganic particle monolayers</i>	74
3.3	CONCLUSIONS	79
CHAPTER 4 PLASMONIC SURFACE PROCESSING		81
4.1	DIFFERENT COLLOIDAL MONOLAYERS AS SACRIFICIAL MASKS	81
4.1.1	<i>Pitch investigation</i>	81
4.1.2	<i>Colloidal monolayers at different pH</i>	83
4.2	INFLUENCE OF THE ETCHING PROCESS.....	85
4.2.1	<i>Polymer pillars</i>	85
4.2.2	<i>SiO₂ particles and silicon pillars</i>	89
4.3	THE EFFECT OF POLYMER AND GOLD LAYERS.....	92
4.3.1	<i>Influence of polymer thickness</i>	92
4.3.2	<i>Comparison of different polymer substrates</i>	93
4.3.3	<i>Investigation of surface post-treatments</i>	98
4.3.4	<i>Study of different gold deposition methods</i>	105
4.4	CONCLUSIONS	109
CHAPTER 5 APPLICATION OF PLASMONIC SURFACES		111
5.1	SPR IMAGING APPLICATION	111
5.1.1	<i>Chip characterization</i>	111
5.1.2	<i>iNPx characterization</i>	114
5.1.3	<i>Diagnostic assay</i>	115
5.2	SERS APPLICATION	117
5.2.1	<i>Surface optimization</i>	117
5.2.2	<i>DNA recognition and microarray assay</i>	120
5.3	CONCLUSIONS	124
CHAPTER 6 CONCLUSIONS AND PERSPECTIVES		127
6.1	GENERAL CONCLUSIONS	127
6.2	FUTURE PERSPECTIVES.....	130
6.3	CONCLUSIONES GENERALES	132
REFERENCES		137

LIST OF ACRONYMS

AFM	Atomic Force Microscopy
CA	Contact Angle
CL	Colloidal lithography
CVD	Chemical Vapour Deposition
EtOH	Ethanol
FT	Fourier Transform
HCP	Hexagonal close packed
iNPx	Imaging Nanoplasmonics
IPA	Isopropanol
JRC	Joint Research Centre
LB	Langmuir Blodgett
LSPR	Localized Surface Plasmon Resonance
MeOH	Methanol
MSD	Magnetron Sputtering Deposition
PE-CVD	Plasma Enhanced Chemical Vapour Deposition
PFOS	Perfluoro octyl triethoxysilane
PMMA	Polymethyl methacrylate
ppAA	plasma polymerized Acrylic Acid
PS	Polystyrene
PVD	Physical Vapour Deposition
RIE	Reactive Ion Etching
RIU	Refractive Index Unit
SEM	Scanning Electron Microscopy
SERS	Surface Enhanced Raman Scattering
SP	Surface Pressure
SPM	Scanning Probe Microscopy
SPP	Surface Plasmon Polariton
SPR	Surface Plasmon Resonance
TE	Thermal Evaporation
UAM	Universidad Autónoma de Madrid
WCA	Water Contact Angle
XPS	X-rays Photoelectron Spectroscopy
CMOS	Complementary metal-oxide semiconductor

ABSTRACT

Surface plasmon resonance (SPR)-devices are widely applied as biosensing platforms to perform a potentially sensitive, rapid, real time, label free and/or multiplexed detection. As a drawback, this technology is often challenged by high instrumentation costs, poor interfacing capabilities with other analytical techniques and a lack of sensitivity when applied to direct detection of highly diluted targets or analytes of small molecular weight. In order to overcome these challenges, an extensive research has addressed the development of advanced SPR platforms based on innovative nanomaterials and fabrication methods, enabling a low cost and massive production of large area nanostructured surfaces, as well as affordable miniaturized detection devices.

In this thesis we report the optimization of a protocol for the production of large area plasmonic surfaces. The proposed nanofabrication technique combines colloidal lithography and plasma processes. In particular, we deeply studied the Langmuir-Blodgett formation of colloidal monolayers, acting as efficient etching masks when transferred on solid substrates. The sequential etching process, gold deposition and particle lift off allowed obtaining a surface made of 2D plasmonic crystals. By adjusting the process parameters it is possible to nanostructure different materials, leading to a fine tuning of the final structure aspect ratio and, consequently, of the spectral position of the optical response according to a proper acquisition setup. The versatility of this fabrication method shows great potential for easy and massive parallel fabrication of gold cavity arrays with a tailorable shape, diameter and periodicity. These surfaces have been proved to work as sensitive platforms in SPR and SERS experiments for a fast, real time and multiplexing detection of proteomic (long pentraxin PTX3) and genomic (Wilms tumor gene) biomarkers.

RESUMEN

Los dispositivos basados en la Resonancia de Plasmón Superficial se aplican extensamente como biosensores para identificar distintas biomoléculas de manera sensible, rápida, en tiempo real, libre de marcadores y/o con la posibilidad de multidetección. Actualmente, los desafíos al desarrollo de este tipo de dispositivos se encuentran en los altos costes de la instrumentación empleada, la limitada capacidad de conectar otras técnicas analíticas y una carencia de sensibilidad cuando se aplican a la detección de analitos muy diluidos o con pequeño peso molecular. Con el fin de vencer estos desafíos, se ha dirigido una extensa investigación al desarrollo de plataformas SPR avanzadas, basadas en materiales innovadores y métodos de fabricación que permiten una producción económica y masiva de grandes superficies nanoestructuradas, así como de dispositivos miniaturizados y de bajo coste.

En este trabajo de tesis se ha llevado a cabo la optimización de un proceso para la producción de superficies plasmónicas sobre grandes áreas. La técnica de nanofabricación propuesta combina litografía coloidal y procesos plasma. En particular, hemos estudiado en detalle la formación de monocapas coloidales según el método Langmuir-Blodgett, sirviendo de máscaras para crear nanoestructuras en sustratos sólidos. El proceso implica un ataque plasma, la deposición de oro y la eliminación del residuo coloidal para obtener una superficie que consiste en cristales plasmónicos bidimensionales. Ajustando los parámetros del proceso es posible diseñar estructuras en materiales diferentes, controlando con precisión la relación de aspecto de la estructura final y, por consiguiente, la posición espectral de la respuesta óptica de acuerdo con el sistema de adquisición apropiado. La versatilidad de este método de fabricación ofrece gran potencial para un eficiente, fácil y masivo desarrollo de cavidades de oro con forma, diámetro y periodicidad controlables. Finalmente, se ha demostrado que estas superficies trabajan como plataformas eficaces en experimentos de SPR y SERS para una detección rápida, de tiempo real y sensible de distintos analitos protéicos (como la proteína pentraxin PTX3) y genómicos (como el gen del tumor de Wilms).

CHAPTER 1

INTRODUCTION

In the last decades, biosensors have achieved an important role in several fields such as medical diagnostics, drug screening, food safety, environmental monitoring and security. Biosensor technologies are commonly based on the interaction of a target molecule (analyte) with a biomolecular receptor, one of which is bound to the surface of a transducer. Depending on the method of detection of the analyte, they can be categorized, in the most common groups, as optical, electrochemical or mechanical based sensors. The use of micro and nano-technologies has allowed the micro and nanoscale patterning of surfaces, leading to the miniaturization and integration of sensing devices, as relevant physico-chemical contributions to the improvement of their properties. In this framework, nanostructured plasmonic surfaces, made possible through combined nanofabrication techniques, have appeared as powerful tools to perform highly sensitive real-time and multiplexing monitoring of various biological and chemical interactions.

1.1 NANOSTRUCTURED PLASMONIC SURFACES

1.1.1 INTRODUCTION TO PLASMONICS

Plasmonics is a sub-field of nano-photonics and relies on interaction processes between electromagnetic waves and conduction electrons at metallic interfaces or in metallic nanostructures, leading to an enhanced optical near field of sub-wavelength dimension [1-3]. In fact, at enough high electromagnetic frequencies and/or small material scale, even structures with high electronic densities get polarized, which lead to define the resulting surface waves (plasmons) as surface plasmon polaritons. From a practical point of view, there is a growing interest in plasmonics related to its numerous potential applications, ranging from optoelectronics to food safety, environmental monitoring, medical diagnostics and therapeutics [4-14]. Novel developing technologies include the use of plasmonic materials for photovoltaic cell development [15-19] and other energy applications [20].

The field of plasmonics includes a series of phenomena that is convenient to appropriately categorize. The collective oscillations of electrons in the conduction band of bulk metals, as excited by an oscillating electromagnetic field (light), are insensitive to the surrounding medium [7] and are thus of no applicability in the bio sensing area. On the other hand, surface plasmon resonances (SPR) are defined as coherent oscillations of conduction electrons on a metal surface, excited by the electromagnetic radiation at metal-dielectric interface, which can concentrate electromagnetic fields on the nanoscale, while enhancing local field strengths by several orders of magnitude [21]. These SPRs can be ascribed to two main modes: surface plasmon polaritons (SPPs) are propagating, dispersive electromagnetic waves coupled to the free electrons of a conductor at a dielectric interface. Localized surface plasmon resonances (LSPRs) are non-propagating excitations of the conduction electrons of metallic nanostructures coupled to the electromagnetic field. Size, shape, composition and local dielectric environment are important parameters to define in order to set spectral position and magnitude of the LSPR. Normally, SPP can propagate along the metal surface with an associated electric field that decays exponentially from the surface (normal to the dielectric-metal interface) with a decay length on the order of hundreds nm, while LSPRs can exhibit a small decay length on the order of tens of nm [22, 23]. Since surface plasmons cannot propagate freely if the structure is smaller than the distance of propagation, the properties of the surface plasmon strongly depend on the structure dimensions [3, 7, 24-26]. Metal nanoparticles and nanostructured thin metal films (with dimensions much smaller than the wavelength of light) can be resonantly excited with visible light due to the presence of a LSPR (Figure 1.1).

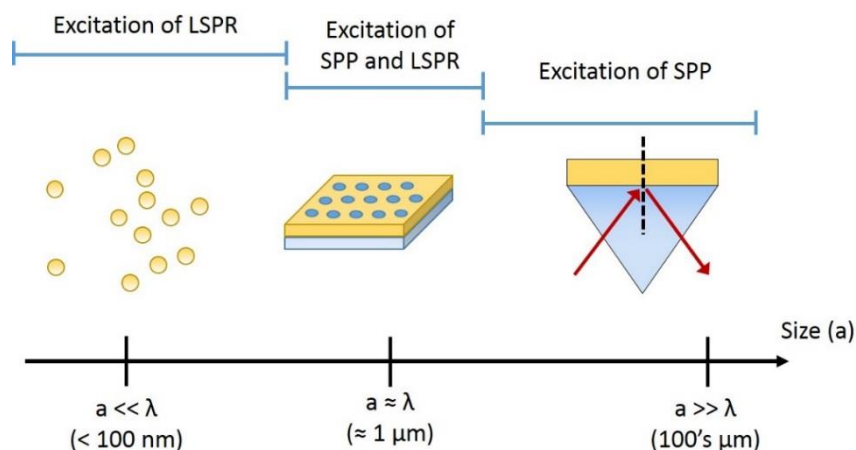


Figure 1. 1 – Optical properties of surface plasmons in relation with structure dimensions. Macroscopic thin films support SPPs. Metallic nanoparticles and nanomaterials of sub-wavelength dimension support LSPRs. Nanostructures with length scale comparable with the wavelength of light can support both SPP and LSPR. Adapted from [7].

In the case of macroscopic material, with bigger dimensions than the wavelength of light, surface plasmons cannot be directly excited and coupling through total internal reflection in a prism (Kretschmann configuration) or by exciting the surface plasmon on a metallized grating is required (Figure 1.1). A recent class of materials (e.g., nanovoid and nanohole arrays), with a length scale similar to the wavelength of light, is able to support both SPP and LSPR (Figure 1.1). The sensitivity of these structures to environmental changes within the electromagnetic near field, makes them particularly promising for sensing applications.

1.1.2 PLASMONIC BASED BIOSENSING

The greatest challenge in quantitative clinical bio-analysis is the development of label-free methods for biomolecular analysis, based upon the measurement of an inherent molecular property (e.g. refractive index). Furthermore, these methods should allow the real time detection of the biomolecular events occurring on the sensor surface in terms of kinetic and affinity information [27]. If this can be combined with a proper patterning of the surface, multiplexing can become an additional value [6, 28-31]. Among others, SPR is a promising label-free technique for probing chemical, biological and physical processes occurring on the free surface of a plasmonic material [5, 7, 10-12, 14, 28, 32-46], as well as to integrate complementary analytical techniques such as surface enhanced spectroscopy [4, 22, 47, 48]. The detection principle is based on a shift of the plasmon resonances (typically read as a change in the plasmonic wavelength or the excitation angle) due to a change in the refractive index, whether due to bulk or binding events, within the penetration depth of the decaying plasmonic field.

Plasmonic crystals (also named plasmonic metamaterials) are two-dimensional plasmonic surfaces characterized by a tight field confinement to the metal surface, which allows one to manipulate the surface plasmon in the surface plane by using different types of surface metal nanostructures [14, 26, 32, 49-53]. Indeed, the properties and performances of a plasmonic crystal strongly depend on the spacing, composition, size and shape of the employed materials, as well as on the fabrication method used. Gold and silver are the most often used metals at optical frequencies in the visible and NIR ranges, but gold is normally preferred due to its higher stability towards oxidation and environmental conditions. The phenomena in the visible and near infrared range can be however studied on other metals and semiconductors [48], with extension to the UV range if studied on aluminum, nickel and zinc. In general, a suitable manufacturing procedure for real device applications should merge simplicity of usage and flexibility for various designs [49]. Colloidal lithography is a particularly versatile fabrication technique useful to achieve a fast, robust and massive production of plasmonic components with nanoscale features.

A typical SPR biosensor requires not only a highly sensitive plasmonic material, but also an instrument specifically designed to probe it and a controlled surface chemistry capable of immobilizing a molecular receptor to detect the target analyte [3, 39, 54]. The binding between receptor and analyte causes a small change in the local refractive index and results in a real-time SPR signal, which provides biomolecular information such as binding kinetics, association and dissociation constants and the concentration of the analyte. Nowadays, there is a variety of commercial SPR instruments, ranging from laboratory SPR instruments, passing through portable miniaturized SPR devices and reaching high throughput SPR imaging systems [3, 7, 26, 35, 54-56]. These can be further coupled to orthogonal analytical techniques (e.g., Raman, infrared, fluorescence or mass spectrometry). Indeed, a huge interest is addressed to nanostructured plasmonic surfaces as biosensing platforms, coupling investigation of binding and detection of selected and specific targets with improved nanofabrication techniques, in order to obtain miniaturized devices for high performance applications [49, 57].

1.1.3 PLASMONIC NANOHOLE ARRAYS

Since the discovery made by Ebbesen and co-workers [58], regarding the enhanced transmission of light through periodic arrays of sub-wavelength holes in metal films, attributed to surface plasmons, one of the most applied structures in plasmonics is made of periodic arrays of holes in an opaque metal film [59-67]. Its main advantage relates to the simplicity in tuning and adjusting the spectral properties according to the structural parameters of the holes in the array, as well as to the metal layer properties and the grating coupling conditions [60, 64, 68-74]. Indeed, symmetry of the structure, shape, dimensions and spacing of the holes and profile of the corrugations around the apertures, are important parameters which can affect the spectral response. All these parameters influence the electromagnetic field distribution on the surface, the propagation dynamics of the surface waves, their scattering efficiencies and coupling to light. Moreover, since the dielectric constants of metals are wavelength dependent, it is important to select the proper metal working at the desired wavelength. Ideally, the dielectric constant of the metal should have a large negative value for the real part and a small imaginary part that determines the absorption in the metal in order to maximize the surface plasmon fields and minimize losses. Moreover, the quality of the metal layer is an important parameter which has to be controlled to optimize the optical properties of the final structure.

1.2 NANOFABRICATION TECHNIQUES

1.2.1 OVERVIEW ON NANOFABRICATION

Nanofabrication techniques, basically relate to two main approaches: “top-down” and “bottom-up” [75-79]. In the top-down approach, lithography methods are used to scale down thin films or bulk materials to create nanodevices, by means of “parallel writing” methods (e.g., optical lithography) and “sequential writing” methods (e.g., scanning beam lithography). These methods offer good control and resolution over the reproduced features, but they are mainly carried out in clean room environments and are limited by the process cost and incompatible with configurations out of the standard (e.g., coatings on not planar surfaces). To overcome these disadvantages, many alternative lithographic and patterning techniques have been proposed: the soft lithography collects a set of methods (microcontact printing, replica molding, microtransfer molding, etc.) for generating or replicating structures by using a patterned elastomer as a mask, stamp, or mold. Moreover, soft lithography paves the possibility to nanostructure a wide range of materials, on curved or planar surfaces, but it is not well suited for fabricating structures with multiple layers that must stack precisely one on top of the other and requires the assistance of conventional lithographic techniques to design and manufacture the masks or masters. Scanning probe techniques are another potential tool for nanofabrication, based on the changes undergone by species present on the surface of a substrate and with a resolution dependent on the sharpness of the pen. However, they are too slow for mass production. On the other hand, bottom-up approach refers to cheap and efficient methods to obtain complex structures by means of self-assembly of small and simple building blocks (atoms, molecules, particles, etc.). Self-assembly involves the spontaneous organization of several components into larger aggregates using covalent and/or noncovalent interactions at controlled thermodynamic conditions. These techniques can fabricate structures reaching sub-10 nm dimensions, but they also show several disadvantages, such as limited regularity, difficult repeatability, as well as a restricted control of precise spatial positioning and assembling shape. Figure 1.2 shows the evolution over the last years of top down and bottom up methods, in terms of achievable dimension scale [80]. The comparable scale order reached by either approaches makes particularly interesting their potential combination into hybrid methods in order to overcome the issues of each single technique and obtain the desired structural, mechanical, optical, magnetic or electronic properties with a high level of precision. Innovative nanofabrication technologies are particularly promising in the field of nano-medicine for point-of-care applications and for the development of advanced functional materials with tunable properties, sensors, surfaces with controlled properties and optics [77].

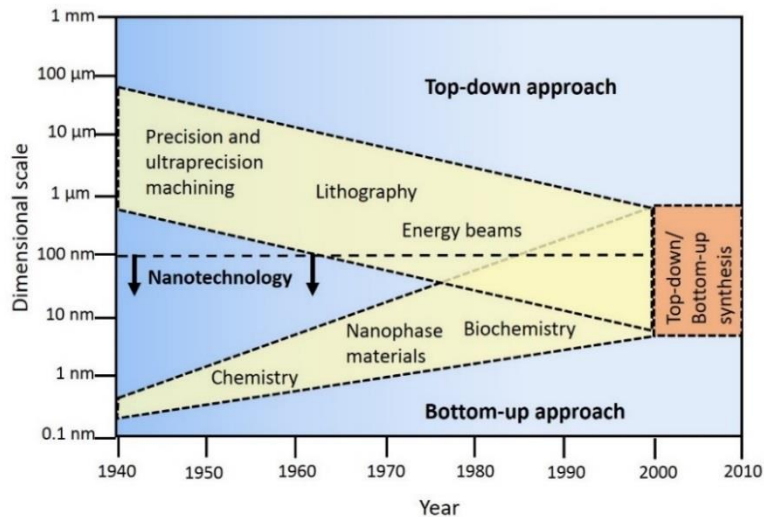


Figure 1. 2 - Progression of top down and bottom up techniques [80]. Reprinted with permission from Ingenia online.

1.2.2 FABRICATION BASED ON COLLOIDAL CRYSTAL MONOLAYERS

In addition to the classical fabrication approaches, the development of hybrid top-down/bottom-up techniques can allow a fast, parallel and low cost fabrication of large area surface patterns [4, 79, 81]. Among these techniques, colloidal lithography (CL, also called nanosphere or natural lithography) is a facile and cost effective method based on colloidal monolayers to obtain controllable and repeatable surface patterns with structural features down to the sub-100 nm resolution [75, 82-85]. CL is based on the deposition of mono or double layers of micro and nanoparticles (either organic, e.g. polystyrene, or inorganic, e.g. silica) serving as a sacrificial mask in a further deposition or etching processes [81, 86-89]. The properties of the final nanostructures depend on the colloidal particle size, inter-particle distance, ordering and the overall colloidal film size. Large size particles will increase the lattice period, and in turn, weaken the advantage of the nanofabrication method, while small size particles will increase the difficulty of colloidal preparation and assembly processes. Self-assembled 2D colloidal crystals are mostly hexagonal close packed (HCP), because this structure provides the minimum surface free energy (also referred as Gibbs surface free energy) and defines the most stable positions. Non-close-packed colloidal crystals can also be prepared by etching on HCP template or by directly setting proper assembly environments and conditions [82, 90-92].

In addition to the CL monolayer parameters, the resulting final nanostructure also depends on the further modification processes [82, 93-95] (Figure 1.3). Using 2D colloidal crystals as masks for etching process, it is possible to obtain non-close packed template (Figure 1.3, top) with conserved pitch to fabricate nanodisks, nanotips or nanopillars on polymeric or semiconductor

substrates. By deposition or imprinting with nanospheres as molds, ordered arrays of spherical voids have been fabricated on metal, semiconductor, or polymer thin films. Through dewetting around nanospheres, nanorings of polymers, carbon nanotubes or nanoparticles can be obtained. On the other hand, using 2D colloidal crystals as template during evaporation of metals, honeycomb arrays (Figure 1.2 b-d) of triangular nanoparticles can be synthesized, which can evolve into roundish nanoparticles if a thermal treatment is introduced. Moreover, these metallic nanoparticles can act as catalysts to grow nanorods. Honeycomb arrays of nanorings can also be obtained by rotating the colloidal mask during the evaporation process. In addition, various deposition techniques and wet-chemical strategies can lead to hexagonally arranged nanostructures (Figure 1.2 e-l), such as bowl arrays, nanodots, nanopillars arrays, hollow sphere arrays, nanorings and nanocrescents.

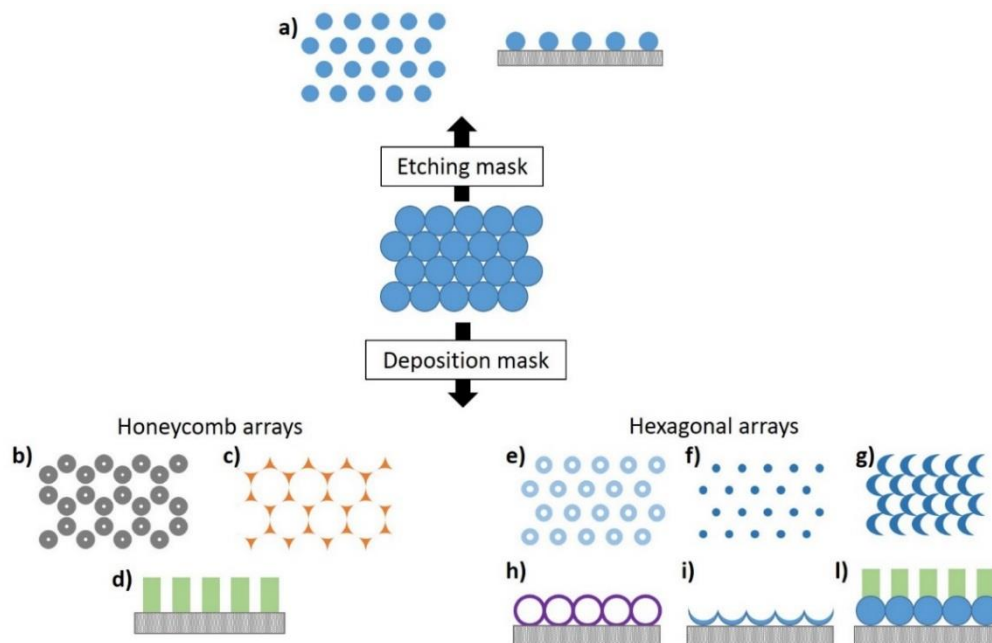


Figure 1. 3 – Examples of hexagonal close packed colloidal monolayers as etching (top) and deposition (bottom) masks. Etching conditioning leads to non-close packed template (a). Deposition process allow obtaining honeycomb arrays of nanorings (b), nanoparticles (c), nanopillars (d) or hexagonal arrays of nanorings (e), nanodots (f), nanocrescents (g), hollow spheres (h), bowls (i) and nanopillars (l). Adapted from [82].

1.2.3 LANGMUIR-BLODGETT MONOLAYERS

Different protocols have been proposed to develop colloidal crystal monolayers at low cost and with high structural control, reproducibility and low defect density on different substrate types, by investigating, both experimentally and theoretically, the nucleation of 2D crystals as well as the driving forces for the crystallization process [84, 96-99]. Particle diameters ranging from tens of nm to several microns can be used to obtain polycrystalline monolayers with a size up to several cm^2 . Colloidal monolayers can be directly obtained on solid substrates by applying a

colloidal suspension under controlled evaporation conditions. Alternatively, they can firstly assemble on a liquid-liquid or liquid-gas interface and then be transferred onto solid substrates. Among others, the Langmuir-Blodgett (LB) technique is an efficient method for the fabrication of colloidal crystal monolayers: high quality monolayers are first formed within movable barriers on an intermediate surface (normally water), which allows for better particle mobility and ordering, and then transferred to the target substrate by vertical dipping [83, 100-102]. The first investigation, regarding the spreading of monodisperse colloidal suspensions at the air-water interface, and the consequential assembly onto monolayers, was done in the late 60's [103]. Since then, hydrophobic polystyrene particles spread at the air-water interface have been investigated [104], but typical latex particles are made of a hydrophobic polymer core and an amphiphilic shell of emulsifier and/or stabilizer molecules. The surface charge and the use of surfactants within the subphase influence the buoyancy and the behaviour of the particles [105]. As a drawback, surfactant and residual stabilizers can co-spread and negatively affect the reproducibility of the particle assembly. To overcome this issue, some studies were addressed to the spreading and subsequent compression of LB monolayers without any stabilizer at the air-water interface [106, 107], but by simply playing with the subphase conditions, such as pH and temperature [108-110]. In addition to polystyrene particles, also glass, silica [100, 107, 111], or other inorganic micro and nanoparticles [112-115] were also studied.

1.3 THESIS MOTIVATION, OBJECTIVES AND OUTLINE

1.3.1 MOTIVATION AND OBJECTIVES

This work has been carried out in the framework of a collaboration with the industrial partner Plasmore Srl, an Italian company spin-off of the Joint Research Centre and the University of Pavia. These two institutions made available their facilities (Nanobiotechnology Laboratory located in Ispra and Department of Physics located in Pavia, respectively) to develop part of this work.

The motivation of this thesis relates to the optimization of large area plasmonic surfaces for biosensing as a continuation for standardization of previous works carried out at the University of Pavia [116, 117].

The main objective has been the refinement of a hybrid bottom up/top down nanofabrication process based on a combination of colloidal lithography and plasma processes to obtain a plasmonic sensor chip exhibiting highly sensitive LSPRs.

The first goal to achieve has been the development of 2D colloidal crystals over large areas by means of the Langmuir-Blodgett technique. We planned to study suspension-related parameters (spreading solvent, suspension volume) to evaluate the buoyancy of polystyrene

particles of different diameters (400, 500 and 1000 nm) and their assembly into 2D crystalline monolayers. Different subphase related parameters (pH, temperature) have been additionally evaluated to better control the particle organization. We then considered making Langmuir-Blodgett with bare and fluoro-silane treated SiO₂ particles as potential sacrificial masks to nanostructure silicon and glass.

In parallel, we have aimed at investigating further nanofabrication processes leading to the production of sensitive and high area plasmonic surfaces. We considered thus the use of different substrate materials and processing techniques/parameters for the deposition of the plasmonic material of choice (Au), since a control over the nanostructure features is strictly related to the spectral response of the final surface.

The final objective was the proof of concept application of the plasmonic surfaces as biosensing platforms. The flexibility of the nanofabrication process was assessed to tailor the surface performances for specific applications, such as imaging SPR and SERS.

1.3.2 THESIS OUTLINE

Chapter 2 describes the experimental methods used within each step of the nanofabrication process. Moreover, the characterization techniques employed for the analysis of colloidal monolayers and plasmonic surfaces are presented. The basics of imaging SPR and SERS are also introduced.

In Chapter 3, the development of Langmuir-Blodgett colloidal monolayers is detailed in terms of preliminary optimization of the isotherm curve and subsequent control over particle assembly. Optical and electron microscopy, together with image processing, allow one to assess the overall quality of the film and the crystal organization. Reflectance measurements provide information about order, uniformity and density of the colloidal monolayers.

The integration of the 2D crystal monolayers into a multi-step nanofabrication protocol is discussed in Chapter 4. Each single process (polymeric layer deposition, etching, gold deposition and surface post treatments) is deeply evaluated by combining results from microscopy (optical, SEM, AFM) and reflectance measurements in order to understand the influence to the nanostructured surfaces and consequently to the sensitivity of the final samples to refractive index changes. Ellipsometry, XPS and contact angle techniques provide further details regarding the nanostructure properties.

Chapter 5 relates to the application of the developed plasmonic surfaces for biosensing in imaging SPR and SERS experiments. These surfaces are firstly optimized and characterized for each specific application and then successfully applied in preliminary diagnostic assays.

Finally, Chapter 6 presents an overview of the main achievements and the future perspectives related to this thesis.

CHAPTER 2

EXPERIMENTAL METHODS

This chapter describes the investigated fabrication process of a nanostructured surface with effective performances for biosensing applications. An overview of all the techniques involved is presented, as well as an introduction to the characterization methods useful for surface analysis. Finally, the two biosensing techniques evaluated in this thesis, Imaging Nanoplasmonics and Surface Enhanced Raman Spectroscopy, are also described.

2.1 NANOFABRICATION PROCESS

The fabrication process involves several steps and merges bottom-up and top-down approaches based on a combination of colloidal lithography and plasma processes (Figure 2.1).

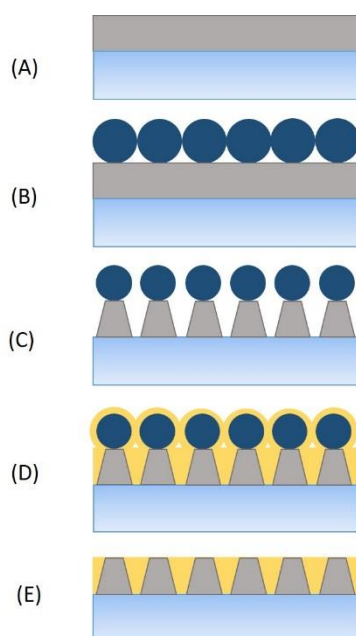


Figure 2. 1 – Sequential steps of the fabrication process. (A) polymeric layer deposition on glass or silicon substrate; (B) Langmuir-Blodgett assembly of 2D colloidal monolayer; (C) reactive ion etching; (D) gold deposition; (E) lift off of particle residuals.

Glass microscope coverslips (D263 T-eco, Schott) custom cut with dimension of (12 x 20 x 0.55) mm and standard one side polished (100) silicon wafers were used as substrates. Plasma

polymerized acrylic acid deposited by plasma enhanced chemical vapour deposition or polymethylmethacrylate deposited by spin coating were used as functional layers to coat the substrate with a defined and controlled thickness. Thus, 2D colloidal masks were transferred on top of the polymeric layer within a Langmuir-Blodgett trough. These crystalline masks were then exposed to a reactive ion etching (made of O_2 plasma or a combination of Ar/CF_4 plasma for polystyrene and silica colloids, respectively) by controlling the exposure time, in order to decrease the bead diameters and create a structure on the underlying polymeric layer. After this step, a layer of gold with controlled thickness was deposited by physical vapour deposition to fill the parts exposed after etching. Finally, to remove the residual of colloidal mask, the samples were immersed in isopropanol and placed in an ultrasonic bath for 5 minutes. The final structure is a hexagonal lattice of gold nanoholes made by polymeric pillars embedded in an optically thick gold layer, acting as plasmonic nanoantennas.

2.1.1 POLYMERIC LAYER DEPOSITION

Plasma enhanced chemical vapour deposition

Chemical vapour deposition (CVD) is a technique based on the formation of a thin solid film on a substrate by chemical reactions of vapour-phase precursors that occur both in the gas phase and on the substrate (Figure 2.2) [78, 118, 119].

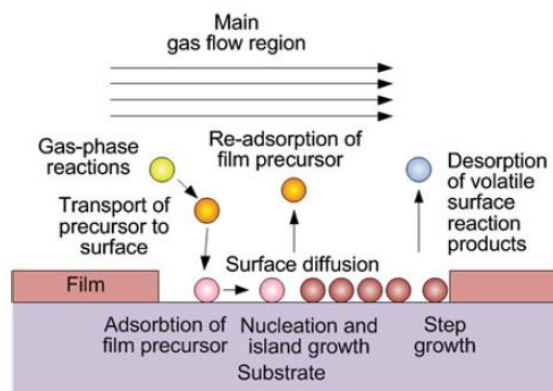


Figure 2. 2 – Schematic illustration of gas transport and reaction processes contributing to film growth by CVD [78].

In particular, in the case of plasma-enhanced CVD (PE-CVD) the gas-phase source is activated in a glow discharge environment: the electric energy, rather than thermal energy, is used to initiate homogeneous reactions for the production of chemically active ions and radicals that can participate in heterogeneous reactions, which lead to film formation on the substrate. The main advantages of PE-CVD are: broad range of control over plasma–chemical reactions and plasma–surface interactions to optimize the film composition and microstructure (tailorable packing density and environmentally stable films), with optional operation in bias-controlled mode;

tunability of deposition rates (up to high rates of ~1-10 nm/sec or more); possibility of depositing at low temperatures (normally ranging from near ambient temperature to 350°C) and atmospheric pressure glow discharge. This allows sensitive substrates to be coated; uniform coating of different substrate shapes; wide range of focus materials of inorganic, organic (such as “plasma polymers”) and nanocomposite or nanohybrid nature.

On the other hand, some drawbacks are: possible toxicity of precursor and by-products; higher equipment cost than alternative techniques for polymer deposition (e.g., spin coating); contamination from precursor and carrier gas molecules; possible substrate heating due to the plasma bombardment; maintenance required to control stoichiometry from batch to batch.

During a PE-CVD process there are external parameters (such as pressure, gas flow, discharge excitation and power) and internal parameters related to plasma characteristics (such as plasma density, electron energy distribution function, electrical potentials and fluxes of precursor species) to control. A typical equipment for PE-CVD consists of a reactor chamber, pumping system, power supply and monitor, electrical matching network, process control and diagnostics. Different configurations are available, ranging from low-, medium- and Radio-Frequency (RF) plasma reactor to microwave (MW) and Dual-Mode MW/RF systems, as to complementary deposition approaches (among others: plasma-assisted atomic layer deposition, hybrid PE-CVD and physical vapour deposition systems).

In this thesis, a functional layer of plasma polymerized polyacrylic acid (ppAA) was deposited on different substrate (glass, silicon wafers) by using acrylic acid (Sigma Aldrich) as monomer precursor in a PE-CVD equipment customized at the Nanobiotechnology Laboratory of the Joint Research Centre (JRC, Italy). The system is based on a capacitively coupled parallel-plate configuration, equipped with a Cesar RF power supply at 13.56 MHz (Advanced Energy). It was operated in bias-controlled mode, with a typical bias of 400 V and a pressure of 20 mTorr (which corresponds to approximately 2.66 Pa, according to conversion in SI units), leading to a deposition rate of ~25 nm/min.

Spin coating technique

The main purpose of the spin coating technique is to apply uniform polymer films like photoresist (e.g., polymethyl methacrylate PMMA) [78, 120]. During the operation of the instrument, the substrate (eventually pre-treated to enhance adhesion) is held by a vacuum chuck and few ml of a liquid precursor (typically a polymer) are dispensed in the middle of the substrate in static (with the substrate still at rest) or dynamic mode (supported by a slow spin). Afterwards, the spin speed of the substrate is increased to thousands of rounds per minute (rpm). The centrifugal force distributes the polymer over the substrate and forms the film. By means of this technique it is possible to deposit resist films on top of different planar substrates

(made of different dimensions and materials) with high control over thickness homogeneity and within short coating times (i.e., few minutes). Normally the original resist is dispersed in a proper solvent that easily evaporates after spin coating, reducing time consumption before handling and soft-bake, which are normally required after the coating process. As a drawback, the spin coating presents disadvantages in case of non-rotation-symmetric substrates, because the strong air turbulence at the substrate edges leads to the formation of pronounced edge beads. Moreover, in the case of textured substrates, the coverage can be incomplete.

PMMA is a versatile polymeric material, commonly used as positive resist for microelectronic application and normally formulated with 495000 and 950000 molecular weight (PMMA 495 and PMMA 950, respectively). The resist film thickness attained by spin coating represents the equilibrium between centrifugal force and solvent evaporation, both increasing with spin speed. The spin speed versus thickness curves provided within the material datasheet give useful information to select the appropriate PMMA dilution and spin conditions needed to obtain the desired film thickness. Figure 2.3 shows the calibration curves related to 950 PMMA resists commercialized by MicroChem at different solid concentration in anisole [120].

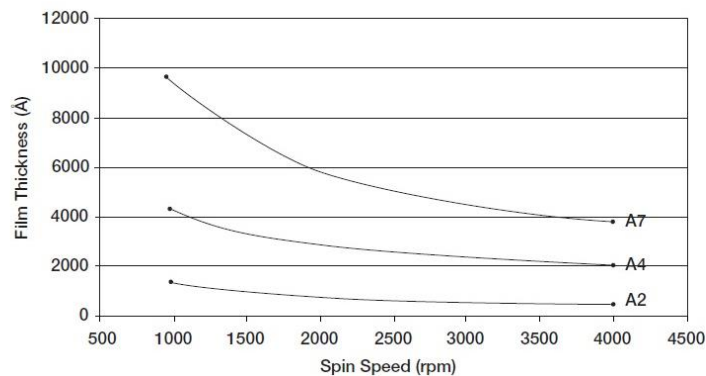


Figure 2. 3 – Calibration curves for 950 PMMA resists at different solid concentration in anisole (A2: 2%; A4: 4%, A7: 7%) [120].

In this thesis, we used a spin coater WS-400B-6NPP-LITE (Laurell Technologies Corporation). Since the purpose was to obtain a polymeric layer in the range of 150-200 nm, we selected a resin made of PMMA with 950000 molecular weight dispersed at 4% in anisole (950 PMMA A4, MicroChem), additionally diluted to 3.6% when a thickness around 150 nm was needed. Indeed, a higher molecular weight should ensure a better control over etching process.

The operating procedure is resumed below:

- substrate preparation: sequential cleaning in acetone, ethanol and water and final dry under N₂ flow. Just before the coating, an O₂ plasma cleaning was performed;

- coating: static dispensing of the resist over the substrate, static spread for 10 sec, ramp to final spin speed of 6000 rpm at high acceleration rate and hold for a total of 60 seconds;
- post-bake: solvent evaporation and layer stabilization on hot plate at 200°C for 20 min.

2.1.2 LANGMUIR BLODGETT TECHNIQUE

The Langmuir Blodgett (LB) trough is a computer controlled and user programmable instrument for automated Langmuir and Langmuir-Blodgett film experiments and deposition on solid substrates [121]. This technique represents a simple and rapid method to coat large scale and defect free areas, with high degree of control over the crystal organization and potential application to the wafer scale production. The device is a modular instrument made of different components as described below and reported in Figure 2.4 (model MiniTrough, KSV Instruments Ltd):

- a Langmuir trough made of PTFE (available in several sizes) with proper effective film area and equipped with a dipping well for the immersion of the samples;
- a sensor element for surface pressure control (i.e., Wilhelmy plate);
- two symmetrically moving barriers made of PTFE for surface area regulation;
- a dipping arm, for the transfer of the surface film on solid substrates;
- a manual control unit to move barriers and deposition arm outside of the software control;
- in addition, it can be equipped with an external thermostating bath to select subphase temperature during operation (not shown in the picture).

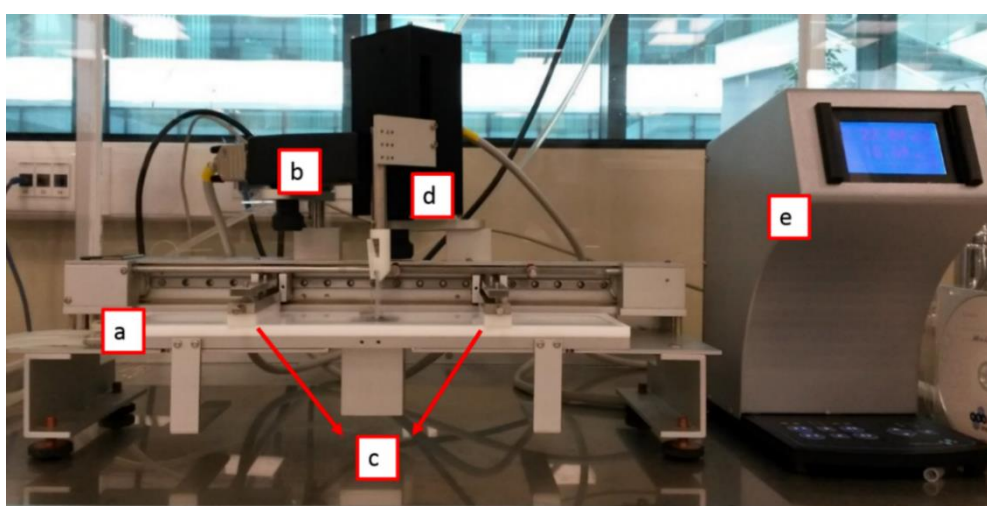


Figure 2. 4 –Overview of a LB instrument. a) trough; b) pressure control element; c) moving barriers; d) dipping arm; e) manual control unit.

The basic principle for the formation of a LB monolayer is the trapping of amphiphilic molecules/materials at the interface of two phases, either liquid-liquid or liquid-gas, and

depends on the particular thermodynamic properties of this interface [96]. The energy difference in the state of a molecule lying on the surface and the same molecule solved in the bulk of a liquid leads to an excess of free energy, also known as surface tension γ , defined by equation 2.1:

$$\gamma = \left(\frac{\delta G}{\delta A} \right)_{T,P,n} \quad (2.1)$$

where G is the Gibbs free energy of the system, A is the surface area, and the temperature T , the pressure P and the composition n are held constant. Due to the exceptionally high value of its surface tension (around 72.8 mN/m at 20 °C and atmospheric pressure), water is by far the most often used subphase in LB experiments. The tendency of colloidal particles (either organic, e.g. polystyrene, or inorganic, e.g. silica) to lower the surface tension by their presence allows them to remain at the air-water interface and make it possible to obtain controlled colloidal monolayers. The surface pressure (even if not strictly a pressure from its magnitude units), is normally measured by a Wilhelmy plate, and determined by equation 2.2:

$$\Pi = \gamma_0 - \gamma \quad (2.2)$$

where γ_0 is the surface tension of the pure liquid subphase and γ is the surface tension of the monolayer-covered subphase. After the spreading of the particles over the liquid subphase (normally done by means of a microsyringe), the system is kept at constant temperature and the barriers are programmed to move, in order to record an isotherm curve monitoring the variation of the surface pressure as a function of the area available for film formation. A typical isotherm curve (Π - A) for polymer particles, which records the surface pressure as a function of the surface area, is shown in Figure 2.5 [109].

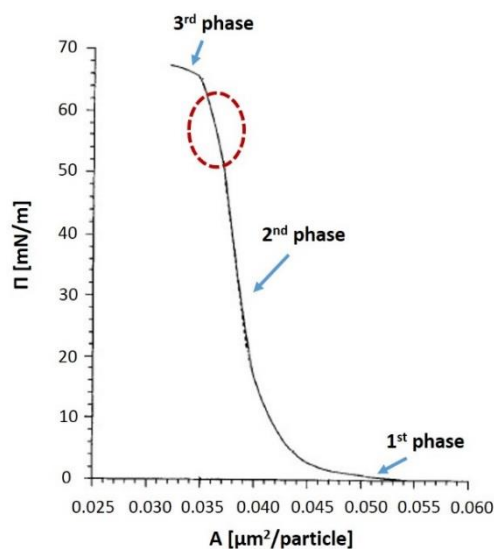


Figure 2. 5 – Typical isotherm curve of polymer particles. 1st phase: non interacting particles; 2nd phase: close packing monolayer formation; 3rd phase: collapse. The dashed red circle corresponds to the region with highest close packing of the particles, ideal to transfer the monolayer to a solid substrate. Adapted from [109].

It is possible to notice several regions (or phases) determined by the physical and chemical properties of the spreading molecules/particles, the subphase temperature and composition. The first phase corresponds to high area values and low surface pressure since the particles are not in close contact. As the compression undergoes, there is a first transition corresponding to the mutual interaction of the particles and the formation of a compact monolayer (second phase). Upon further compression, the monolayer reaches the collapse and it is seen as a transition into a decrease of surface pressure (third phase). The highest part of second phase (i.e., higher surface pressure before transition) corresponds to the closest packing of the monolayer and gives an indication of the optimal values of surface pressure for the transfer. Indeed, once reached a selected value of surface pressure, the dipping arm starts moving while the moving barriers simultaneously keep the surface pressure constant. A computer controlled feedback system exists between the barrier motors and the electrobalance measuring the surface pressure, allowing a homogeneous transfer of the floating monolayer to the solid substrate (Figure 2.6).

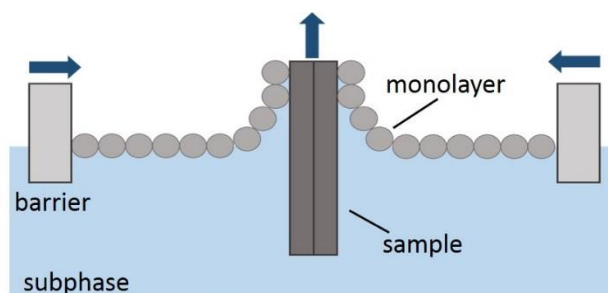


Figure 2. 6 – Schematic illustration of the colloidal monolayer assembly and transfer. The particles are spread at the air-water interface, the moving barriers favour their ordered assembly and the obtained monolayer can be transferred on solid samples. Adapted from [121].

The transition of a LB isotherm into different regimes strictly depends on the electrostatic forces acting between the colloidal particles, as described by the DLVO theory (developed by Derjaguin, Landau, Verwey and Overbeek) [122, 123]. Basically, in case of electrostatically stabilized and equally charged particles, the total interaction potential (V_T) between them is the sum of repulsive electrostatic forces (V_R) and attractive Van der Waals forces (V_A), as depicted in Figure 2.7. At short distance, the curve of the potential energy shows a primary minimum, since at these low molecular distances the Van der Waals attractive forces are dominant over the repulsive forces, even equally charged particles tend to cluster irreversibly when forced into physical contact. At intermediate distances, the electrostatic repulsive forces become bigger than the attractive ones, the particles remain dispersed and the interaction potential displays a primary maximum. When the separation distance further increases, the repulsive forces decrease faster than the attractive forces, resulting in the secondary minimum.

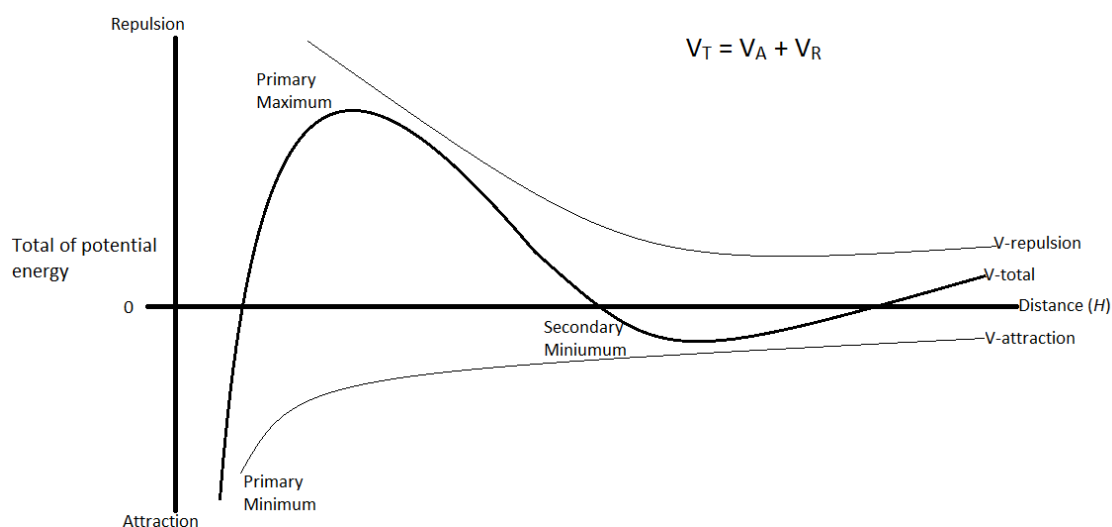


Figure 2.7 – Schematic of the DLVO theory for the potential energy [124].

In this thesis, we use the LB technique to study the formation of highly ordered colloidal monolayers formed at the air/water interface and then transferred on solid substrates. The MiniTrough and MicroMini models (KSV Instruments Ltd) of the LB instruments were used, available at the Nanobiotechnology Laboratory of the JRC and at the Department of Applied Physics of Universidad Autónoma de Madrid (UAM, Spain), respectively. They basically differ for the area of the trough (area with wide open barriers is 330 x 75 mm and 170 x 50 mm, respectively) and for the maximum size of substrate to be transferred (60 x 35 mm² and 30 x 25 mm², respectively). In all experiments just one deposition cycle was considered and the compression speed, as well as the dipping speed, was set to 4 mm/min. A deep study of the LB parameters will be presented in Chapter 3.

2.1.3 REACTIVE ION ETCHING

An etching process can be defined as a surface modification of a material through its own dissolution by applying liquid or gaseous chemically aggressive compounds (etchants) or through electrochemical effects [78]. Normally, a protective layer masks the areas not supposed to be attacked by the etchant and, once removed at the end of the etch process, it leads to patterned structures. The main etching techniques of solid surfaces can be ascribed as wet processes if the etchant is liquid (wet-chemical etching or electrochemical), or dry processes if the etchant is gaseous (physical, chemical, or a combination of both). In particular, in dry etching, the etchant may be a vapour (vapour phase etching) or a gas in a state of plasma, which can enhance the chemical attack (plasma etching) and/or create charged particles to physically bombard the substrate (ion beam etching). Moreover, the etching may be in all directions (isotropic etching), follow crystal directions of single crystal materials (anisotropic etching), or

have a preferential direction (directional etching). In addition, selective etching can be applied to etch alternative materials with different rates and it is particularly useful to etch a sacrificial layer to fabricate micro and nano structures.

Reactive ion etching (RIE) is a process performed in a vacuum chamber (typical process pressure between 0.01 and 0.2 Torr), which uses a glow discharge to achieve ion bombardment and chemical reactions to provide a directional etch (Figure 2.8).

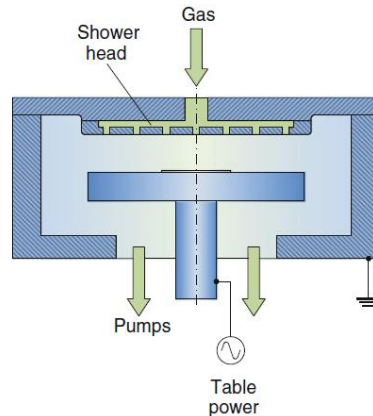


Figure 2. 8 – Schematic representation of a parallel plate RIE system [78].

A good control over ion density, electron temperature, and plasma potential is fundamental to ensure a uniform plasma etching. The type of gas used varies depending on the etch process but the most often selected are carbon tetrafluoride (CF_4) and oxygen (O_2) to etch inorganic and organic materials, respectively. A parallel plate reactor is the most common configuration and the plasma is commonly produced in the system by applying a strong RF (typically at 13.56 MHz) electromagnetic field to the bottom electrode. Since the top electrode is at ground potential, electrons deposited on it create a negative charge, which develops a negative voltage of a few hundred volts, creating a plasma with a slightly positive charge. Then, the positive ions tend to drift toward the bottom electrode due to the difference in voltage and collide with the samples to be etched. The ions react chemically or by transferring their kinetic energy with the material on the surface of the samples, stripping matter from it, which is then drifted away by the vacuum pump. As a result, the substrate is subject to a chemical attack by radicals (the isotropic chemical component of RIE), but also to ion impingement vertical on the substrate (the physical component of RIE, causing directional etching). Etching conditions in a RIE system are adjustable on many levels based on gas flow, pressure, and RF power settings (these latter determine both ion density and energy). Additionally, a faster etching can be achieved by raising the temperature of the chamber during the RIE process.

In this thesis, we used different types of RIE equipment. For the etching of organic materials (i.e., ppAA and PMMA), we used a combined inductively/capacitively coupled RIE customized at the Nanobiotechnology Laboratory of the JRC with O_2 (50 sccm) as etching gas and setting the

pressure at 10 mTorr (which corresponds to approximately 1.33 Pa, according to conversion in SI units) and the power at 140 W. Differently, for the etching of inorganic materials (i.e., silicon and glass), we used a Mini-Lab Plasma-Pod (JLS Designs) available at IMDEA Nanoscience Laboratory (Spain) with a mixture of Ar/CF₄ (5 sccm and 25 sccm, respectively) as etching gas and setting the pressure at 25 mTorr (which corresponds to approximately 3.33 Pa, according to conversion in SI units), while testing different powers (45 – 60 – 75 W).

2.1.4 GOLD DEPOSITION

PVD processes include different methods to deposit thin solid films (e.g., metals such as gold and ceramics such as oxides and nitrides) onto various surfaces and involve the physical ejection of material as atoms or molecules and the subsequent condensation and nucleation of these atoms onto a substrate [78, 125, 126]. Indeed, a PVD process can be defined by three basic steps:

1. Creation of vapour-phase species in order to convert the target material to a vapour phase (by evaporation, sputtering, or chemical vapours and gases when combined with CVD into hybrid processes);
2. Transport of vapour species from the source to the substrate, with (plasma-assisted ionization) or without collisions between atoms and molecules during transport;
3. Film growth on the substrate by nucleation of atoms or molecules deposited on the substrate.

Among other PVD technologies, sputtering and thermal evaporation are two of the most used methods (Figure 2.9). In the former case, a plasma process ejects atoms from a solid target due to a collision impact with excited ions and they travel from the source to substrate under vacuum conditions. In the latter case, the transformation is caused by a thermal process resulting in evaporating solid or liquid materials.

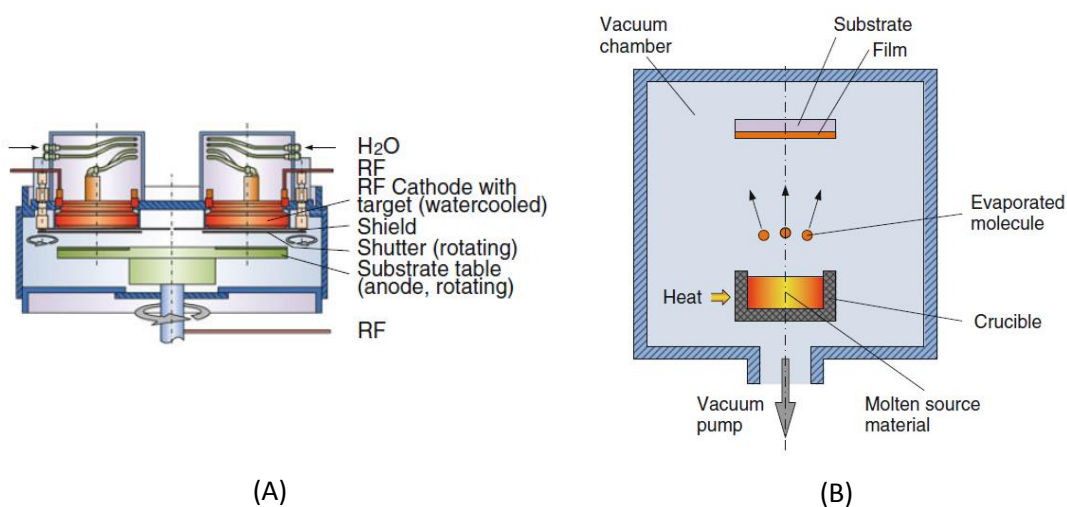


Figure 2. 9 – Schematic illustration of sputtering (A) and evaporation (B) PVD tools [78].

PVD magnetron sputtering

Sputter deposition is a vacuum process which involves the physical vaporization of atoms from a surface of a target material by momentum transfer from bombarding energetic atomic-sized particles (usually ions of a noble gas accelerated in an electric field) [125, 126]. Then, ejected atoms or molecules can be condensed on a substrate to form a surface coating.

Among others, direct current (DC) magnetron sputtering is one of the most typical configurations. A suitable magnetic field is applied together with an appropriate arrangement of the magnets, resulting in a high density plasma from which ions can be extracted to sputter the target material. Many sputtering target configurations are available: planar DC diode, planar magnetron, "S" gun, etc.

The main advantage of magnetron sputtering relates to the possibility to create a dense plasma near the cathode at low pressures. This results in ions accelerated from the plasma to bombard the cathode without loss of energy due to physical and charge exchange collisions and allowing high sputtering rates at low potential (several hundred volts) on the target. Moreover, in order to improve surface coverage and planarization, a negative bias may be applied to the substrate, instead of assuming a self-bias with respect to the plasma, giving a continuous bombardment during deposition. Additional advantages of the sputtering deposition are: broad range of target materials; high stability of the target; large-area vaporization source and possible specific vaporization geometries, depending on the configuration; good reproducibility of sputtering conditions from run to run; little radiant heating in the system (if compared to vacuum evaporation); possible reactive deposition by activating the plasma with reactive gasses (typically N₂ and O₂). Despite of these, some disadvantages are: need of fixturing and tooling in some configurations to overcome non-uniform deposition; need of target cooling; lower vaporization rates compared to thermal vaporization; expensive targets with low degree of utilization; high substrate heating in some configurations; film contamination in plasma-based processes due to contaminants on surfaces in the deposition chamber or gaseous contaminants activated in plasma.

In this thesis, we used a DC Magnetron Sputter Univex 350 (Oerlikon Leybold Vacuum GmbH) available at the Nanobiotechnology Laboratory of the JRC to deposit thin films of gold and a previous adhesion layer of titanium. Argon (100 sccm) was used as input gas, the generator was set to 45 W, a bias of 120 V was applied by an RF generator and the operating pressure was in the order of 10⁻³ mbar (which corresponds to 10⁻¹ Pa, according to conversion in SI units). The deposition rates of gold and titanium were 40 and 5 nm/min, respectively.

PVD evaporation

The most common thermal PVD process is called thermal evaporation [78, 125, 126] and relates to the transfer of a source solid or molten material into the gaseous phase. The evaporation occurs under high vacuum conditions and the boiling is caused by thermal or electron beam heating of a source material. The evaporated material travels in a straight line from the melting location before it collides with structures in the vacuum chamber or residual gas atoms. At the substrate surface, the material condenses, resulting in a thin film of the material originally evaporated. The main components of a typical evaporation equipment are: vacuum chamber, evaporation sources, a substrate holder and a quartz crystal microbalance as in-situ film thickness measurement system. The evaporation source can be of different type (e.g., resistively heated sources, sublimation sources) built within a non-reactive, non-melting crucible. Additionally, the system can be equipped with a shutter to better control the deposition. The vapour pressure is the dominant physical parameter for evaporation and the thickness uniformity of the coating is mainly influenced by the characteristics of the evaporation source (point or surface source), as well as by position and orientation of the substrate inside the vacuum chamber. In order to favour the chemical purity of the evaporated film, it is important to minimize any contamination from the source material, heaters and residual gases inside the chamber.

The main advantages of thermal evaporation are: possible use of masks to define areas of deposition due to the line-of-sight deposition; availability of large-area sources; possibility of high deposition rates; many forms of source material and possibility of high purity films. On the opposite, some disadvantages are: need of tooling and fixturing to improve surface coverage and uniformity over large surface areas; poor ability to deposit many alloys and compounds; high radiant heat loads during processing; poor utilization of vaporized material and few processing variables available for film property control.

In this thesis, we used a Nanosphere thermal evaporator (Oxford Vacuum Science) available at IMDEA Nanoscience Laboratory (Spain) to deposit thin films of gold and a previous adhesion layer of chromium. It was operated at a pressure of the order of 10^{-6} mbar (which corresponds to 10^{-4} Pa, according to conversion in SI units) and the deposition rate was circa 2 nm/min.

2.2 2D COLLOIDAL CRYSTAL CHARACTERIZATION

2.2.1 CRYSTAL DOMAINS AND SURFACE ANALYSIS

Optical microscopy

Optical microscopes (also called light microscopes) use visible light and a system of lenses to produce a magnified image of an object, which can be captured by the human eye or by normal

light-sensitive cameras to generate a micrograph [127]. They normally resolve objects separated by hundreds of nm. An improved resolution (down to 100 nm) can be obtained using light with a shorter wavelength (blue or ultraviolet) or immersing the specimen and the front of the objective lens in a medium with a high refractive index (such as oil). Two lenses, the objective lens (obj) and the ocular (oc), work together to produce the final magnification (M) of the image, according to:

$$M_{fin} = M_{obj} * M_{oc} \quad (2.3)$$

Indeed, the main components of a light microscope consist of the objective lens, which collects light diffracted by the specimen and forms a magnified real image at the image plane near the oculars, and the ocular lens (or eyepiece) that gives an enlarged inverted virtual image of the object (Figure 2.10).

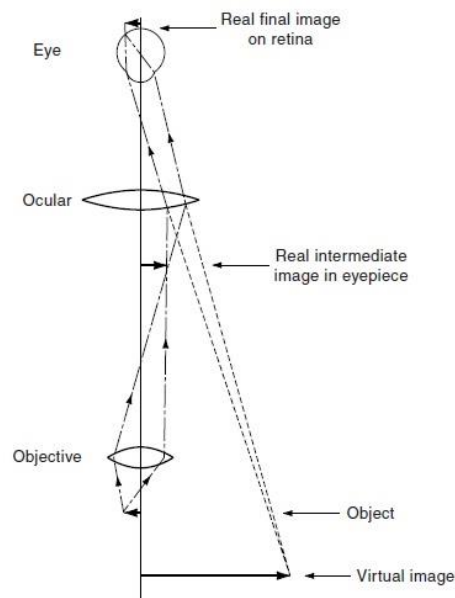


Figure 2. 10 – Schematic illustration of the image formation in an optical microscope [127].

Other components include condenser lens, objective turret or resolving nose piece, light source, filters, polarizers, retarders, and the microscope stage and stand with coarse and fine focus knobs.

The main parameters to describe an optical microscope are resumed below:

- numerical aperture (NA)

$$NA = n * \sin \alpha \quad (2.3)$$

where α is the half angle of the cone of specimen light accepted by the objective lens and n is the refractive index of the medium between the lens and the specimen. A wider NA relates to a better resolution and it can be achieved, for instance, by increasing the refractive index of the medium between the lens and coverslip with immersion in oil.

- resolving power (d)

$$d = 0.61\lambda/\text{objective NA}, \text{ in fluorescence and dark-field microscopy} \quad (2.4)$$

$$d = \frac{1.22\lambda}{\text{condenser NA} + \text{objective NA}}, \text{ in bright-field microscopy} \quad (2.5)$$

where d is the minimum resolved distance (in μm), λ the wavelength (in μm). It indicates a criterion for the resolution of two adjacent diffraction spots (called Airy disks) in the image plane.

- Depth of field (Z)

$$Z = n\lambda/\text{NA}^2 \quad (2.6)$$

where n is the refractive index of the medium between the lens and the object, λ is the wavelength of light in air, and NA is the numerical aperture of the objective lens. It refers to the thickness of the optical section along the z-axis within which objects in the specimen are in focus.

Optical microscopes can be available in upright and inverted designs. In the former design, the objectives are attached to a nosepiece turret on the microscope body, and the focus control moves the specimen stage up and down to bring the image to its proper location in the ocular. In the latter design, the stage itself is fixed to the microscope body, and the focus dials move the objective turret up and down to position the image in the eyepieces. In order to improve the specimen contrast or highlight certain structures in a sample, several illumination techniques are available, such as: bright field (contrast from absorbance of light in the sample), dark-field (contrast from light scattered by the sample), phase contrast (contrast from interference of different path lengths of light through the sample), fluorescence (contrast from light emission at lower frequency than the high energy light illuminating the sample), confocal (use of a scanning point of light and a pinhole to prevent out of focus light from reaching the detector). In this thesis, an upright light microscope DMRME Type 301-371 (Leica) equipped with a DFC280 camera (Leica) available at the Nanobiotechnology Laboratory of the JRC was used to inspect the surface of the samples and evaluate the efficiency of the different fabrication steps in terms of surface reproducibility and presence of defects or artefacts.

Atomic Force Microscopy

Scanning probe microscopy (SPM) is a technology focused on the formation of an image from the interaction of a proximal probe with a surface in a raster pattern while keeping track of the probe sample interaction as a function of probe position. It provides nanometer resolution information about many properties of a sample (e.g., topography, hardness, and conductivity). Among the different SPM techniques, in this thesis we have used atomic force microscopy (AFM) [126, 128, 129]. The AFM monitors the force between a sharp tip and a sample to produce images down to the atomic level, even in non-conductive samples. As a function of tip-sample

distance, different tip-sample interaction regimes can be distinguished: negligible force if the tip is far away from the surface; attractive (negative) force for closer tip-sample distance; repulsive force for very small tip-sample distance. The main components are: a sharp tip that is positioned on or above the sample surface; a cantilever that deflects as a result of the sample-induced forces placed on the tip; a piezoelectric actuator to precisely control the sensor above the surface and to raster the tip across the sample; a control system to provide feedback to the piezoelectric actuators and display the images; an isolation system to dampen ambient vibrations.

The working principle is based on the deflection of the cantilever by the interaction force (upward in the case of a net repulsive force, or downward in the case of a net attractive force), which acts as a spring according to Hooke's law:

$$F = kx \quad (2.7)$$

where F is the force exerted on the cantilever, k is the spring constant of the cantilever, and x is the distance of deflection. The deflection can be measured using a laser beam focused at the end of the cantilever and reflected from its back to a photodiode detector, while monitored by a control system (Figure 2.11).

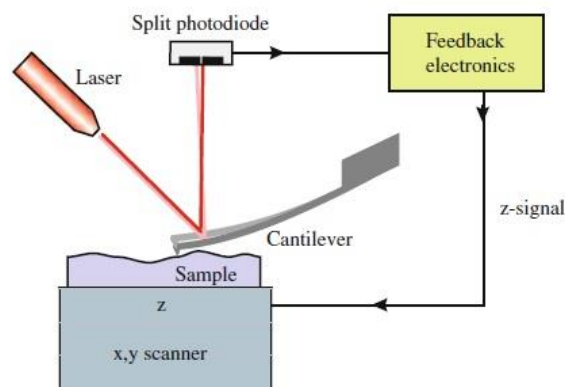


Figure 2. 11 – Schematic of the basic AFM instrumentation [128].

The AFM can operate in different imaging configurations, including contact, non-contact and tapping mode. In particular, within the tapping mode the cantilever is initially oscillated at its resonant frequency, then reduced as the tip comes in contact with the surface; this reduced amplitude is then used to maintain a fixed separation distance between the tip and the sample through adjustment of the piezo-actuators.

The AFM offers the advantage to operate under different controlled operating environments, such as ambient, aqueous and vacuum conditions, at elevated temperatures and pressures, and at cryogenic temperatures. As a drawback, tip artefacts are possible: if the features to image are much larger than the tip radius, then the resultant topography will be fairly accurate or if the tip radius is much larger than the features on the surface, the tip will impose its shape onto the

observed topography and broaden the features in the images. Moreover, soft samples can be damaged by the tip scanning and samples with excessive roughness should be avoided.

In this thesis, we used a Solver Atomic Force Microscope (NT-MTD) available at the Nanobiotechnology Laboratory of the JRC. It was equipped with a SMENA head and golden silicon cantilevers (force constant= 0.6 N/m) and it was operated in tapping mode to evaluate topography and profiles of the nanostructures obtained with the fabrication process.

Scanning Electron Microscopy

Scanning Electron Microscopy (SEM) can be used whenever information is required about the surface or near-surface region of a specimen [129-131]. Samples for conventional SEM generally have to be clean, dry, vacuum-compatible and, ideally, electrically conductive. A SEM uses a beam of electrons instead of light and uses electromagnetic or electrostatic lenses to focus the particles, allowing one to resolve features down to 1-10 nm. A SEM consists of an e^- source, an optical column (Figure 2.12), a vacuum chamber and an e^- detection system, all controlled currently through appropriate software.

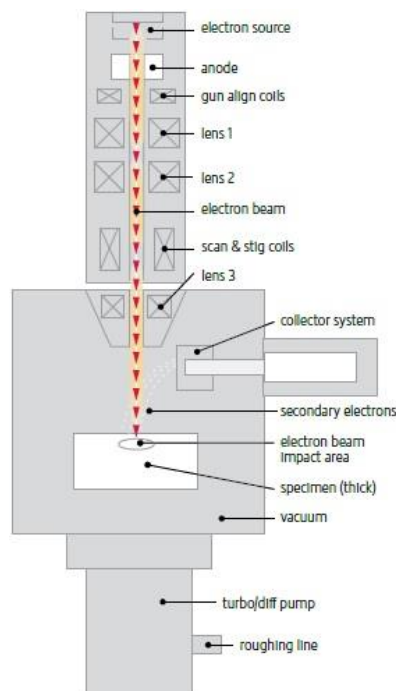


Figure 2. 12 – Schematic illustration of a SEM column [131].

The column is considerably short because the only lenses needed are those above the specimen used to focus the electrons into a fine spot on the specimen surface and there are no lenses below the specimen. The electron gun at the top of the column produces an e^- beam that is focused into a fine spot as small as 1 nm in diameter (accelerating voltage range: 50-30000 volts) on the specimen surface and is scanned line by line in a rectangular raster pattern over the specimen surface. The intensities of various signals created by interactions between the beam

electrons and the specimen are measured and stored in a computer memory. The stored values are then mapped as variations in brightness on the image display.

The specimen can emit secondary electrons (SE), reflected backscattered electrons (BSE) and X-rays. All these phenomena are interrelated and all of them depend to some extent on the topography, the atomic number and the chemical state of the specimen. The most commonly imaged signals in SEM are SE and BSE. SE, because of their very low energies, can escape the sample to be detected only if they originate very close to the sample surface. This gives SE images with high spatial resolution and strong topographic contrast (i.e., edges and flat horizontal planes appear brighter than walls and inclined planes which result darker). The BSE exit the sample surface after elastic scattering and their signal is used primarily for its strong atomic number contrast. Characteristic X-rays are also widely used in SEM for elemental microanalysis.

The quality of the image in a SEM depends on the orientation and distance of the specimen from the detectors and the final lens. The specimen stage allows the specimen to be moved in a horizontal plane (X and Y directions), up and down (Z direction), rotated, and tilted as required. In this thesis, two different SEMs were used to acquire images of colloidal monolayers and nanostructured samples from top and tilted view, as well as in cross section. The first instrument was a Nova 600i Dual Beam (FEI) available at the Nanobiotechnology Laboratory of the JRC, while the other one was a XL30 S-FEG (Philips) available at the Servicio Interdepartamental de Investigación of UAM (SIdI, Spain).

SEM image treatment

Since the image in a SEM is completely electronically produced, it can be subjected to analysis and manipulation using modern digital techniques to extract the best possible information from the specimen. In this thesis, the software ImageJ was used to treat images of colloidal monolayers and acquire information about the average dimension of crystal domains (A_{mean}) and percentage of crystalline area ($A_{cr}\%$). For the calculation of A_{mean} , the border of the domains was manually defined and then all the related areas (A_i : area of a domain i) were averaged to find an estimated mean value.

$$A_{mean} = \frac{\sum_{i=1}^n A_i}{n} \quad (2.8)$$

On the other hand, the $A_{cr}\%$ was calculated as a ratio between the sum of all the domain areas and the total area (A_{tot}) of the surface.

$$A_{cr}\% = \frac{\sum_{i=1}^n A_i}{A_{tot}} \quad (2.9)$$

An example of A_i and A_{tot} for a colloidal monolayer is depicted in Figure 2.13. Colloidal crystals at the edge of each frame were considered to contribute as $\frac{1}{2}$ in these analyses (statistically structures at the edge of the field shall contribute with half of their total area).

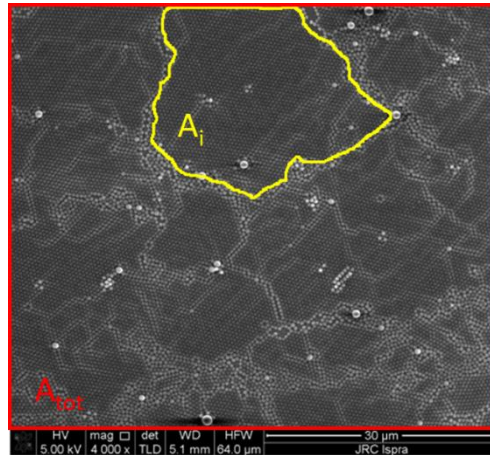


Figure 2. 13 – Example of a SEM image processing. A_i : area of a crystal domain i ; A_{tot} : total surface area.

X-ray Photoelectron Spectroscopy

X-ray photoelectron spectroscopy (XPS) involves the detection of photoelectrons emitted from a sample as a result of irradiation by X-rays and is a powerful technique for the analysis of the composition and chemical state of surfaces [126, 129, 132]. Indeed, it provides quantitative information of surface composition and can detect all elements (except hydrogen and helium) through the detection of the binding energies of the photoelectrons. Small variations in binding energies of the photoelectron lines as well as Auger lines, satellite peaks, and multiple splitting can be used to identify chemical states. It can provide depth information (up to 10 nm with standard X-ray sources) and the sample damage is normally absent or very limited.

The working principle is based on the irradiation of a sample with soft X-rays (typically in the range of 200-2000 eV), which leads to electrons emitted from surface atoms without inelastic energy loss to appear as spectral lines or photoelectron peaks as a function of binding energy. The presence of peaks at particular energies therefore indicates the presence of a specific element in the sample under study and the intensity of the peaks is related to the concentration of the element within the sampled region. Electrons that have lost energy appear as spectral background. The energy of the photoelectrons emitted from the sample is characteristic of each element and the binding energy (BE) of the ejected electrons is determined from the measured kinetic energy (KE), as sketched in Figure 2.14.

$$BE = h\nu - KE - \phi_s \quad (2.10)$$

where BE is binding energy of core level electron, $h\nu$ the characteristic energy of X-ray photon, KE the kinetic energy of ejected photoelectron, and ϕ_s the spectrometer work function.

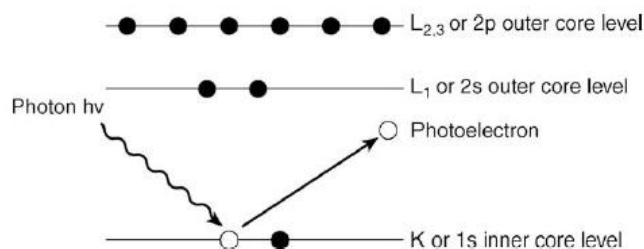


Figure 2. 14 - Schematic diagram of a photoemission process exploited in XPS [126].

Despite of the useful information provided by XPS, some limitations are: requirement of ultrahigh vacuum due to the low energy of the photoelectrons which easily get absorbed in air/poor vacuum, detection limits typically $\sim 0.01\text{--}0.1$ at.%, smallest analytical area $\sim 1\text{--}10$ μm , limited specific organic information, preferential sputtering can be a challenge during in depth quantitative analysis.

In this thesis, XPS measurements were carried out at the Institute of Catalysis and Petrochemistry (ICP-CSIC, Spain) by means of a Phoibos 150 9 mCD (SPECS GmbH) in order to evaluate the variations of composition and chemical states of colloidal beads treated with different surface functionalization, allowing one to estimate the efficiency of the treatment. Additionally, XPS analyses were also performed at the Nanobiotechnology Laboratory of the JCR (Italy) by using an AXIS Ultra device (Kratos Analytical Ltd) to investigate the effect of different gold treatment on nanostructured surfaces at the end of the fabrication process.

Contact angle

The measurement of the contact angle (CA) provides information about the degree of wetting when a solid and a liquid interact [133]. The most common system for CA measurements involves measuring a sessile liquid drop on flat solid surfaces; in this case, the CA is defined as the angle formed by the intersection of the liquid-solid interface and the liquid-vapour interface (Figure 2.15) and the interface where solid, liquid, and vapour co-exist is referred to as the “three phase contact line”.

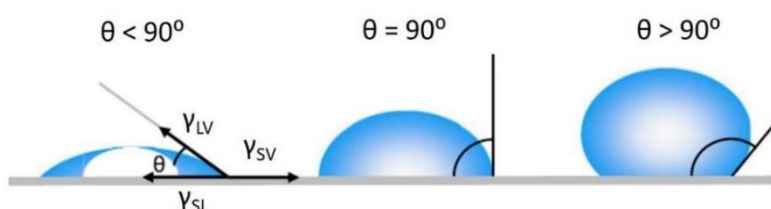


Figure 2. 15 – Schematic overview of contact angles formed by sessile liquid drops on a flat solid surface [133].

In particular, small contact angles ($< 90^\circ$) correspond to high wettability and the liquid spreads on the surface, while large contact angles ($> 90^\circ$) correspond to low wettability and the liquid

forms a more compact droplet. In the case of water, whenever there is almost no contact between the liquid drop and the surface, the term “super hydrophobic surface” applies ($CA > 150^\circ$). Additionally, contact angles can also be applicable to the liquid-liquid interface on a solid. The shape of a liquid droplet is strictly related to the surface tension of the liquid. Since the molecules exposed at the surface do not have neighbouring molecules in all directions to provide a balanced net force, an internal pressure is created and the liquid minimizes its surface area to maintain the lowest surface free energy. Generally, the CA of a liquid drop on an ideal solid surface is defined by the Young’s equation:

$$\gamma_{LV} \cos \theta_C = \gamma_{SV} - \gamma_{SL} \quad (2.11)$$

where γ_{LV} , γ_{SV} , and γ_{SL} represent the liquid-vapour, solid-vapour, and solid-liquid interfacial tensions, respectively, and θ_C is the contact angle.

The most widely used technique of contact angle measurement is a direct measurement of the tangent angle at the three-phase contact point on a sessile drop profile by means of a goniometer. The equipment consists of a horizontal stage to mount a solid or liquid sample, a syringe to form a liquid drop (eventually motor-driven to study advancing and receding CA), an illumination source and an integrated camera to take photographs of the drop profile. A proprietary software allows one to align the tangent on both sides of the sessile drop profile at the contact point with the surface and provides an averaged CA value. The method is simple and particularly convenient if high accuracy is not required. Indeed, it requires small amounts of liquid and small surface substrates, but as drawbacks there is risk of impurity contaminations and accuracy and reproducibility rely on the consistency in the assignment of the tangent line. Moreover, small contact angles ($< 20^\circ$) can be difficult to measure in terms of tangent line assignment. Finally, surface heterogeneity or roughness cause variations of the contact point along the three-phase contact line.

In this thesis, the CA were measured by means of a Digidrop MSE goniometer device (GBX) available at the Nanobiotechnology Laboratory of the JRC and by means of a goniometer KSW 100 (KSV Instruments Ltd) available at the Department of Applied Physics of UAM (Spain). Water was normally used as liquid phase and once the image of the droplet was acquired, the CA was automatically determined by setting the proper baseline and border fitting in the software menu. The values reported in this thesis for the different categories of samples are an average of the measurements of three samples processed under the same conditions.

2.2.2 OPTICAL ANALYSIS

Ellipsometry

Ellipsometry is a technique that measures the change in polarization state of the light reflected from (or transmitted through) the surface of a sample without need of reference samples [126, 129, 134]. Basically, ellipsometry measures Psi (ψ) and Delta (Δ), which are values related to the ratio of Fresnel coefficients \tilde{R}_p and \tilde{R}_s for p- and s-polarized light, respectively:

$$\rho = \frac{\tilde{R}_p}{\tilde{R}_s} = \tan(\psi)e^{i\Delta} \quad (2.12)$$

Ellipsometry is commonly used to characterize both thin films and bulk materials and can determine optical constants, layer thickness and several physical quantities which affect the optical constants (among others, roughness, crystallinity, optical anisotropy).

Variable angle spectroscopic ellipsometry (VASE) offers several advantages over fixed angle of incidence ellipsometers because it allows the user to acquire larger amounts of data even from complex samples and to optimize spectral acquisition ranges and angles of incidence for the determination of specific sample parameters. Moreover, spectroscopic measurements provide more information about the sample if compared to single wavelength measurements and give the possibility to acquire data in the most sensitive spectral regions. In particular, in the case of thin film characterization, ellipsometry works best when the film thickness is in the order of magnitude of the wavelength of the light used for the measurement and when the surface is smooth.

The general procedure for ellipsometry experiments does not directly measure the parameters of interest (e.g., complex refractive index, thickness) but rather Psi (ψ) and Delta (Δ), which are function of those parameters. It is then necessary to solve the inverse problem of modelling the measured data to infer the values of the sample parameters that ensure the best match between modelled and experimental data. Indeed, the basic procedure depicted in Figure 2.16 can be resumed in few steps:

- measurement of the sample, in terms of polarization states (optical quantities ψ and Δ) as a function of the wavelength, angle of incidence and/or sample rotation (if anisotropic);
- development of a model, from which it is possible to predict data measured from a sample of known properties. It includes some known parameters, and other unknown parameters to be fitted;
- fit model to measured data, based on the use of a regression algorithm to vary the unknown parameters of the model and generate data until a set of optimized parameters yields calculated data in close match with measured data;

- evaluation of the best-fit model, in order to establish if the best-fit set of parameters is unique, physically reasonable and not strongly correlated. If not, the model can be modified and the evaluation repeated.

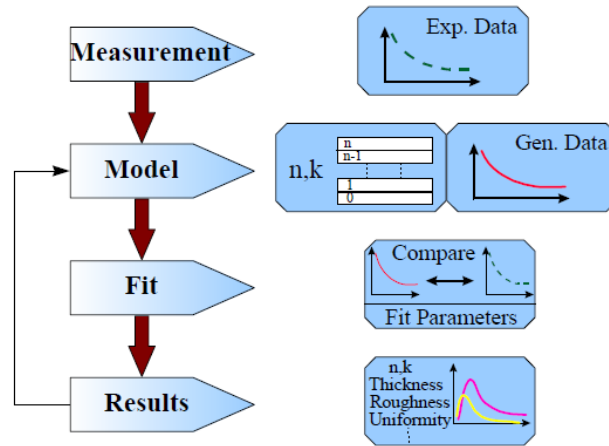


Figure 2. 16 – Basic procedure for optical experiments used in ellipsometry to determine material properties from experimental data [134].

In this thesis, a VASE ellipsometer model VB-400 (Wollam) available at the Nanobiotechnology Laboratory of the JRC was used to infer optical constants and thickness of thin polymeric films. The maximum wavelength range was between 300 and 1000 nm, while the incidence angles were 55°, 65° and 75°. The model for the fit of the experimental data was based on the default Cauchy layer, for which index of refraction n and extinction coefficient k can be represented by the following equations:

$$n(\lambda) = A + \frac{B}{\lambda^2} + \frac{C}{\lambda^4} \quad (2.13)$$

$$k(\lambda) = \alpha e^{\beta(1.24\mu\text{m}(\frac{1}{\lambda} - \frac{1}{\gamma}))} \quad (2.14)$$

where A, B, C are parameters of the dispersion model, λ the wavelength (in μm), α the extinction coefficient, β the exponent factor and γ the band edge (in μm). In particular, A, B, C were defined as parameters to fit. The thickness was initially set to an estimated value, then adjusted to a more realistic value by the regression analysis defined by the proprietary software.

Fourier Transform spectroscopy

Fourier Transform (FT) spectroscopy is a technique for measuring the spectrum of a sample, which takes advantage of the computation of the Fourier transform of physical data [135] and it is commonly based on the Michelson interferometer configuration (Figure 2.17). A beam-splitter is used for dividing the light emitted from the source into two beams. Then, they reach two distinct mirrors (one is fixed, while the other is movable) and, once reflected, the two beams are recombined by the same beam-splitter and sent to a detector where their interference is registered. If the fixed and the movable mirrors are equidistant from the beam splitter, there is

no optical path difference between the two beams. On the other hand, if the movable mirror is tuned to move at a distance d , an optical path difference (also called retardation) is introduced since one of the light beams has to travel an additional distance $\delta = 2d$ (back and forth) before the recombination occurs at the beam splitter.

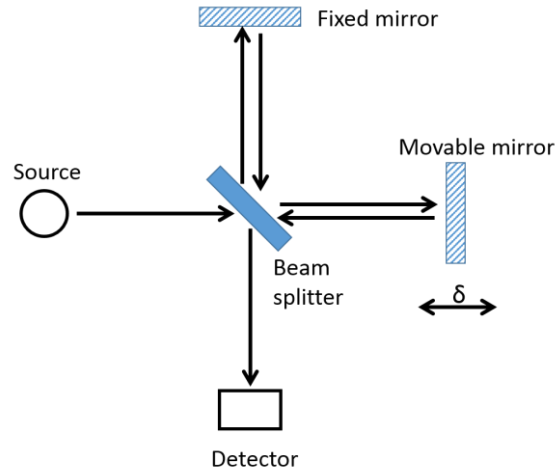


Figure 2. 17 – Schematic illustration of a Michelson interferometer. Adapted from [135].

In case of monochromatic light source, if $\delta=0$ or if $\delta=n\lambda$ (with λ wavelength and n integer) then the two beams are in phase and constructive interference occurs. On the opposite, if $\delta=\lambda/2$ or if $\delta= (n+1)\lambda/2$, then the two beams are out of phase and destructive interference is produced. Intermediate retardations δ result in a smooth behaviour. As the movable mirror moves, the interferogram can be described as the intensity output $I(\delta)$ recorded on the detector by:

$$I(\delta) = \frac{I_0}{2} \left[1 + \cos\left(\frac{2\pi}{\lambda} \delta\right) \right] \quad (2.15)$$

where I_0 is the intensity of the input source.

In case of polychromatic light source, the input signal can be viewed as consisting of infinitely many monochromatic sources, that are simultaneously interfering constructively only at $\delta = 0$ to produce a maximum signal. The recorded interferogram can be calculated by:

$$I(\delta) = \int_{-\infty}^{+\infty} S(\nu) \cos(2\pi\nu\delta) d\nu \quad (2.16)$$

where $S(\nu)$ is the spectrum of the light source expressed in wavenumbers (i.e., $\nu= 1/\lambda$).

Then, the inverse of the Fourier transform allows one to calculate the spectrum of the light source from the interferogram through:

$$S(\nu) = \int_{-\infty}^{+\infty} I(\delta) \cos(2\pi\nu\delta) d\delta \quad (2.17)$$

When a sample is inserted between the beam splitter and the detector, the output beam interacts with the sample and the recorded signal represents the convolution of the optical response of the sample and the source. The optical response of the sample is obtained by the ratio between this signal and a proper reference spectrum.

In this thesis, the optical characterization of the samples was carried out at the Department of Applied Physics of the University of Pavia (Italy) by angle resolved reflectance measurements using a commercial Fourier transform spectrometer (FT-66, Bruker) equipped with a homemade variable angle micro-reflectometer. A halogen lamp and a silicon detector were used to collect spectra in a range of 400-1250 nm, with a light spot of the order of 300 μm . A home-made flow cell was used in case of measurement in aqueous solution. Moreover, additional reflectance measurements were carried out at the Nanobiotechnology Laboratory of the JRC. These measurements were performed with an inverted microscope (Axiovert 25, Zeiss) coupled with a compact USB fiber optic spectrometer (USB4000, OceanOptics). A halogen lamp was used as the light source, and the spectra were acquired over the range from 400 to 1000 nm. Light was directed to the surface (from the glass substrate side) through a 5x objective with a NA = 0.13 (Epiplan 5x, Zeiss), and the back-reflected light was collected by the same objective lens.

2.3 BIOSENSING TECHNIQUES

2.3.1 IMAGING NANOPLASMONICS

The Imaging Nanoplasmonics device (iNPx™) is an imaging surface plasmon resonance (iSPR) microscope developed by Plasmore Srl (Figure 2.18 A) [136]. The detection technology is based on the use of disposable chips made of giga-arrays per cm^2 of plasmonic nano-antennas (Figure 2.18 B), whose nanostructure development is the main topic of this thesis.

(A)



(B)

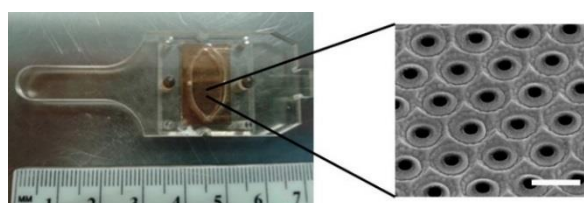


Figure 2. 18 – (A) Picture of the Imaging Nanoplasmonics device developed by Plasmore Srl [136]. (B) Disposable chip and inset of the surface made of giga-arrays per cm^2 of plasmonic nano-antennas. Scale bar: 500 nm.

The iNPx™ consists of a stand-alone, portable, multiplexing, label-free imaging system with integrated optics, fluidics, electronics, computing and data analysis, allowing both kinetic studies and spatially resolved information. The fluidic box consists of a dual-automatic syringe system, for continuous buffer dispensing at a flow regulated between 5 and 500 $\mu\text{l}/\text{min}$, connected to a disposable microfluidic cell sealed to the nanoplasmonic chip. The injection of the liquid sample is done by loading a fixed volume loop connected to a 6-port injection automatic valve. The volume of the cell is 10 μl , while the dead volume between the loop and the liquid cell is $<1 \mu\text{l}$. Images of the sample surface are acquired and analysed in real time using an in-house program that enables contemporary acquisition of up to 10000 sensorgrams of the corresponding regions of interest (ROIs). The fast acquisition time of the camera (maximum acquisition rate: 35 frames per second) enables one to average a large number of frames ensuring, at the same time, a good signal-to-noise ratio while maintaining the necessary time resolution to monitor molecular association and dissociation events on the surface with a sample-to-result time $< 20 \text{ min}$. The optimal compromise between time resolution and signal-to-noise ratio can be controlled by the instrument software. The imaging capability of the system also enables one to make the optimal self-referencing of the signal in the ROIs in order to compensate and correct temperature, flow, illumination, or electronic drifts. With a $\frac{1}{2}$ -in., 2048×1280 pixel CMOS camera, the lateral resolution achievable with the iNPx™ system is around 5 μm with a typical field of view of $13 \times 8 \text{ mm}$, that paves the possibility to reach a theoretical multiplexing capability higher than 1 million individual spots. The working principle of the iNPx™ is based on the continuous acquisition of the camera frames made by proprietary software and the related elaboration of averaged images [137]. The averaged image is then processed by the software in order to evaluate the reflectance variations occurring on the chip surface. A refractive index increase occurring within the first tenth of nanometers close to the surface top, normally results in a red shift of the main reflectance minimum. These changes on the surface of the chip are monitored by the CMOS camera. If the surface is illuminated by a light-emitting diode (LED) characterized by a slightly smaller (larger) wavelength than the resonance, the CMOS camera will detect an increase (decrease) of the intensity of the reflected light. The increase or decrease of the intensity of the reflected light is proportional to the relative variation of the refractive index at the surface. The image of the refractive index variations on the chip surface is transferred to the camera as reflectance variations by an optical imaging coupling system and it is possible to reach a refractive index sensitivity below 4 RU (1 RU= 10^{-6} RIU, where RU: response unit, RIU: refractive index unit). In particular, the reflectance variations are monitored in real-time in the following way:

- one or multiple ROIs are selected via software by the user and they correspond to a group of one or more pixels of the camera sensor;
- each ROI is characterized by a statistical distribution of pixels according to their grey level. The grey level corresponds to the intensity of the reflected light to the camera sensor on each pixel;
- for each ROI, the median value of the distribution of grey levels is calculated from the distribution histograms;
- the real-time evolution of the median value is then calculated by the software and plotted in a sensorgram;
- the sensorgrams are then subtracted to the reference value (e.g., the first value of the baseline) in order to calculate the relative percentage variation of reflectance for each ROI.

2.3.2 SURFACE ENHANCED RAMAN SPECTROSCOPY

Raman spectroscopy is the study of inelastic scattering of monochromatic light (usually from a laser in the visible, near-IR, or near-UV range) and, when applied to molecules, it provides an insight into their vibrational and chemical structure [125, 138]. The working principle is based on the interaction of light with phonons or other excitations in the system, resulting in a Raman spectrum that plots the intensity of light as a function of frequency above and below the frequency of the incident light. Rayleigh and Raman scattering can be observed, which relate to frequencies of the incident photon and to energy changes owing to the inelastic scattering, respectively. In particular, this inelastic Raman scattering depends on the molecular/electronic structure of the molecules and the quantum mechanical selection rules for Raman scattering. The separation of Raman lines and the Rayleigh line in the spectrum is a direct indication of the vibrational frequencies of molecules or atoms in a crystal lattice. While the Raman scattering implying the creation of a phonon and having a lower frequency than the Rayleigh line is known as 'Stokes scattering', the reverse process which arises from decay of a previously existing excited vibrational state in the sample is known as 'anti-Stokes scattering'. When the light used for excitation is focused on a small area, it is possible to conduct Raman spectroscopy in a microscope mode with resolution at the micrometer level (Figure 2.19). Surface Enhanced Raman Scattering or Spectroscopy (SERS) consists in using localized surface plasmon resonances due to (mostly) metallic nanostructures to produce an enhancement of the Raman signal of molecules at (or close to) the surface of the structures. Indeed, in this technique, the amplification of the signals from molecules very close to the metal surface comes through the

electromagnetic interaction of light with metals, which produces large amplifications of the laser field through excitations of plasmon resonances.

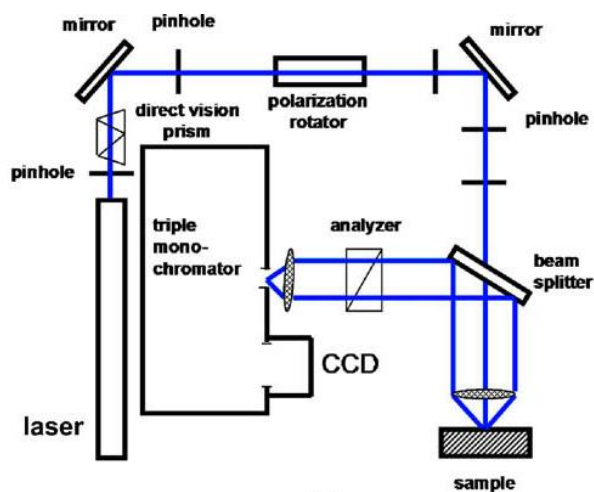


Figure 2. 19 – Schematic of a Raman microscope [125].

Metals in SERS include a variety of different substrates, from metallic particles in suspension to nanostructured metallic substrates. Colloid suspensions are expected to provide a more homogeneous signal, while solid surfaces are easy to functionalize and suitable for multiplexing applications [139]. SERS enhancements of a given substrate are normally limited to a specific excitation wavelength range and the majority of substrates are designed to operate with visible/near-IR excitation (~400-1000 nm), which is the typical range of interest for molecular Raman scattering experiments. Gold or silver, as well as objects with dimensions in the sub-wavelength range are the most suitable substrates to sustain plasmon resonances in that range. Some substrates can provide a relatively uniform enhancement with good performances in terms of reproducibility, while some others can act as ‘hot-spots’ and exhibit some extraordinary enhancement of the Raman signal between closely situated nanosized elements, particularly suited for single-molecule detection. In addition, another important parameter to consider is the surface area of the substrate, because a larger area increases the potential number of molecules that can produce SERS. A good detection requires also the use of proper SERS probes. These molecules have to show intrinsic Raman properties, such as dyes with electronic energies close to the exciting laser energy and, consequently, intense Raman scattering. Moreover, a good Raman probe should be able to adsorb efficiently on the SERS substrate, which can be implemented by proper surface functionalization methods (e.g., thiolization in case of gold surfaces).

In this thesis, Raman spectra were acquired using an Aramis Raman microscope (Horiba) available at the Laboratory of Nanomedicine and Clinical Biophotonics (Labion, Fondazione Don Carlo Gnocchi ONLUS, Italy). The microscope is equipped with three laser lines with different

Chapter 2

wavelengths of 532, 633, and 785 nm. With this Raman instrument, it was possible to obtain a single spectrum from a specific point of the chip (about 1.5 μm diameter) or to collect all spectra acquired from a selected area on the surface (mapping) and analyse them by means of the LabSpec 6 software of Horiba. The DuoScan function of the Raman microscope was used to acquire spectra in mapping mode: the laser beam was moved across the surface by a combination of scanning mirrors and it allowed collecting light from a larger area (50 μm x 50 μm) and decreasing the signal intensity deviations caused by surface inhomogeneity.

CHAPTER 3

COLLOIDAL MONOLAYER DEVELOPMENT

This chapter describes a systematic study regarding the formation of crystalline monolayers of colloidal particles by means of the Langmuir-Blodgett (LB) technique. Indeed, the first goal to succeed in the formation of a 2D crystal is to promote the buoyancy of the particles and their hexagonal close packed arrangement.

In this investigation, we used commercially available negatively charged latex beads made of a hydrophobic core of polystyrene (PS) with aldehyde/sulfate functional groups on the surface (Invitrogen, Molecular Probes). Particles with different diameters (400 nm, 500 nm, 1 μm) were evaluated. In addition, we also tested inorganic particles made of SiO_2 with a nominal diameter of 1000 nm (Angstrom Sphere™, Fiber Optic Center Inc.). In all experiments, a fixed volume of those monodisperse particles was centrifuged to remove the supernatant (water, surfactant and salt present in the original suspension). The recovered pellet of particles was redispersed in a mixture of spreading solvent and ultrapure water (Milli-Q). After an ultrasonic bath, the particle solution was dispensed with a microsyringe onto the surface of an aqueous subphase within a LB trough (Mini-trough and MiniMicro-trough, KSV Instruments Ltd). Ultrapure water was chosen as a LB subphase because of its high value of surface tension (72.75 mN/m at 20°C), which allows obtaining buoyant particles without addition of surfactants. After waiting for the system stabilization for few minutes, the trough was compressed at a constant rate and any variations in area and surface pressure (SP or Π) were recorded. The pH value of the subphase was adjusted by adding hydrochloric acid. The temperature of the trough was set and controlled by means of a bath circulator.

The monolayer formation at the surface trough was studied by measuring SP vs. area (Π -Area) isotherms and allowed the identification of optimal parameters to obtain and transfer 2D colloidal crystals. In addition, monolayers on solid substrates were prepared upon LB deposition and the particle organization was characterized by optical microscopy and SEM and near to normal reflectance measurements, normalized with respect to a gold reference. Besides, an image processing was performed on some samples by using the software ImageJ, in order to

achieve information about the average crystal dimension and the percentage of the crystalline area.

3.1 ISOTHERM CURVE OPTIMIZATION

The optimization of compression isotherms was successfully applied to PS particles with different diameters. A typical isotherm curve, obtained in our experiment for PS 500 nm particles (4% w/v), is shown in Figure 3.1.

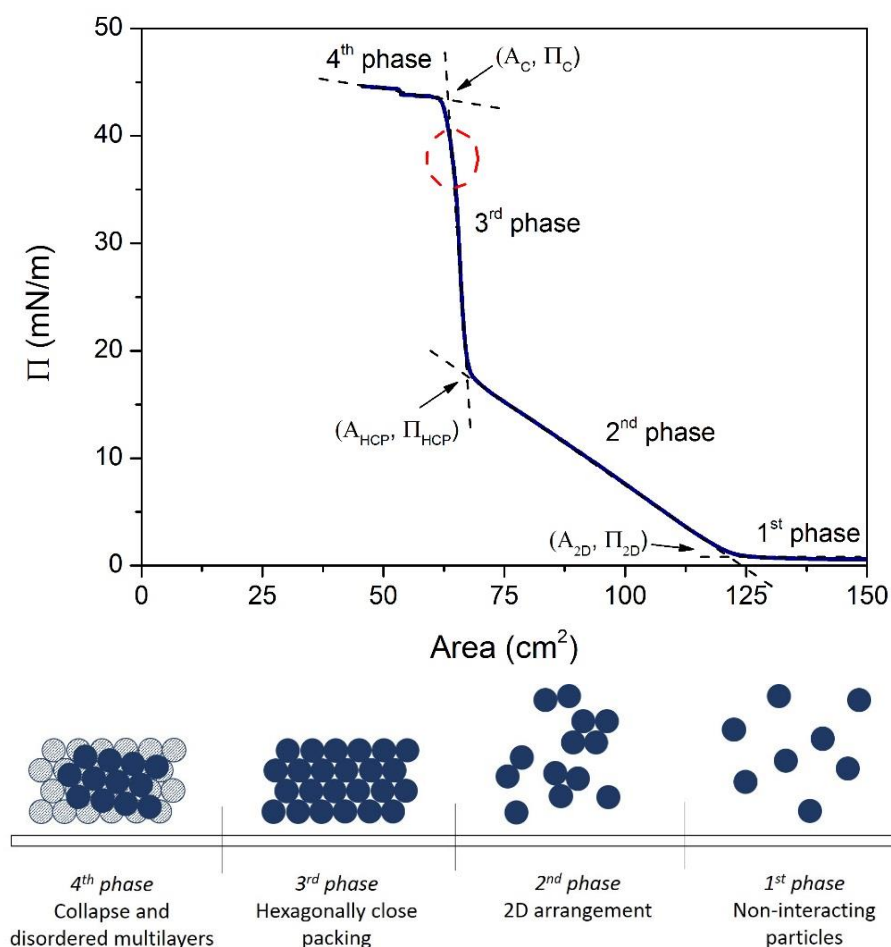


Figure 3. 1 - Experimental LB isotherm (top) and scheme of the monolayer formation (bottom). The dashed red circle indicates the region ideal for the monolayer transfer.

It mainly differs from ideal curve presented in Chapter 2 for the presence of an intermediate 2nd phase. At high area values, the isotherm shows an initial constant value for the SP. In this regime (1st phase), the particles adsorbed at the air-water interface are not in close contact and the SP is close to zero. As the compression of the barrier progresses (2nd phase), the particles are forced into closer physical contact and they start to arrange themselves in a 2D structure (A_{2D} , Π_{2D}) forming a continuous network of particle islands. When the separation distance critically decreases, the SP rises very rapidly with small compressions (3rd phase). In this regime, the

mutual repulsion among particles is overcome, and the colloidal layer starts to be ordered into a hexagonal close packed 2D colloidal crystal (A_{HCP} , Π_{HCP}). With further compression, the monolayer collapses (A_c , Π_c) and results in the formation of disordered bead multilayers and particle dispersion in the subphase (4th phase). Thus, the highest part of the HCP regime is normally the reference to transfer the colloidal monolayer on a solid substrate.

The obtained curve suggests that a short 2nd phase and larger 3rd phase allow a better arrangement of the 2D crystal and the quality of the film will be better if transferred at high SP. The identification of the area corresponding to SP suited for the transfer is also important. Indeed, it defines the maximum dimensions available for transfer, allowing an adequate cost-efficiency optimization. A minimum area in a range of 40-60 cm² and 30-40 cm² for the LB Mini-trough and Micro-Mini trough, respectively, is suitable for the preparation of a reasonable number of samples at the same time. By using these best conditions to transfer the colloidal film on a substrate, it has been possible to obtain large-scale coated areas with some defects but with a good organization of the 2D crystals (Figure 3.2).

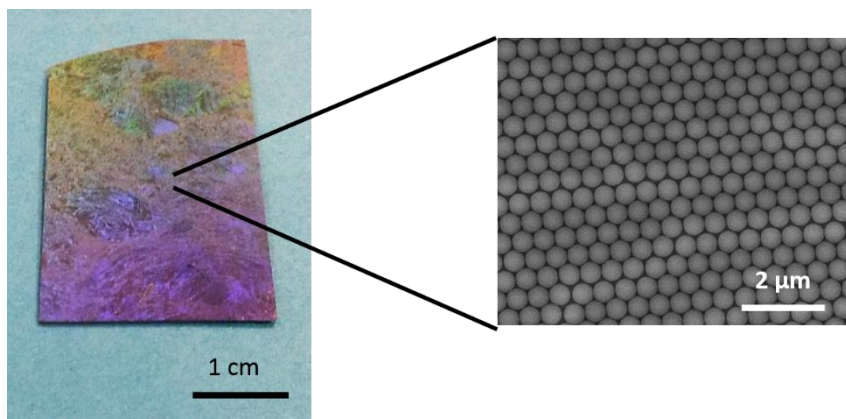


Figure 3. 2 - Colloidal monolayer (PS particles, $pH \phi = 500 \text{ nm}$) after LB transfer on silicon substrate.

Table 3.1 details the different characterization methods used to investigate the properties of the transferred film.

Table 3.1 – Methods of characterization and related information.

Method	Information
LB isotherm	2D, HCP transition
Optical and scanning electron microscopy	Film quality
Reflectance	Order, uniformity, density
Image processing	Mean crystal size, crystalline coverage %

SEM images of the film, transferred at different surface pressures within 2nd and 3rd phases, confirmed the progressive monolayer formation. Figure 3.3 shows that at increasing surface

pressure (6, 14, 22, 40 mN/m) the colloidal monolayer is more compact with bigger and ordered crystal domains.

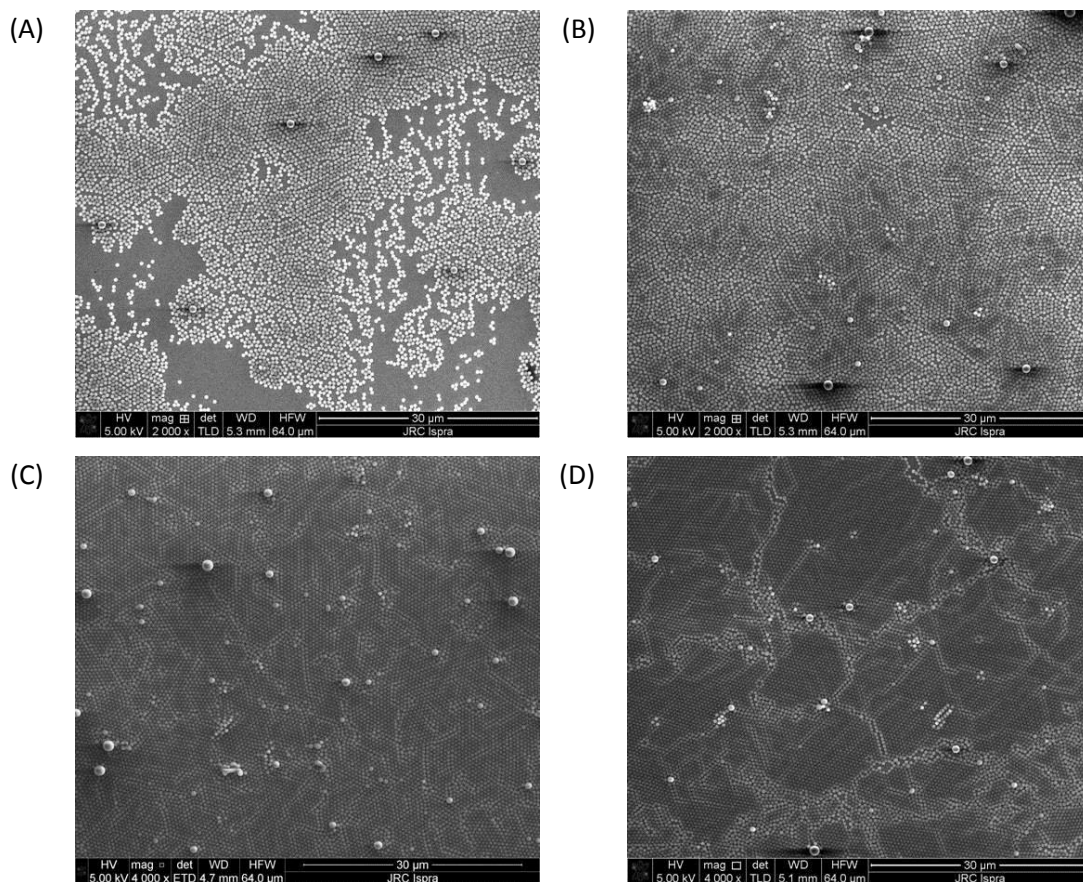


Figure 3. 3 - SEM images of the colloidal monolayer (PS particles, $\phi= 500$ nm) transferred on silicon substrate at different values of surface pressure. (A) 6 mN/m; (B) 14 mN/m; (C) 22 mN/m; (D) 40 mN/m.

Scale bar: 30 μ m.

If we observe at higher magnification the film transferred at 6mN/m, we can notice that some small crystal is already formed at this compression stage (Figure 3.4, left).

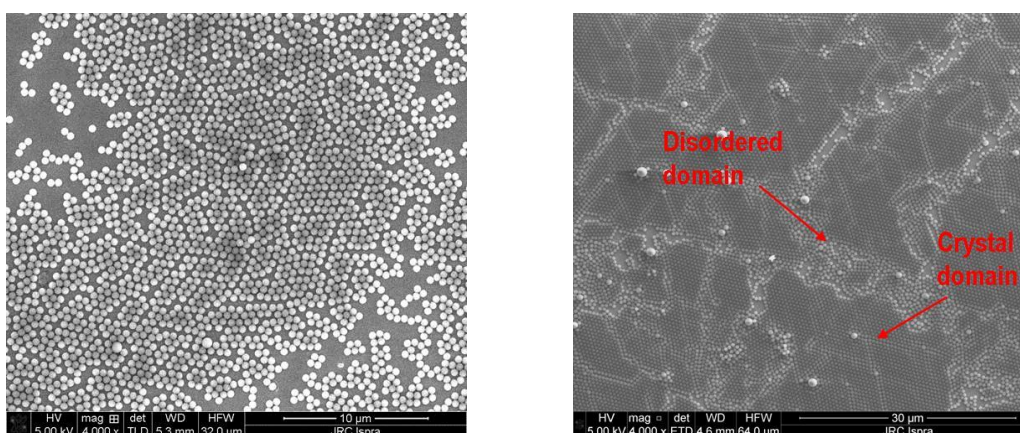


Figure 3. 4 - Disordered and ordered crystal domains at 6 mN/m (left) and 40 mN/m (right).

By going on with the barriers compression, these smaller crystals grow and present well defined crystal boundaries. The organization of the monolayers can be progressively increased by

increasing the transfer SP up to values of 40 mN/m. At that pressure, the heterogeneous colloids integrated in smaller domains are likely responsible for the inter-crystal disorder observed in samples, which implies that there is still a margin of improvement from the point of view of the processing of the starting colloidal particles.

The reflectance measurements (Figure 3.5) show that at increasing SP, the spectral features become more defined and pronounced, indicating a more ordered and dense arrangement of the monolayer. In particular, the reflectance minimum around 620-640 nm is due to diffraction and it is related to the lattice period: a deeper and narrower peak suggests a better ordered film. At low SP (6 mN/m) ordered domains and empty regions are present, resulting in broader spectral features. At intermediate values of SP, the monolayer is dense and uniform, while at higher SP (40 mN/m) the monolayer is slightly less uniform due to the presence of line defects (less pronounced reflectance minimum) but the film is more compact (reflectance minimum shifts towards lower wavelength suggesting a smaller lattice period).

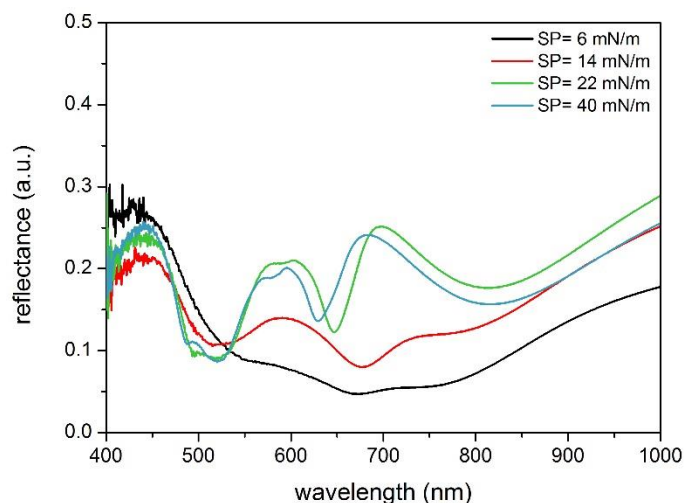


Figure 3.5 - Reflectance measurements of monolayers (PS particles, $\phi = 500$ nm) transferred on silicon substrate at different SP.

3.1.1 SUSPENSION RELATED PARAMETERS

In order to define the initial conditions for the formation of a 2D crystal, we investigated the LB isotherms obtained within a Mini-trough LB equipment for 500 nm PS particles with different combination of suspension-related parameters (Figure 3.6):

- Use of different spreading solvent; to improve the buoyancy of the particles, by using solvents with different degree of polarity.
- Percentage in volume of the spreading solvent; to obtain a better buoyancy of the particles and reduce their loss within the subphase.
- Volume of particle suspension; to identify a complete isotherm with reduced 2nd phase and/or high 3rd phase.

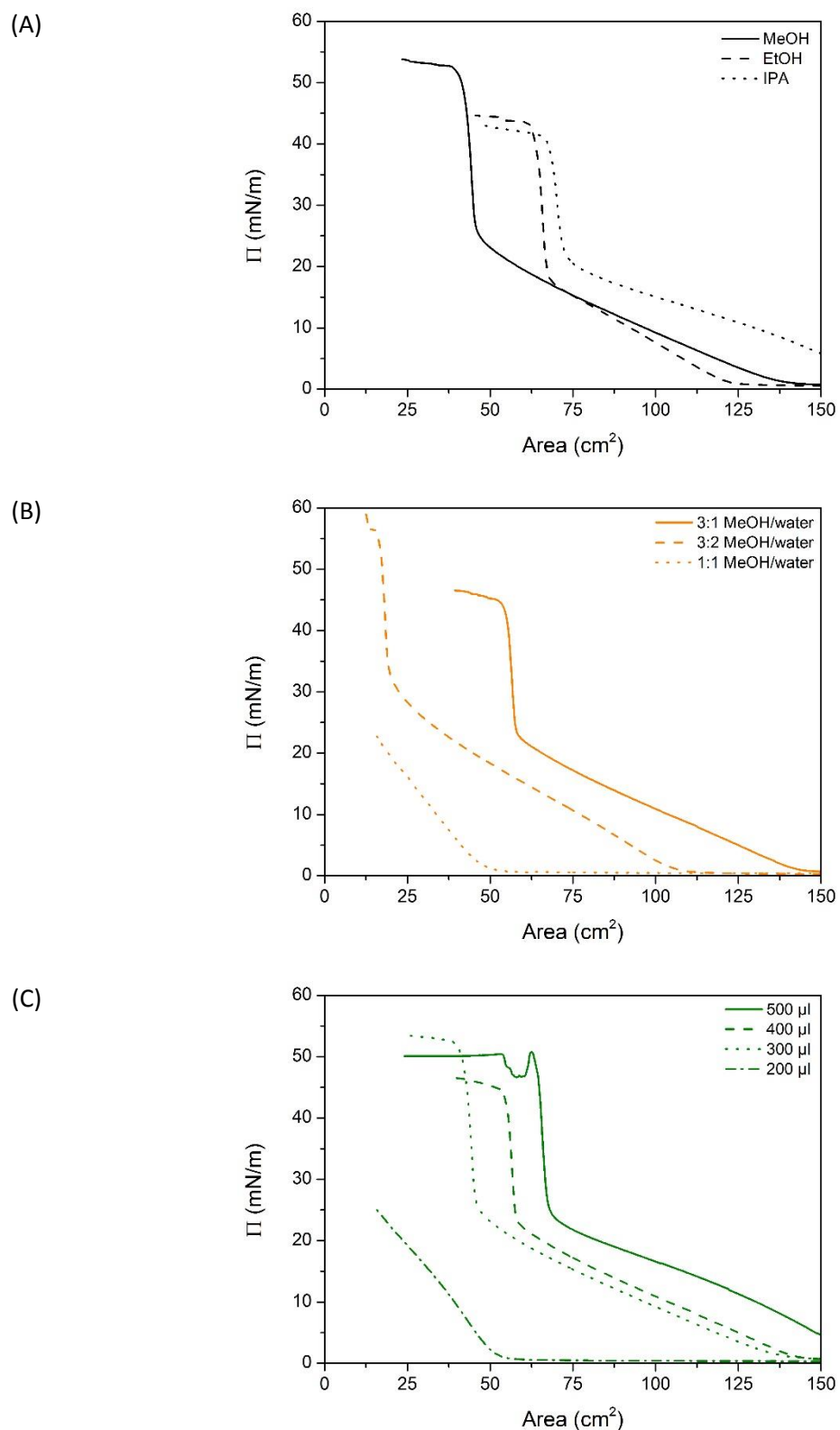


Figure 3. 6 - Isotherms corresponding to fixed particle diameter (PS particles, $\phi = 500$ nm) and different suspension related conditions. (A) Different spreading solvent, fixed suspension volume of 400 μl and spreading solvent/water ratio of 3:1 (MeOH: methanol, EtOH: ethanol, IPA: isopropanol). (B) Different percentage of the spreading solvent, fixed suspension volume of 400 μl and MeOH as spreading solvent. (C) Different volume of particle suspension, MeOH as spreading solvent and fixed spreading solvent/water ratio of 3:1.

Spreading solvent selection

A proper spreading solvent for the particle solution helps to avoid the material from dispersing in the subphase; it should be volatile to induce rapid elimination from the resulting monolayer and it should not dissolve the particles. Spreading solvents with different polarity (in decreasing order: methanol-MeOH, ethanol-EtOH, isopropanol-IPA) were tested (Figure 3.6 A). The volume suspension (400 μl) and the percentage of spreading solvent and water (3:1 v/v) were fixed in all experiments. By using the less polar solvent (IPA), we obtained isotherms with good shape but with high initial value of SP and lower values of the transition regime, resulting in a shorter 3rd phase, as compared with the other solvents in Figure 3.6 A. In fact, the lower polarity of IPA spreading solvent allows a reduced particle mixing with water in the trough and consequently a smaller amount of particles are lost into the aqueous subphase. As a drawback, a shorter rising part within the 3rd region results in a poorer controllability of their 2D arrangement with respect to MeOH or EtOH.

Spreading solvent percentage

The influence of the amount of the spreading solvent was also evaluated (Figure 3.6 B). We selected MeOH as spreading solvent and a fixed volume suspension of 400 μl , while the relative percentage of MeOH was decreased. At higher percentage of MeOH (MeOH/water 3:1 or 3:2 v/v), the transition into HCP occurs at higher value of area and SP, whereas with a 1:1 (v/v) ratio, it was not possible to obtain a complete isotherm and the latex particles did not order into a HCP monolayer. This result suggests that with a higher amount of spreading solvent, the colloids can easily float at the air-water interface and there is a smaller amount lost into the subphase.

Suspension volume

In these experiments (Figure 3.6 C), we used MeOH as spreading solvent in a ratio of 3:1 v/v with respect to water. We monitored the isotherm of different volumes of the particle solution (ranging from 500 to 200 μl) in order to optimize the balance of the particles used and obtain a suitable large area for the HCP transition. When high suspension volumes are used, the isotherm does not show the 1st phase but starts with a rising region. This result relates to a large amount of particles at the air-water interface and it suggests that, right after the deposition, the particles are already in contact with each other. By decreasing the volume of suspended latex beads (400 μl , 300 μl , 200 μl), the curve shows an initial horizontal tract (high surface area, SP close to zero) as an indication that the particles are not in physical contact. Besides, with a suspended volume of 400 and 300 μl the transition into a HCP occurs at lower values of area but similar value of SP with respect to those obtained with a volume of 500 μl , due to a smaller quantity of particles floating on the surface. With a suspended volume of 200 μl it was not possible to obtain a complete isotherm and the transition into a HCP structure did not occur.

3.1.2 DIFFERENT PARTICLE SIZE

The versatility of the LB technique offers the possibility to use particles with different diameters and made of different materials. We studied the formation of monolayers made of polystyrene beads with a nominal diameter of 400, 500 and 1000 nm within a LB trough (Figure 3.7).

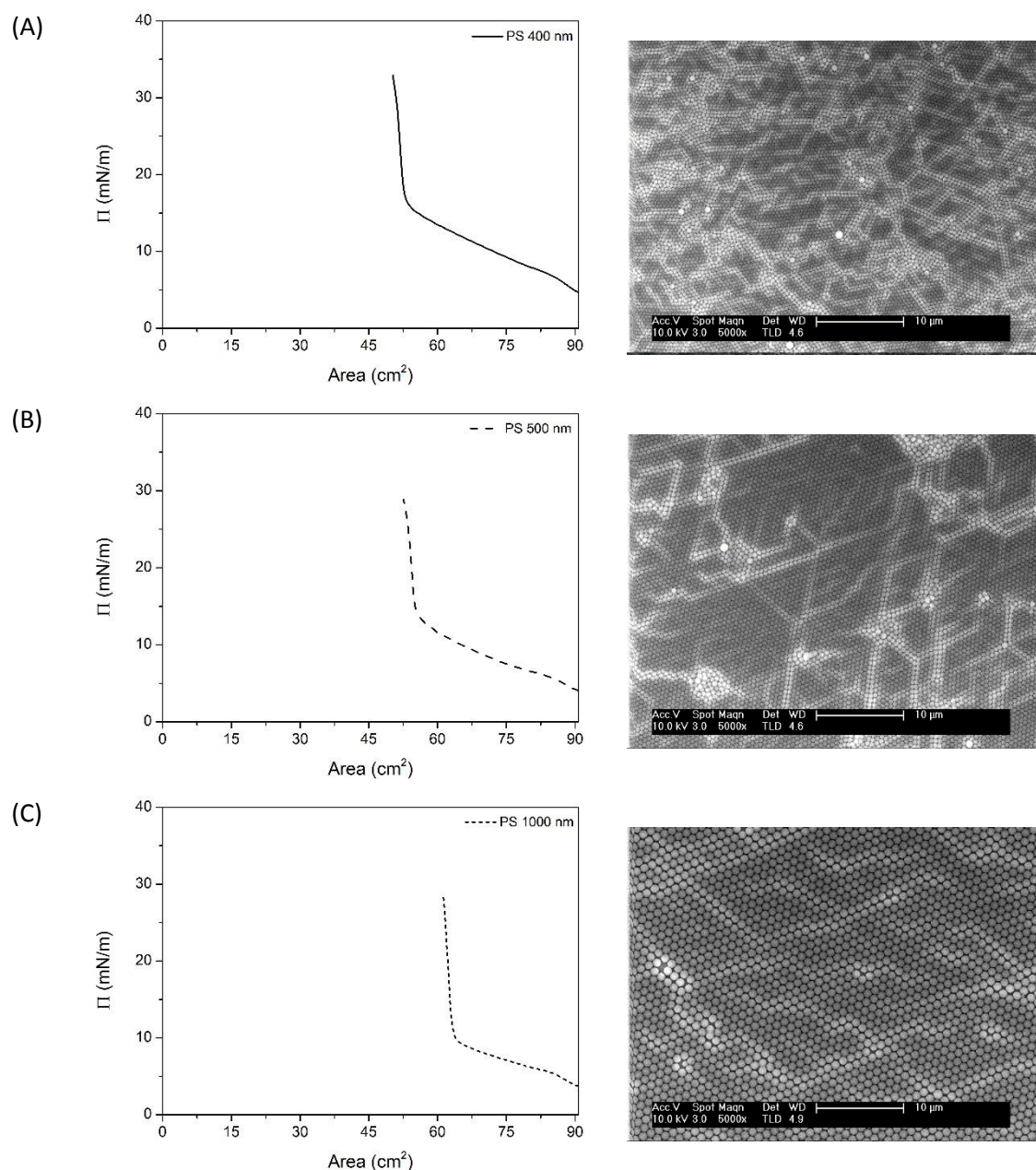


Figure 3. 7 - Isotherm and SEM images of monolayers made of PS beads with different sizes. (A) 400 nm; (B) 500 nm; (C) 1000 nm.

According to the results shown on the previous paragraph, we selected EtOH as spreading solvent, in a percentage of 3: 1 v/v with respect to water. The amount of the dispensed particles was scaled down according to the reduced dimensions of the LB model. In particular, for 400 and 500 nm particles the amount of the dispensed solution was 200 μ l, while for the 1000 nm particles was 100 μ l due to their increased buoyancy. Figure 3.7 shows the monolayer obtained

with each particle suspension and the isotherm related to the transfer. From SEM images, it is possible to notice that as the particle diameter increases the monolayer becomes more ordered and made of bigger crystal domains. As exposed in Chapter 2, this effect is due to a dominant contribution of electrostatic repulsive forces acting in case of bigger particles, which obliges the particles away from each other, resulting in an improved colloidal stability and a better control over their assembly under barrier compression. In case of small particles, the mutual repulsion is lower and the attractive forces are predominant (capillary forces and Van der Waals forces over long and short range, respectively), turning in the formation of a higher number of clusters after the spreading and, consequently, leading to a less controllable monolayer ordering.

3.2 CONTROL OVER PARTICLE ORGANIZATION

In order to improve the quality of the film, it is worth to influence the initial crystal formation. The aim is to disaggregate the smaller crystals formed at low SP and promote a better arrangement of beads with a reduced number of defects. Ideally, we want to decrease, the 2nd phase of the isotherm and increase the 3rd phase.

To control the defects on transferred film, we take into account several parameters:

- subphase pH;
- subphase temperature during the dispensing and/or the transfer of particle suspension (dispensing temperature, T_d and transfer temperature, T_t);

3.2.1 SUBPHASE pH

The PS particles used in all of these experiments have a charged surface (aldehyde and sulfate groups are present), therefore we investigated how their spreading behavior is affected by the pH of the water subphase[105]. At low pH value (i.e., high acid concentration), a protonation of the surface groups increases the particle buoyancy and, consequently, their concentration at the air-subphase interface. In this way, it is possible to use a reduced amount of particles and the loss of particles into the subphase is reduced as well. As a reference we consider the film obtained by spreading 400 μ l of bead suspension in standard conditions (particle ϕ = 500 nm, EtOH/Milli-Q 3:1 v/v), which means a T = 22°C and pure Milli-Q water as a subphase (pH slightly acid, around 6.5). As a testing condition, we selected several acid pH values: 2.1, 2.5, 2.8, 3.55. In the experiment at lowest pH (2.1), an amount of particle suspension around 50-100 μ l was sufficient to obtain the colloidal monolayer formation. An acid pH in the subphase strongly affects the isotherm shape. In Figure 3.8 are reported the isotherm curves obtained by using different acid pHs of the subphase. It is noteworthy that at pH 2.1 and 2.5 we obtained a curve characterized by two phases: an initial horizontal region (non interacting particles), followed by

an abrupt increase of the surface tension (HCP formation) within a steep region. As the pH value increases, we obtained curves more similar to standard condition, where four different phases are present.

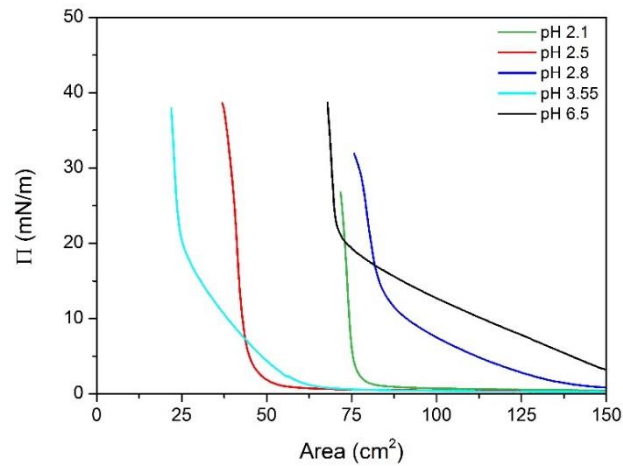


Figure 3. 8 - LB isotherm curves (PS particles, $\phi= 500$ nm) at different pH values of the LB trough subphase

Besides, we calculated the expected HCP area and number of particles for different amounts of spreading solution (Table 3.2); we also evaluated the real HCP area, as well as the particle loss into the subphase at different pH conditions (Table 3.3). In particular, once defined the solution volume, the loss was estimated as a ratio between the number of particles (NPs) corresponding to the real HCP area and the ones related to the expected HCP area.

$$NPs \text{ loss } \% = \frac{\# NPs_{exp} - \# NPs_{real}}{\# NPs_{exp}} * 100 \quad (3.1)$$

Table 3.2 – Expected values of HCP area and number of particles (PS particles, $\phi= 500$ nm) for different solution volumes and particle diameter of 500 nm.

V_s [μ l]	A_{HCP} [cm^2]	NPs_{exp}
450	502	2.32E+11
100	125	5.79E+10
75	94	4.34E+10

Table 3.3 – Real values of HCP area, number of particles and percentage of particle loss (PS particles, $\phi= 500$ nm) at different pH conditions.

pH value	V_s [μ l]	A_{HCP} [cm^2]	NPs_{real}	$NPs \text{ loss}\%$
2.10	75	75.99	3.51E+10	19.2
2.5	75	45.27	2.09E+10	27.8
2.8	100	83.73	3.87E+10	33.2
3.55	75	24.65	1.14E+10	73.8
6.5 (std)	450	70.82	3.27E+10	87.5

At low pH the requested amount of particles is decreased, as well as the percentage of the dispersed ones. Indeed, at acidic pH values of the subphase, the transition into HCP occurs around the expected value of area allowing the prediction of the exact amount of particles in relation with the dimensions of the sample on which we aim to transfer the monolayer.

In order to characterize the film obtained with acidic subphase, we made a LB transfer on silicon substrate and analyzed the samples by means of optical microscopy and SEM (Figures 3.9-3.10).

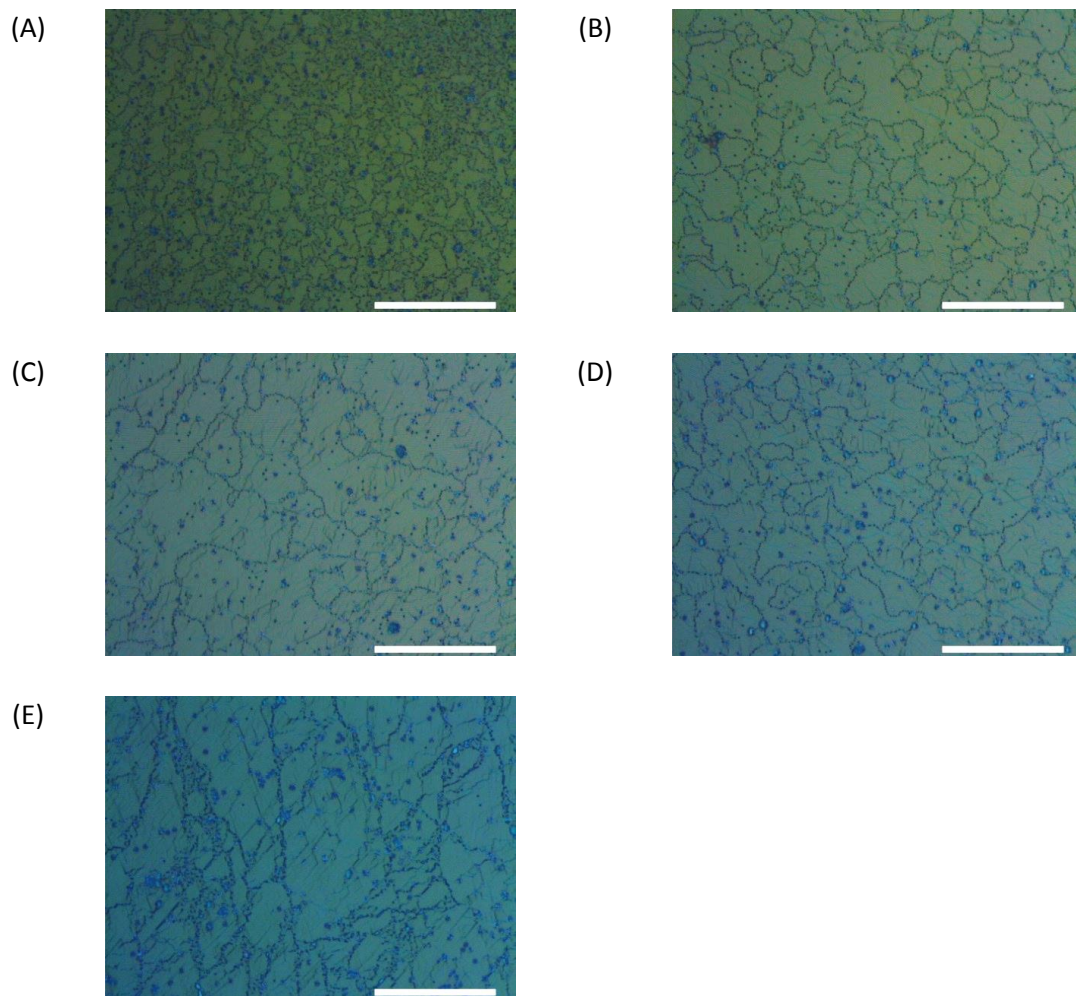


Figure 3. 9 - Optical images of monolayers (PS particles, $\phi= 500$ nm) transferred at different pH value of the water subphase. (A) pH = 2.1; (B) pH= 2.5; (C) pH = 2.8; (D) pH= 3.55, (E) pH= 6.5. Scale bar: 40 μ m.

The images show that, close to neutral pH, the particles arrange in big crystal domains with several defects. With an acidic subphase, the size of the crystals increases if the pH value is higher (2.8 -3.55).

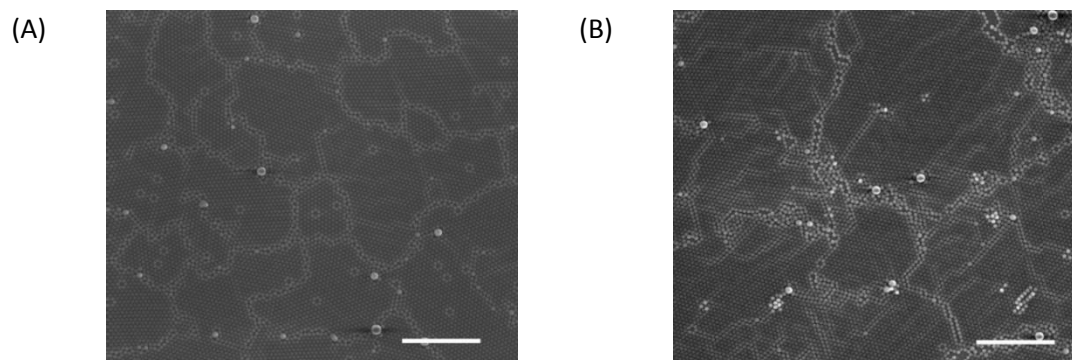


Figure 3. 10 - SEM images of the samples (PS particles, $\phi= 500$ nm) obtained at different pH value of the subphase. (A) pH= 2.5 (B) pH= 6.5. Scale bar: 10 μm .

Nevertheless, the average size of crystal domains is decreased if compared to neutral pH, but the defects are mainly localized at the boundaries. Furthermore, some other defects can be present, both missing sphere inside the domains and not ordered zones around crystalline areas. At the lowest pH (2.1), the monolayer is more uniform but less ordered and compact due to the presence of smaller crystal domains.

By image processing, it has been possible to analyse the transferred monolayer in terms of mean crystal area and percentage of crystalline coverage (Figure 3.11).

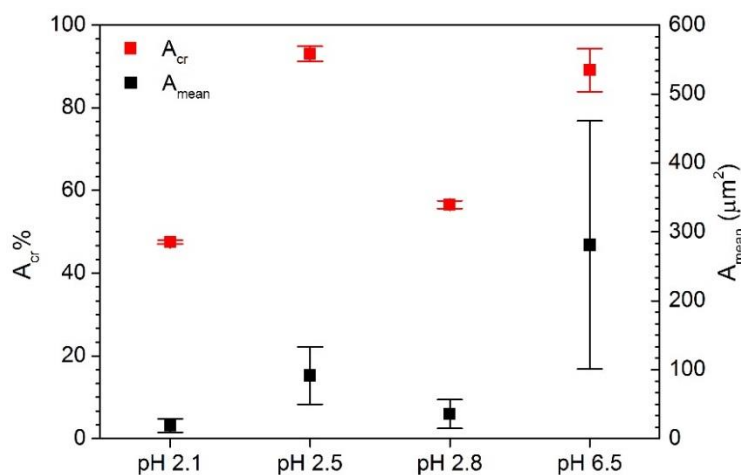


Figure 3. 11 - Percentage of crystalline area ($A_{cr}\%$) and average dimension of crystal domains (A_{mean}) derived from image processing for samples (PS particles, $\phi= 500$ nm) obtained at different pH values.

Figure 3.11 shows that at increasing pH values, the average dimension of crystal domains increases as well, but the high variability close to neutral pH indicates a lower uniformity. On the other hand, the area occupied by crystalline regions increases until a maximum and then decreases. This suggests that bigger crystals are more uniform but are accompanied by an increasing number of zones where the particles are not ordered. These results, together with the observation of the isotherm curve and the calculation of lost particles, allow noting that at acid pH (2.5-2.8) we can obtain the best arrangement between ordered films and optimize the

use of particles. However, it is worth to note that the highest mean crystal area has been obtained in standard condition.

Reflectance measurements (Figure 3.12) show broader and less pronounced peaks at pH=2.1, when the film is less ordered and dense. As the pH increases, the spectral features become deeper and better defined, suggesting a more compact and ordered arrangement of the particles. Except for the sample at lowest pH, all the others reproduce a very similar optical response and there is not a clear differentiating optical trend.

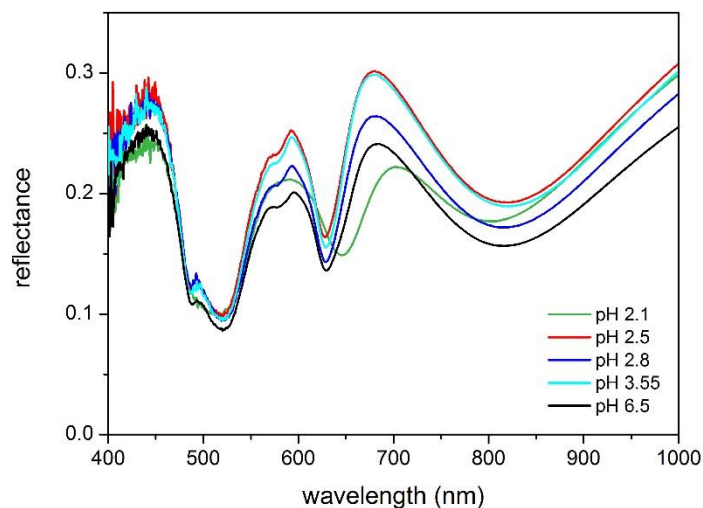


Figure 3. 12 - Reflectance measurements of colloidal monolayers (PS particles, $\phi= 500$ nm) transferred on silicon substrate at different pH of the subphase (2.1, 2.5, 2.8, 3.55, 6.5).

3.2.2 SUBPHASE TEMPERATURE

As aforementioned, we can also consider the temperature of the subphase as a parameter affecting the mobility of the particles and, consequently, the monolayer organization. For all the experiments, done at fixed pH (6.5), we used 400 μ l of polystyrene latex beads with a diameter of 500 nm, dispersed in a mixture of MeOH and water (3:1 v/v), by varying:

- The temperature of the subphase during the dispensing of the colloidal solution (T_d): 5°C, 22°C (standard), 50°C;
- The temperature of the subphase during the transfer of the monolayer (T_t): 5°C, 22°C (standard), 50°.

Dispensing temperature

The increase of the temperature during the dispensing phase might facilitate the dispersion of the particles into the subphase, because of the decreased surface tension of the water subphase (72.75 mN/m at 20°C and 67.94 mN/m at 50°C [140]). On the other hand, this effect is corrected by the increased evaporation rate of the spreading solvent at higher temperature, which transitionally improves the buoyancy of the particles.

Figure 3.13 shows the isotherms of the monolayer transferred at different dispensing temperature. At $T_d = 22^\circ\text{C}$, the isotherms are similar, but if the T_d is higher (50°C) the 2nd phase related to the 2D arrangement is longer and the transition is less abrupt: this is due to the higher mobility of the particles, which negatively affects their assembly while forced into contact.

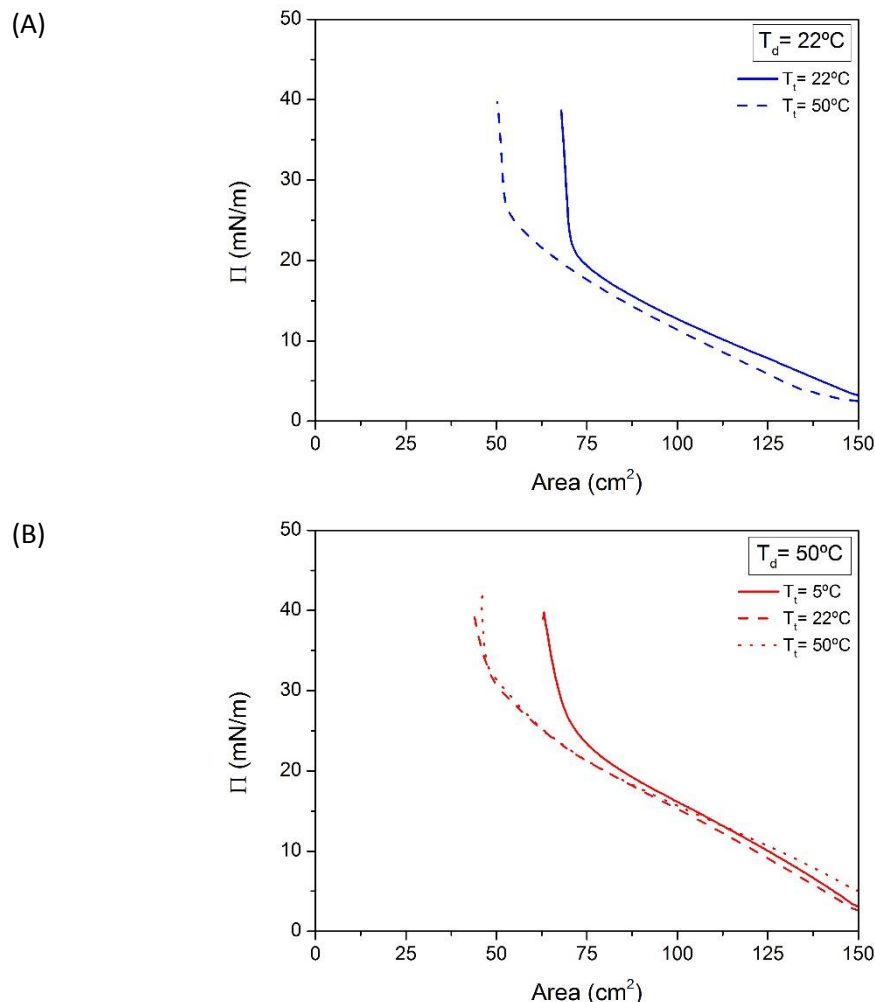


Figure 3. 13 - Isotherms (PS particles, $\phi = 500$ nm) obtained at different dispensing temperatures. (A) $T_d = 22^\circ\text{C}$, for T_t values of 22°C and 50°C ; (B) $T_d = 50^\circ\text{C}$, for T_t values of 5°C , 22°C and 50°C .

SEM images were processed to obtain information about crystalline coverage and mean crystal area (Figure 3.13-3.15). The results show that at low T_d and T_t , the quality of the film improves in terms of crystal domain order. At high T_t (50°C) there are more bead aggregates. When the T_d is high (50°C) the monolayer is characterized by smaller crystalline domains and smaller crystalline coverage. Indeed, at those elevated temperatures, the increased evaporation rate of the spreading solvent, together with increased kinetic effect, decreases the control over particles mobility and makes more difficult their arrangement. A more uniform distribution of the small crystal domains is obtained when T_t is low (5°C).

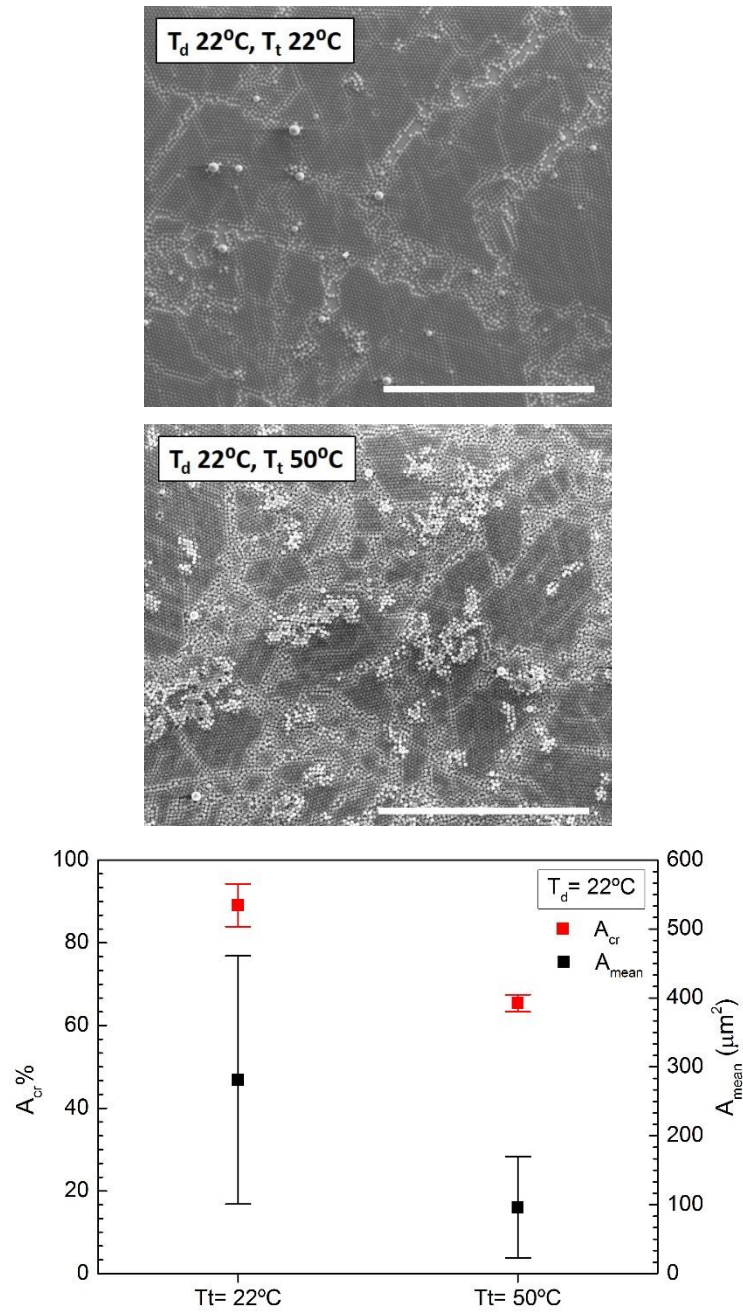


Figure 3. 14 - SEM images of samples (PS particles, $\phi = 500$ nm) obtained with $T_d = 22^\circ\text{C}$ and related percentage of crystalline area (A_{cr} %) and average dimension of crystalline domains (A_{mean}) derived from image processing. Scale bar: $30 \mu\text{m}$.

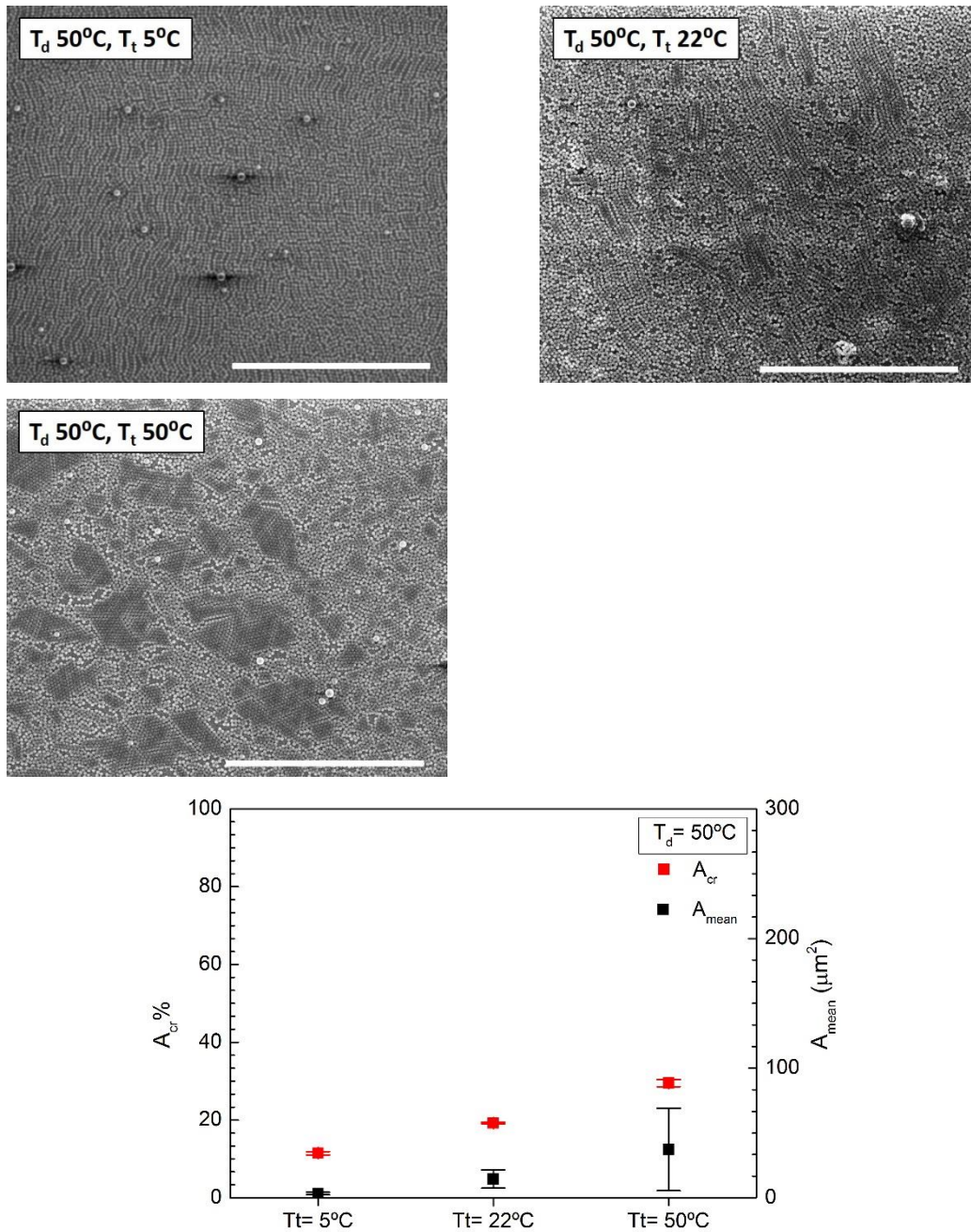


Figure 3. 15 - SEM images of samples (PS particles, $\phi = 500 \text{ nm}$) obtained with $T_d = 50^\circ\text{C}$ and related percentage of crystalline area ($A_{cr} \%$) and average dimension of crystal domains (A_{mean}) derived from image processing. Scale bar: $30 \mu\text{m}$.

Reflectance measurements (Figure 3.16) show broader and less defined spectral features at high T_d , as a confirmation of the decreased order of the system.

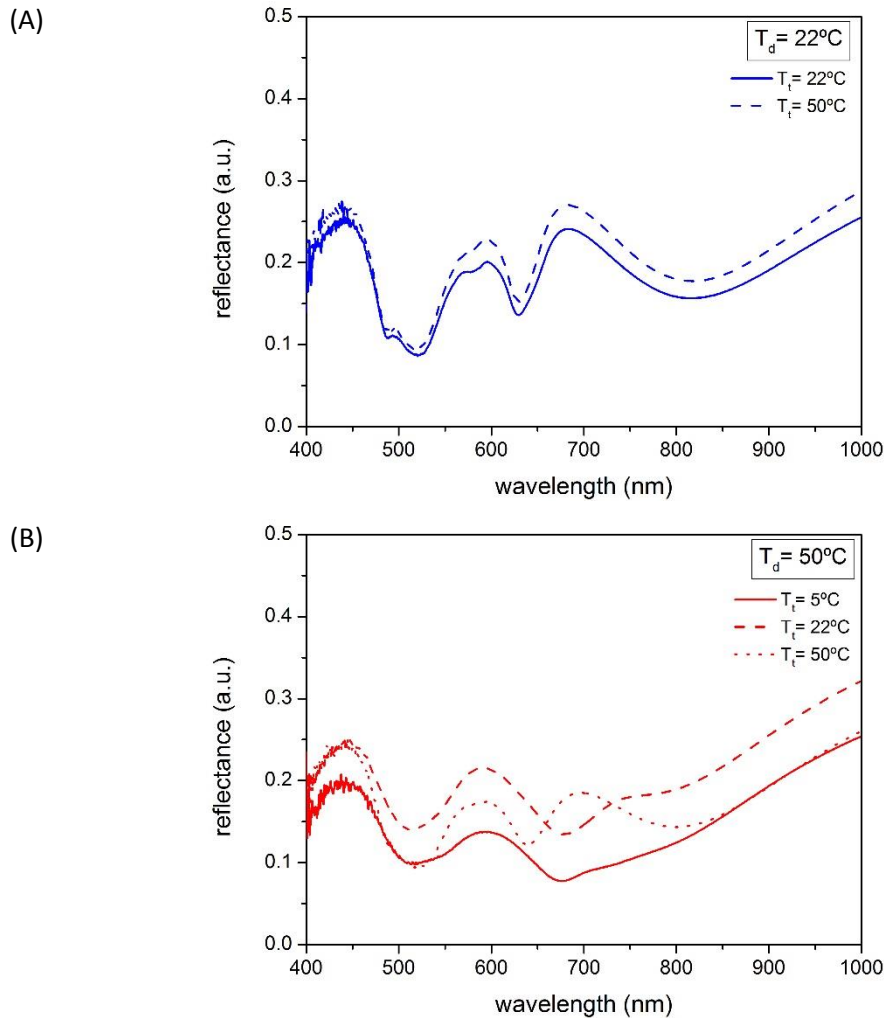


Figure 3. 16 - Reflectance measurements of monolayers (PS particles, $\phi= 500$ nm) transferred on silicon substrate at different T_d values. (A) $T_d= 22^\circ\text{C}$, for T_t values of 22°C and 50°C ; (B) $T_d= 50^\circ\text{C}$, for T_t values of 5°C , 22°C and 50°C .

Transfer temperature

Once the monolayer is obtained, the temperature set during the transfer can affect the quality of the colloidal film. A higher T_t should promote a faster solvent evaporation and increase mobility of the particles at the same time. Meanwhile, a lower T_t should confer higher rigidity to the film and favor its compactness. As reported in Figure 3.17, at $T_t= 5^\circ\text{C}$ or 22°C , the isotherm is better defined if the T_d is lower, while at $T_d= 50^\circ\text{C}$ the transition between 2nd and 3rd phase is less pronounced indicating a lower controllability of the 2D arrangement, probably due to a higher particle mobility. For $T_t= 50^\circ\text{C}$, the isotherms are more similar, but again the 2D arrangement phase is better defined if the T_d is lower.

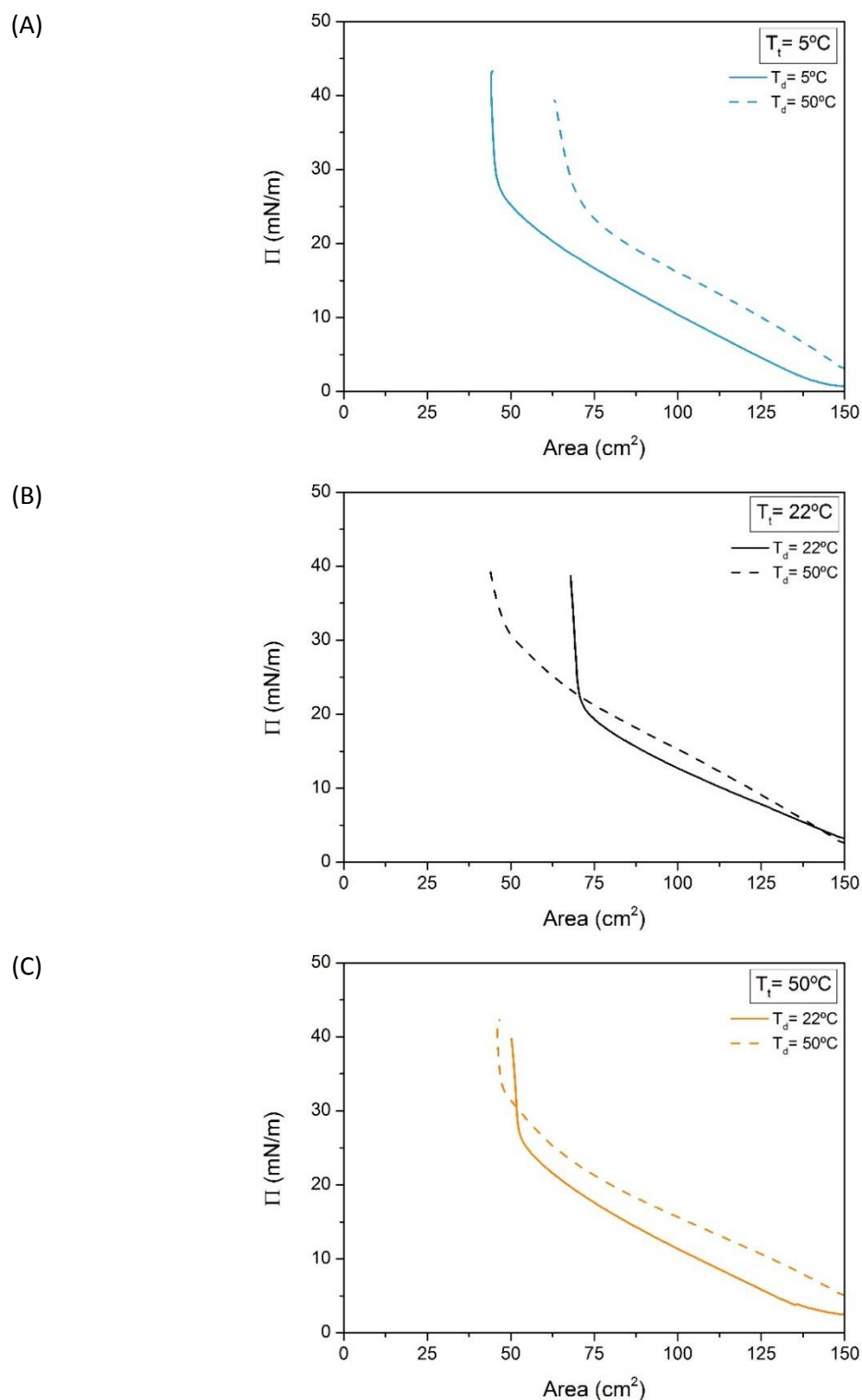


Figure 3. 17 - Isotherms (PS particles, $\phi = 500$ nm) obtained at different transfer temperatures. (A) $T_t = 5^\circ\text{C}$, for T_d values of 5°C and 50°C ; (B) $T_t = 22^\circ\text{C}$, for T_d values of 22°C and 50°C ; (C) $T_t = 50^\circ\text{C}$, T_d values of 22°C and 50°C .

SEM images validate the particle arrangement derived from the isotherm curves (Figure 3.18-3.20). If both T_d and T_t are low (5°C) the monolayer presents quite large crystalline domains with line defects mainly related to a higher rigidity of the film, while at high T_d (50°C) the domains are uniformly distributed but they are really small and with several empty spaces between them.

By increasing the dispensing temperature, we increase the mobility of the particles and this inhibits the crystal organization over large areas. At $T_t = 22^\circ\text{C}$, the best particle arrangement corresponds to $T_d = 22^\circ\text{C}$. If the T_d is higher, the monolayer is characterized by less compact small domains. For $T_t = 50^\circ\text{C}$, the quality of the film is poorer, there are bigger crystal domains with less ordered distribution and an increase of colloid clusters is observed.

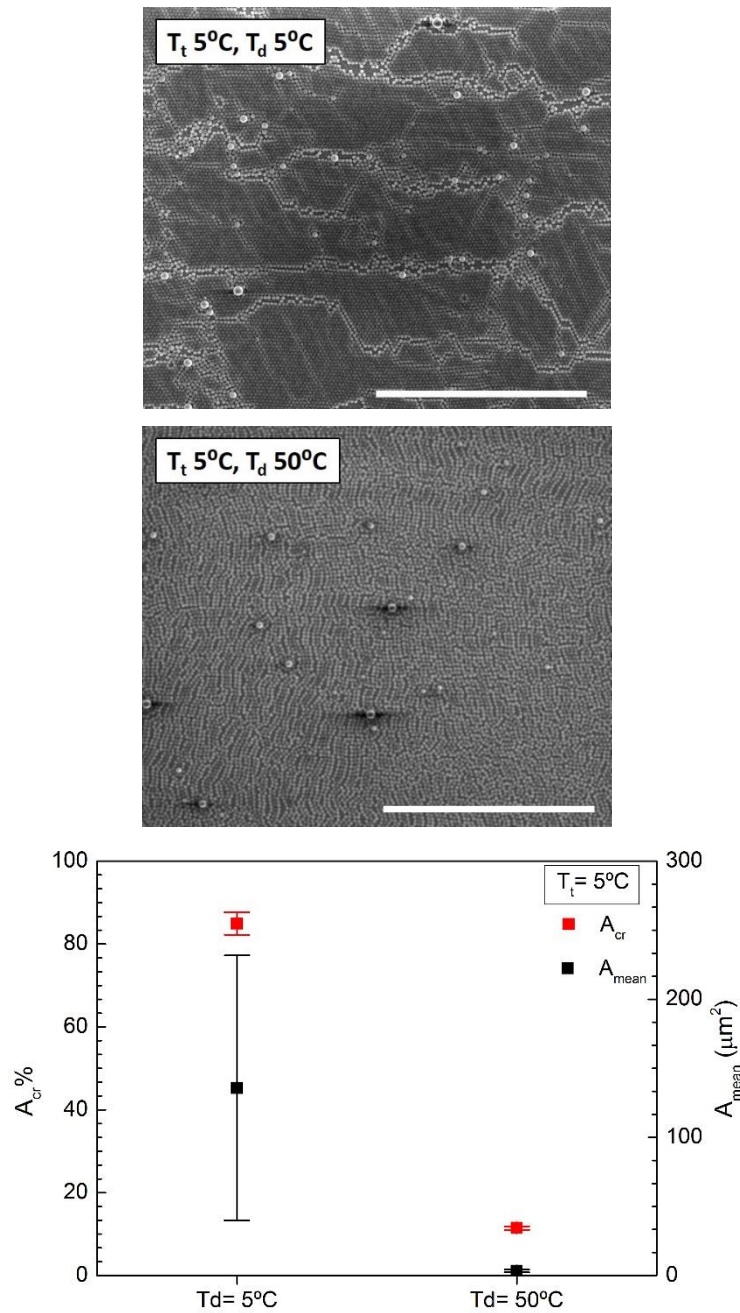


Figure 3. 18 - SEM images of samples (PS particles, $\phi = 500$ nm) obtained with $T_t = 5^\circ\text{C}$ and percentage of crystalline area ($A_{cr}\%$) and average dimension of crystal domains (A_{mean}) derived from image processing.

Scale bar: $30\ \mu\text{m}$.

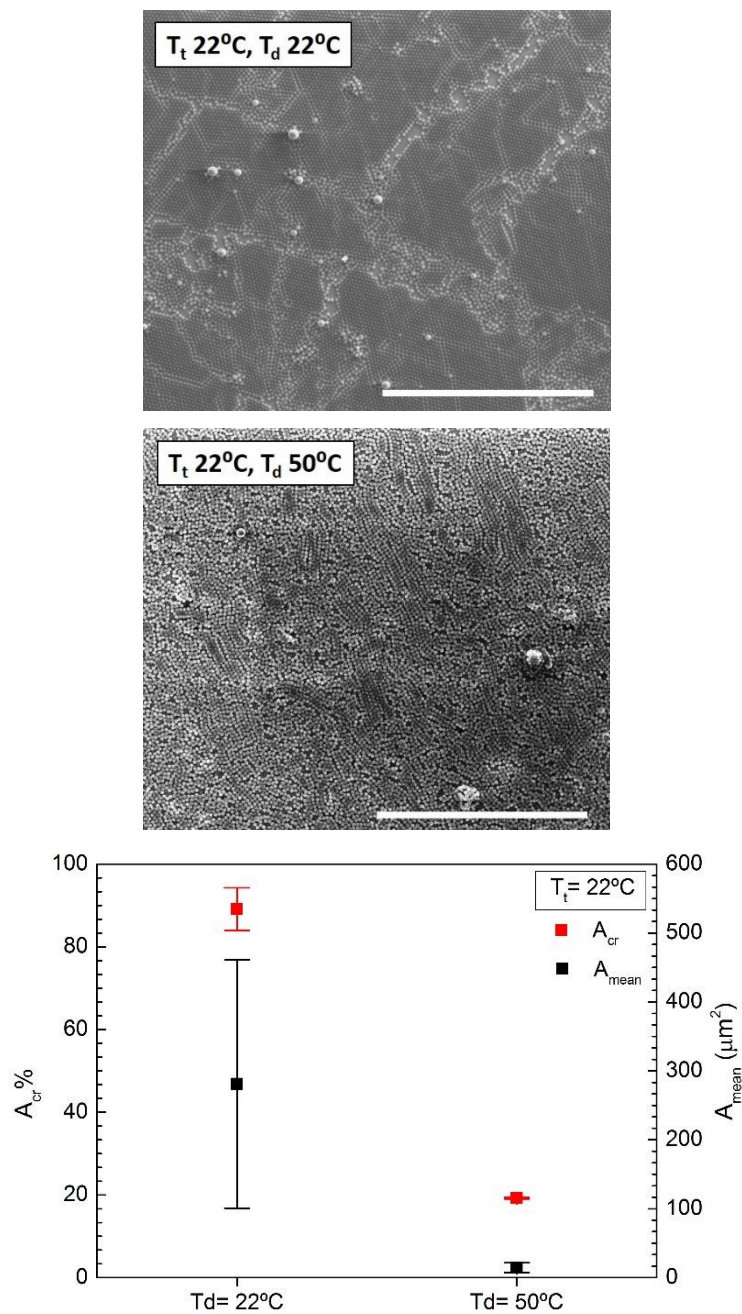


Figure 3. 19 - SEM images of samples (PS particles, $\phi = 500$ nm) obtained with $T_t = 22^\circ\text{C}$ and percentage of crystalline area ($A_{cr}\%$) and average dimension of crystal domains (A_{mean}) derived from image processing.

Scale bar: $30\ \mu\text{m}$.

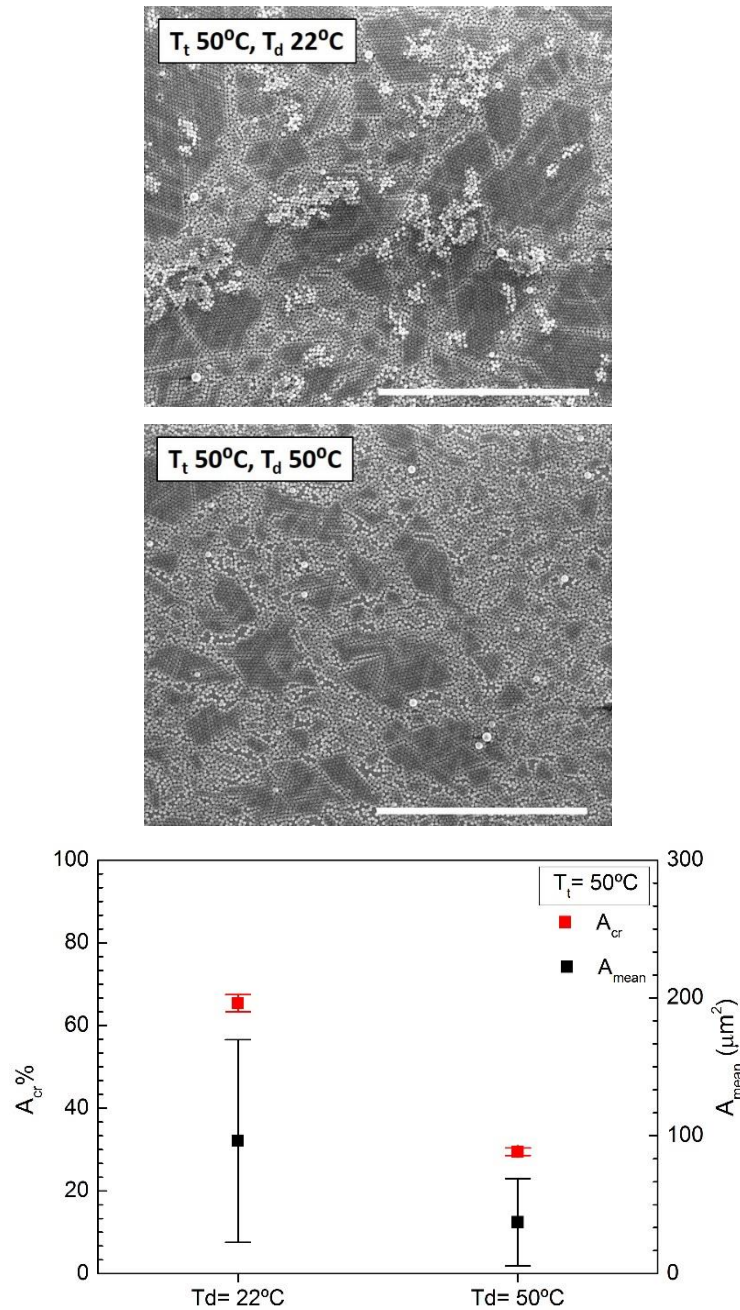


Figure 3. 20 - SEM images of samples (PS particles, $\phi = 500$ nm) obtained with $T_t = 50^\circ\text{C}$ and percentage of crystalline area ($A_{cr}\%$) and average dimension of crystal domains (A_{mean}) derived from image processing.

Scale bar: $30\ \mu\text{m}$.

From reflectance measurements (Figure 3.21) it is possible to notice a stronger influence of the dispensing temperature over the transfer temperature. Indeed, for all the tested values of T_t , the spectral features become less pronounced when $T_d = 50^\circ\text{C}$, indicating a less ordered and less compact monolayer.

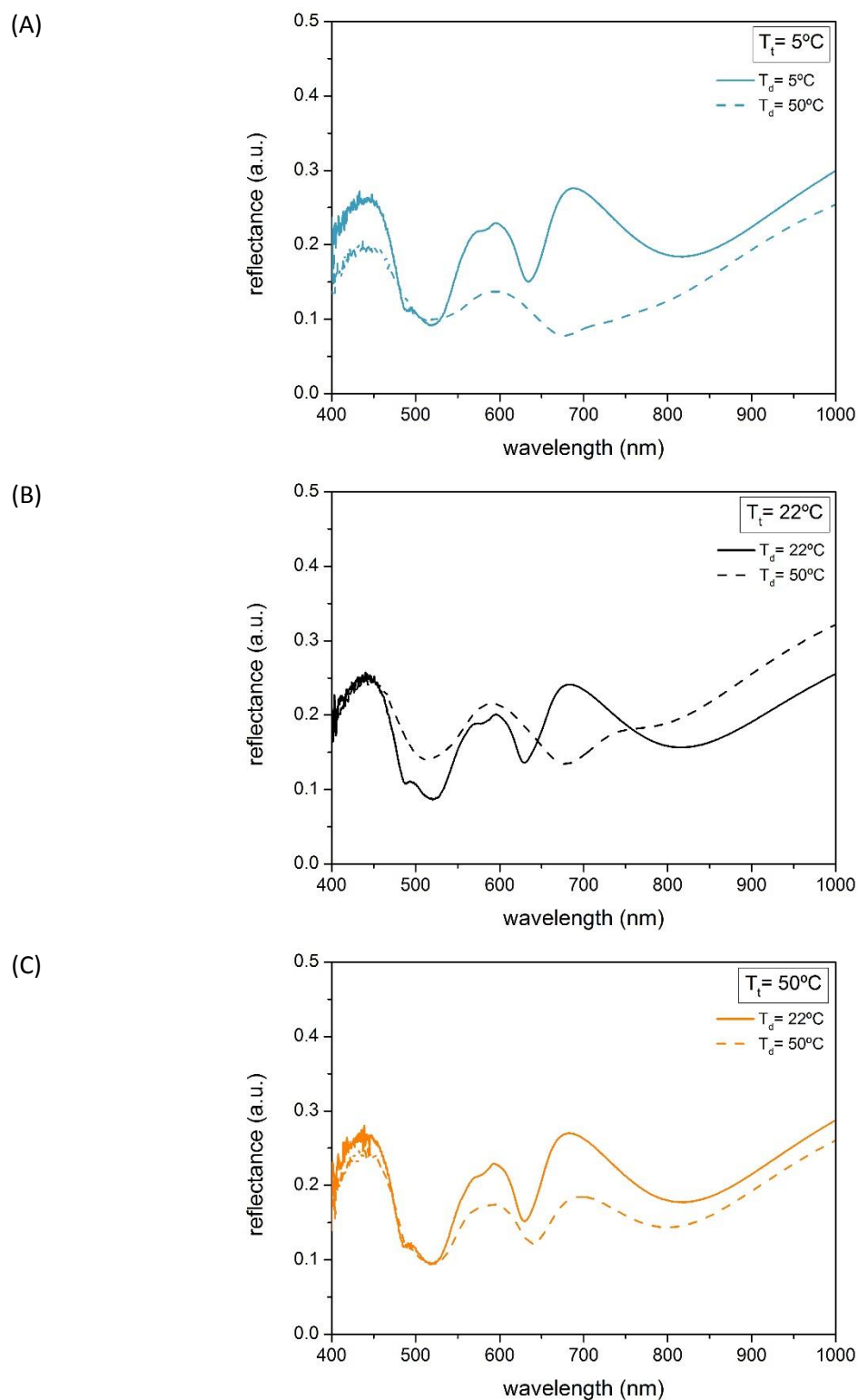


Figure 3. 21 - Reflectance measurements of monolayers (PS particles, $\phi = 500$ nm) transferred on silicon substrate at different T_t values. (A) $T_t = 5^\circ\text{C}$, for T_d values of 5°C and 50°C ; (B) $T_t = 22^\circ\text{C}$, for T_d values of 22°C and 50°C ; (C) $T_t = 50^\circ\text{C}$, for T_d values of 22°C and 50°C .

3.2.4 INORGANIC PARTICLE MONOLAYERS

As an alternative to organic particles, we studied the formation of colloidal monolayers made of SiO_2 particles with a nominal diameter of 1000 nm. An inorganic monolayer shows more

resistance to further etching process and is selectively etched by other reactive gasses, thus paving the possibility to nanostructure harder substrates (e.g., silicon and glass) with a high pillar aspect ratio. Moreover, SiO₂ particles offer a surface which can be easily functionalized by silane chemistry, providing a controllable and effective way to influence the colloidal buoyancy and the monolayer formation. XPS measurements are a useful tool to assess the successful outcome of the surface modification and functionalization.

Figure 3.22 shows the isotherm and monolayer corresponding to these SiO₂ particles (1% w/v, 400 μ l, EtOH/water 3:1).

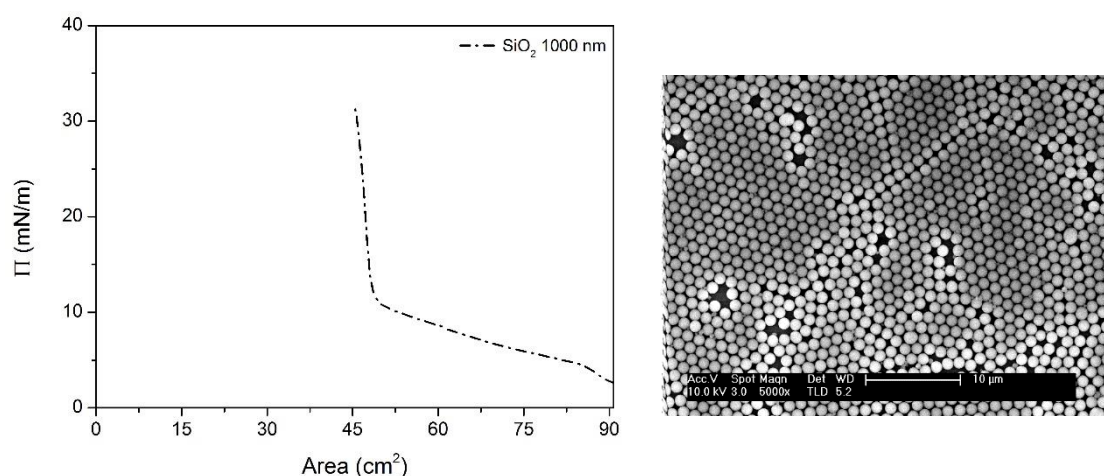


Figure 3. 22 - Isotherm and SEM images of monolayers made of SiO₂ particles ($\phi= 1000$ nm).

We also tested different activation and functionalization of these particles in order to improve their buoyancy and organization. The activation involved the redispersion of the particles in a 1% HF in water solution for 10' and, eventually, an oxidation step with H₂O₂ for other 10', followed by washing in water. As for the functionalization, we used a fluoro-silane coupling with perfluoro-octyl-triethoxysilane (PFOS, Sigma Aldrich): after activation, the particles were redispersed in a solution of 0.2% or 2% PFOS in EtOH and let react for 2h. After this process, the particles were washed in EtOH and then redispersed in the standard spreading solution (EtOH/water 3:1). The LB condition within the MiniMicro-trough were the same as for bare SiO₂ particles, but after surface activation and functionalization it was not possible to obtain a complete isotherm (Figure 3.23) since the transition to the formation of HCP clusters was reached in a very short change of total trough area. In case of activation of the particle surface with HF or HF/H₂O₂, the curves are very similar and after the 1st phase there is an elongated 2nd phase, suggesting a non-straightforward 2D arrangement, especially if compared with the isotherm of bare SiO₂ particles where the transition into 3rd phase is evident. The activation step probably induces a slightly higher polydispersity of the particle solution and affects the surface charge, making colloidal repulsive forces predominant when the particles are forced to coalesce. After the PFOS coupling, the isotherms start with higher values of SP, since the increase of the

particle hydrophobicity allows a better buoyancy, but also in this case the 2D arrangement is slower. At high silane concentration, the shape of the 2nd phase becomes even more irregular. This can be explained by an excessive and likely not homogeneous functionalization of the surface, which makes the particle interaction less controllable during their packing.

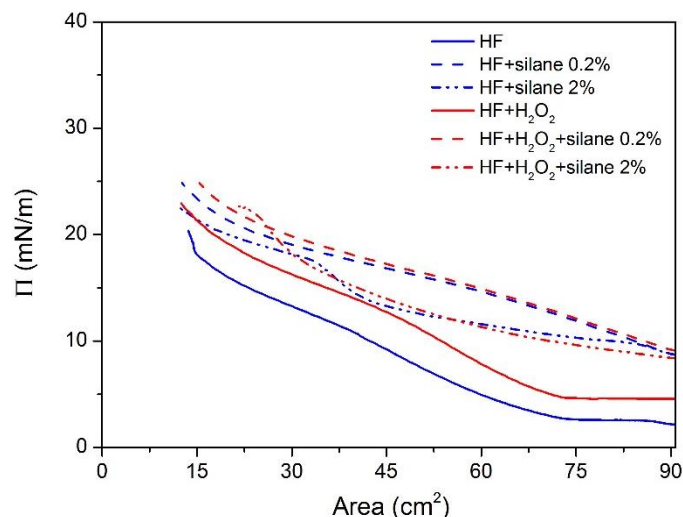


Figure 3. 23 – Isotherms of SiO₂ particles after activation and functionalization treatments.

The presence of fluorine groups in the XPS results confirms that activation and functionalization were effective. After the activation step, some F residual is present, but the amount increases after functionalization (Table 3.4). Due to a high amount of fluorine, just a few samples were analyzed in order to prevent a possible damage of the XPS equipment.

Table 3. 4 – XPS elemental composition of SiO₂ monolayers transferred on Ti substrates after different surface treatments.

	C 1s	O 1s	Si 2p	F 1s
<i>SiO₂ beads (bare)</i>	15.11	48.97	35.90	-
<i>SiO₂ beads + HF</i>	27.99	42.91	27.72	1.36
<i>SiO₂ beads + HF/H₂O₂</i>	29.69	43.25	25.77	1.28
<i>SiO₂ beads + HF + PFOS 0.2%</i>	44.30	36.58	12.80	6.31

The energy scale was calibrated by setting the C1s hydrocarbon peak to 284.8 eV and core level spectra for C1s and Si2p are reported in Figure 3.24. In case of bare SiO₂ particles, the C1s peak can be fitted with three components: C0 at 284.8 eV related to C-C/C-H bonds, C1 at about 286 eV relative to C-O bonds and C2 at about 288 eV related to C=O bonds. These last two peaks are due to some residual from the synthesis of the particles. The Si2p core level spectrum shows the presence of oxidized states of Si. The main component of the fit (Si 2pOx2 at about 103.5 eV) is related to SiO₂ compound, while the other one (Si 2pOx1 at about 102 eV) can be ascribed to partially oxidized state, such as SiOx compound. After HF treatment and PFOS 0.2%

functionalization, a new component at higher binding energy (at about 289 eV) is introduced to fit the C1s peak, which can be ascribed to carbon-fluorine bonds of the silane structure. As for the Si2p spectrum, in addition to the component related to SiO₂ compound, it is possible to notice a Si 2pOx1 component at around 100 eV, likely related to SiOxC and SiFC bonds associated to silane binding.

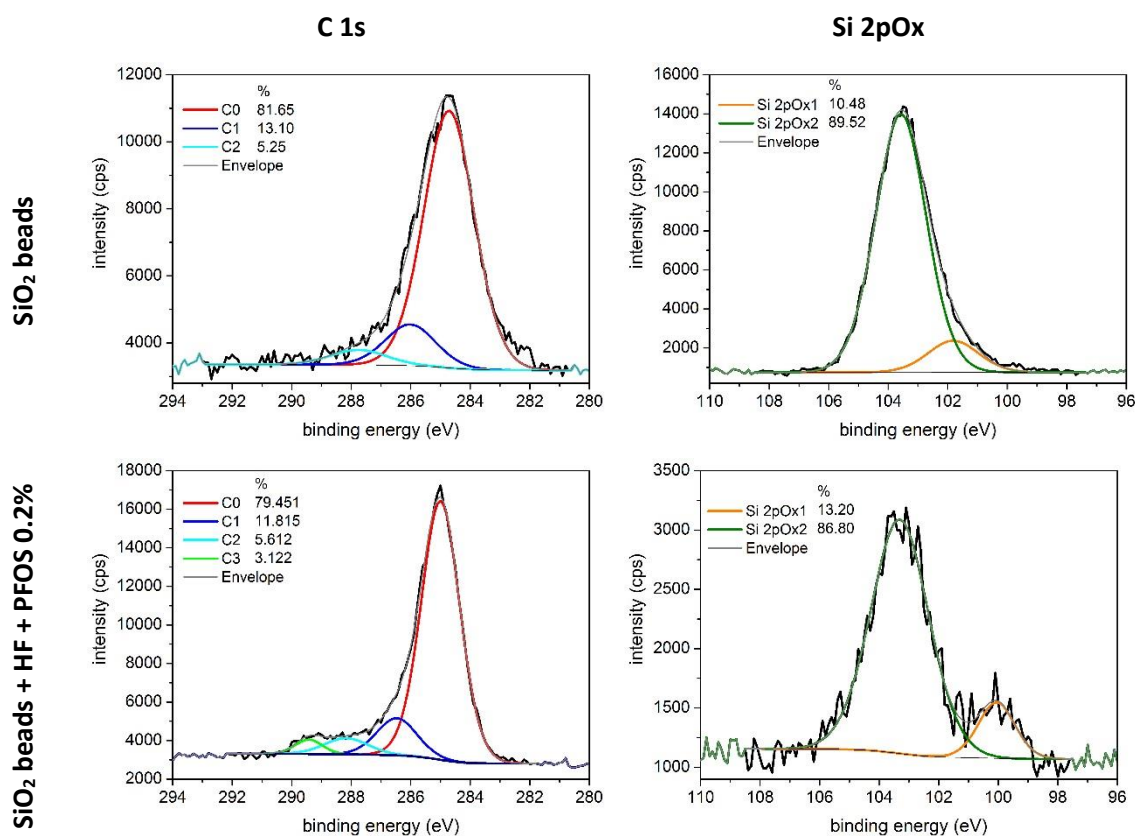


Figure 3.24 – XPS core level spectra of C 1s and Si 2pOx for samples made of bare SiO₂ beads (top) and SiO₂ beads treated with HF and PFOS 0.2% (bottom).

For the analysis of SEM images, it has to be taken into account that the transfer on solid substrate was done approximately at the same value of SP (20-25 mN/m) for all the activated and functionalized samples, but the isotherm did not reach the HCP phase. Consequently, a poor quality of the particle assembly can be explained with a transfer in a non-ideal region. SEM images show a better organization of the monolayer in absence of activation and functionalization or for functionalization at high silane concentration after HF/H₂O₂ activation (Figure 3.25).

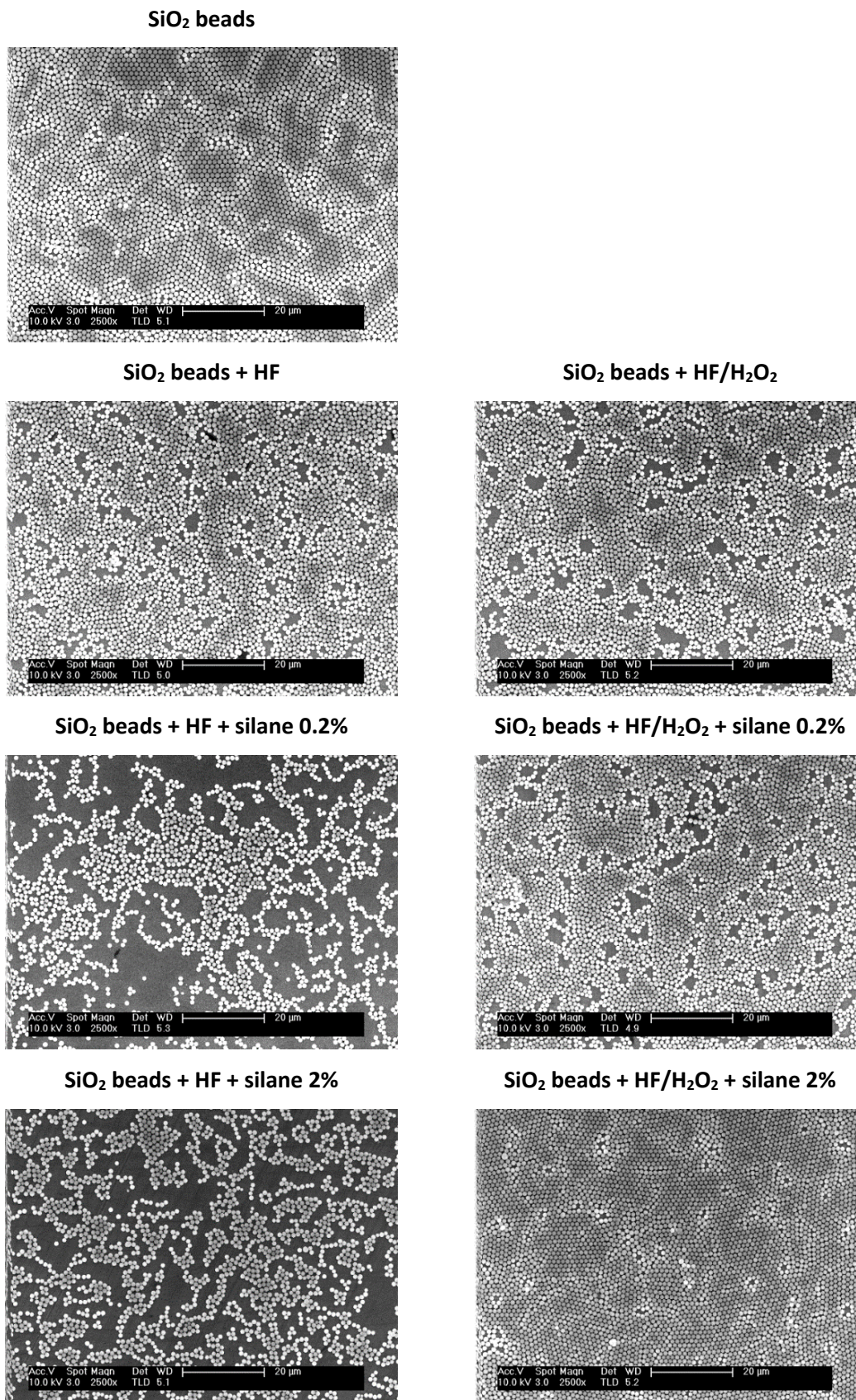


Figure 3. 25 – SEM images of monolayers on silicon substrates made of bare SiO_2 beads and treated SiO_2 beads.

This suggests that the surface treatment can be useful for an improved buoyancy of the particles, but in overall it does not improve the monolayer formation because it leads to small particle islands that do not assemble into continuous monolayers. In case of activation with HF/H₂O₂, the oxidation of the surface allows an increased silane coupling, which results in a better organization of the monolayer and in a slightly anticipated transition within the isotherms, as previously shown.

3.3 CONCLUSIONS

We investigated the LB isotherms obtained by combining different suspension-related parameters. The LB process was successfully optimized for PS particles with different diameters (400, 500 and 1000 nm) and EtOH (in a ratio 3:1 with respect to water) was selected as efficient spreading solvent in view of a better particle buoyancy and control over 2D arrangement. Once these initial conditions were defined, we aimed at decreasing the defects in the monolayers to improve the quality of the transfer on solid substrates. We investigated the peculiar effect of varying the subphase-related parameters (pH, temperature) on the microcrystalline structure of the transferred colloidal films. A pH of 6.5 of the LB subphase and a process temperature of 22°C (both for the monolayer assembly and the transfer on solid substrate) were selected to obtain large area coated surfaces made of well-ordered and compact crystalline domains.

The assembly of inorganic monolayers made of SiO₂ beads (1000 nm as nominal diameter) was also evaluated. These particles were successfully treated by HF or HF/H₂O₂ activation and functionalized by fluoro-silane coupling. The surface treatment (including both activation and functionalization) is useful to improve the buoyancy of the particles, but the monolayer assembly results in a better organization only when bare particles or particles functionalized after HF/H₂O₂ activation are considered.

CHAPTER 4

PLASMONIC SURFACE PROCESSING

This chapter details the development of an active plasmonic surface [141], focusing on the fabrication steps complementary to the monolayer growth described in Chapter 3. The flexibility of the fabrication process offers high versatility in view of the integration of these surfaces with optical and electronic components.

If not differently indicated, all the samples were made on glass and reflectance measurements were collected with light impinging from substrate side. The bulk sensitivity of the final plasmonic surface was assessed by testing different refractive index changes. A preliminary evaluation was done considering spectra in Milli-Q water with respect to air (refractive index of 1.33 and 1, respectively). A characterization to smaller variations of refractive index refers to spectra acquired in a solution with a fixed refractive index of 1.336 (referred as “fixed solution” in this Chapter; glycerol 4% in Milli-Q or ethanol 20% in Milli-Q, to overcome the problem of residual sticky glycerol) with respect to Milli-Q water.

4.1 DIFFERENT COLLOIDAL MONOLAYERS AS SACRIFICIAL MASKS

4.1.1 PITCH INVESTIGATION

A different pitch of the colloidal mask results in a different optical behaviour of the plasmonic surface, in terms of peak position and sensitivity. We investigated samples made on glass with ppAA and gold layers at the same nominal thickness and using PS beads of different diameters (400, 500 and 1000 nm) as colloidal monolayers, according to the process summarized in Chapter 2 (Figure 2.1). Samples made with 400 and 500 nm beads were processed under the same conditions: 150 nm of ppAA as polymeric layer, 4' of O₂ plasma etching and 150 nm as nominal thickness for the gold deposition. In case of 1000 nm beads, polymer and gold layers had the same nominal thickness of 200 nm and the O₂ plasma was set to 5'. Indeed, the bigger diameter of the particles justifies a slightly higher ppAA layer and a longer etching time, in order to obtain a reasonable etching of the beads and consequently a proper nanostructure within the

underlying polymeric layer. Figure 4.1 A shows the reflectance in air (solid line) and in Milli-Q water (dashed line) of the surfaces obtained with the three different colloidal monolayers. The spectra in air related to 400 and 500 nm pitch present a similar behaviour, characterized by a main maximum (around 600 and 690 nm, respectively) and a deep minimum (around 750 and 830 nm, respectively). The spectrum in air related to 1000 nm pitch shows a more complex behaviour with a maximum around 700 nm and two sequential minima around 750 and 840 nm. The ratio between reflectance in Milli-Q water and air (Figure 4.1 B) gives an indication of the sensitivity of the surface to bulk refractive index change and allows identifying the regions of the spectra with higher sensitivity.

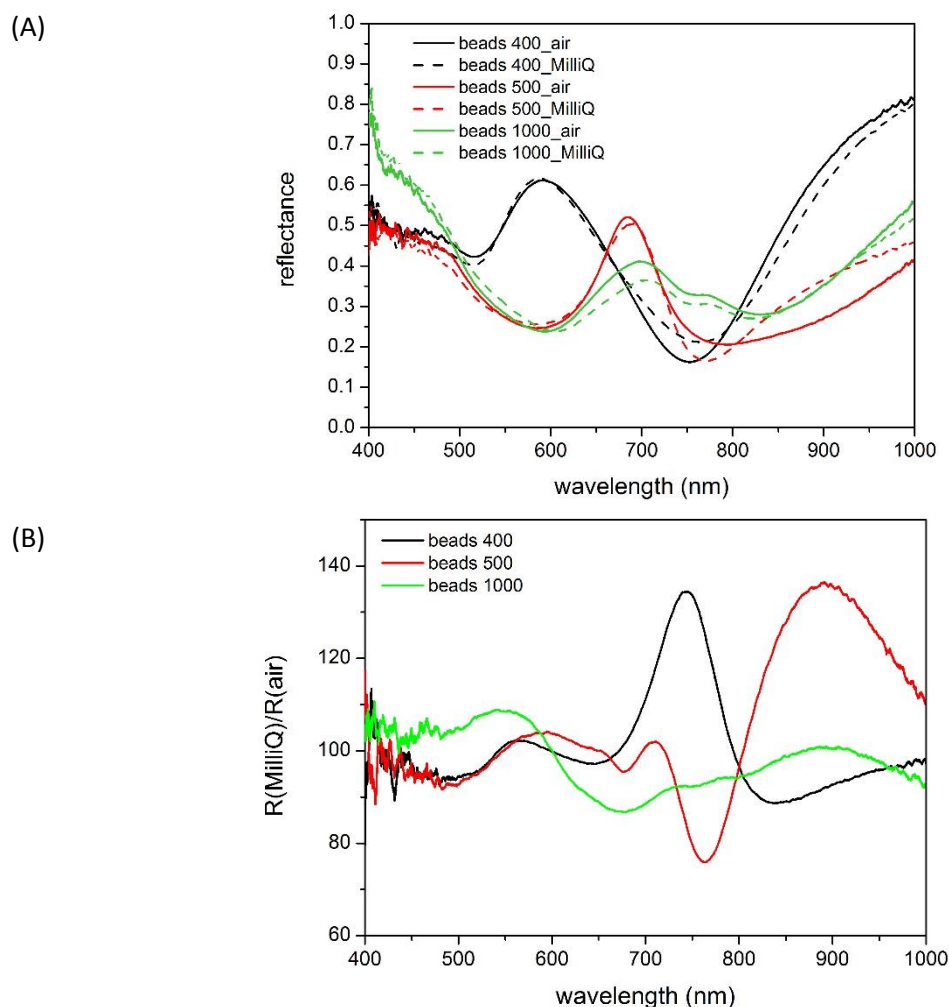


Figure 4. 1 – (A) Reflectance spectra in air (solid line) and Milli-Q water (dashed line) of samples made with 400, 500 and 1000 nm pitch. (B) Ratio of the reflectance spectra in Milli-Q water to reflectance spectra in air.

In case of 400 and 500 nm pitch, it is possible to notice a well-defined peak related to positive refractive index change of approximately 30% located around 750 and 900 nm, respectively. On the other hand, the surface made with a pitch of 1000 nm does not show a region with high bulk sensitivity, but just a low variation to refractive index change around 900 nm. High sensitivity to

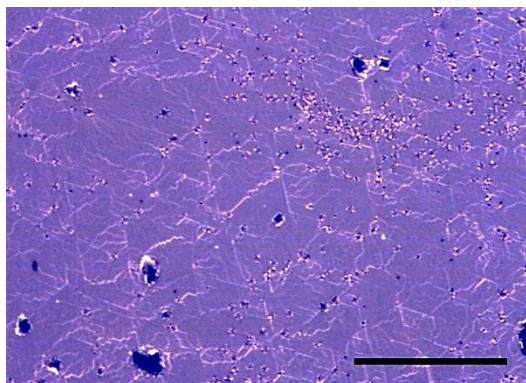
refractive index change in the Vis-NIR range, where normally optical components perform best, was considered as the eligibility criterion to select the more promising surface for sensing application.

4.1.2 COLLOIDAL MONOLAYERS AT DIFFERENT pH

These samples were fabricated using the same parameters (150 nm of ppAA, colloidal monolayer of 500 nm beads, 4' O₂ plasma etching, 150 nm of gold), except for the condition of the subphase during the LB process. The standard pH (6.5) and low pH (2.5) were tested according to the results presented in Chapter 3. After the lift off of the particles, a cleaning of the surface was performed to reduce any possible contamination by means of a combination of wet and plasma etching.

The optical images in Figure 4.2 show the plasmonic surfaces related to a different organization of the monolayers, with bigger crystal domains when a pH of 6.5 is considered. Samples transferred at low pH show smaller crystal domains in good agreement with the results presented in Chapter 3, but lots of defects are also present within the ppAA layer likely due to a negative effect of the acid pH of the LB subphase on the ppAA stability.

(A)



(B)

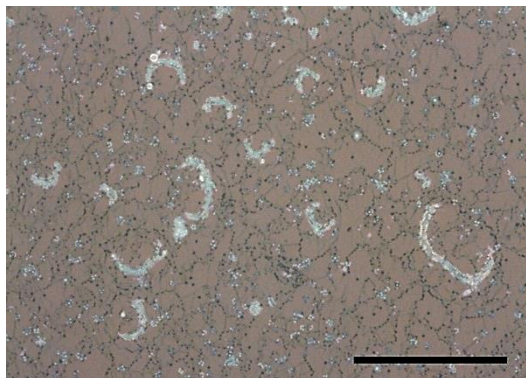


Figure 4. 2 – Plasmonic surfaces related to colloidal monolayers (PS particles, $\phi= 500$ nm) obtained with different pH of the LB subphase. (A) pH 6.5; (B) pH 2.5. Scale bar: 40 μ m.

For each batch, the reflectance spectra in air of three samples have been reported to show the reproducibility of the optical behaviour (Figure 4.3 A-B). In both cases, the position of the peaks

are similar with a strong maximum at around 700 nm and a deep minimum around 850 nm, but they are better defined in shape when the standard pH (6.5) is considered. Indeed, when the monolayer is self-assembled at low pH, the surface is made of smaller crystal domains with a narrower distribution, but the presence of abundant domain boundaries is probably responsible for a less reproducible optical response. As a consequence, when the sensitivity to refractive index change is tested, it is possible to notice a better reproducibility in terms of peak position and shape for the samples made at standard pH.

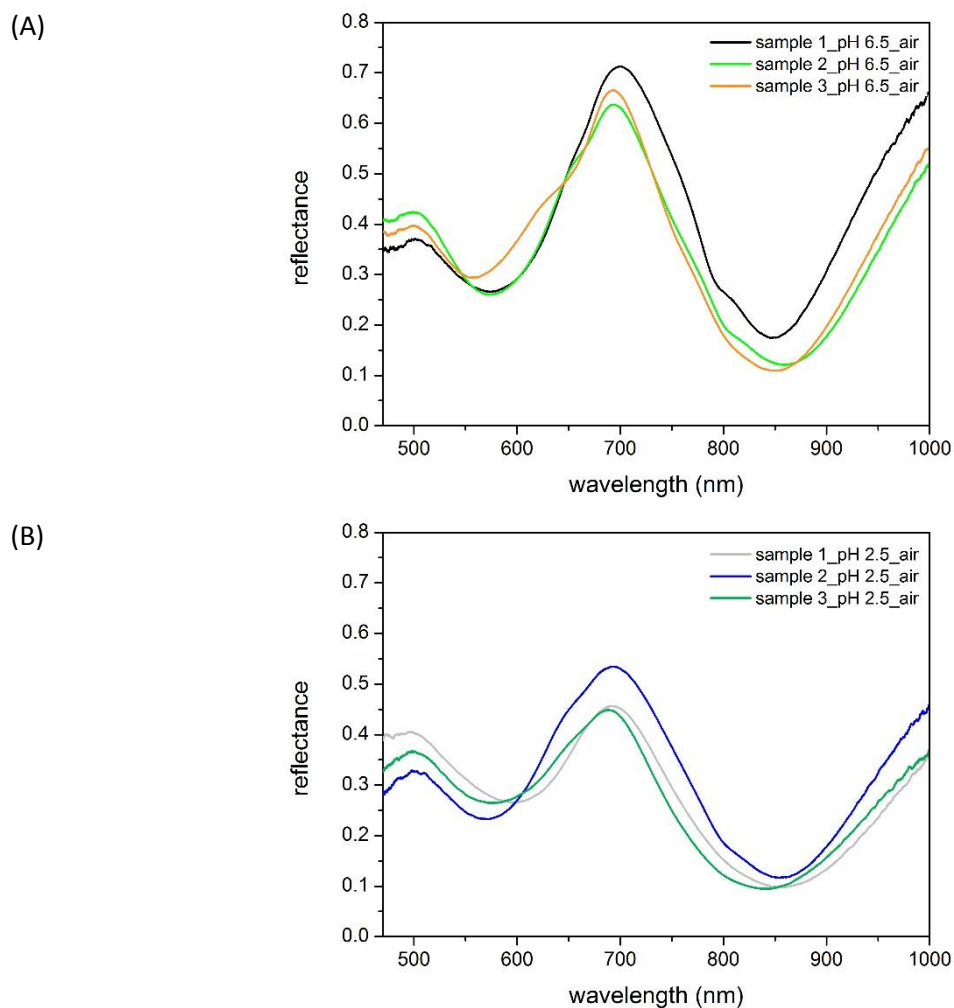


Figure 4. 3 – Reproducibility study through the reflectance spectra of samples (3x) related to colloidal monolayers (500 nm pitch) obtained with different pH of the LB subphase. (A) pH 6.5; (B) pH 2.5.

Figure 4.4 shows the bulk sensitivity to different refractive index changes: Figures 4.4 (A-B) report the reflectance variation when the medium changes from air to Milli-Q water, while Figures 4.4 (C-D) refer to smaller refractive index variation when the medium changes from Milli-Q water to the fixed solution.

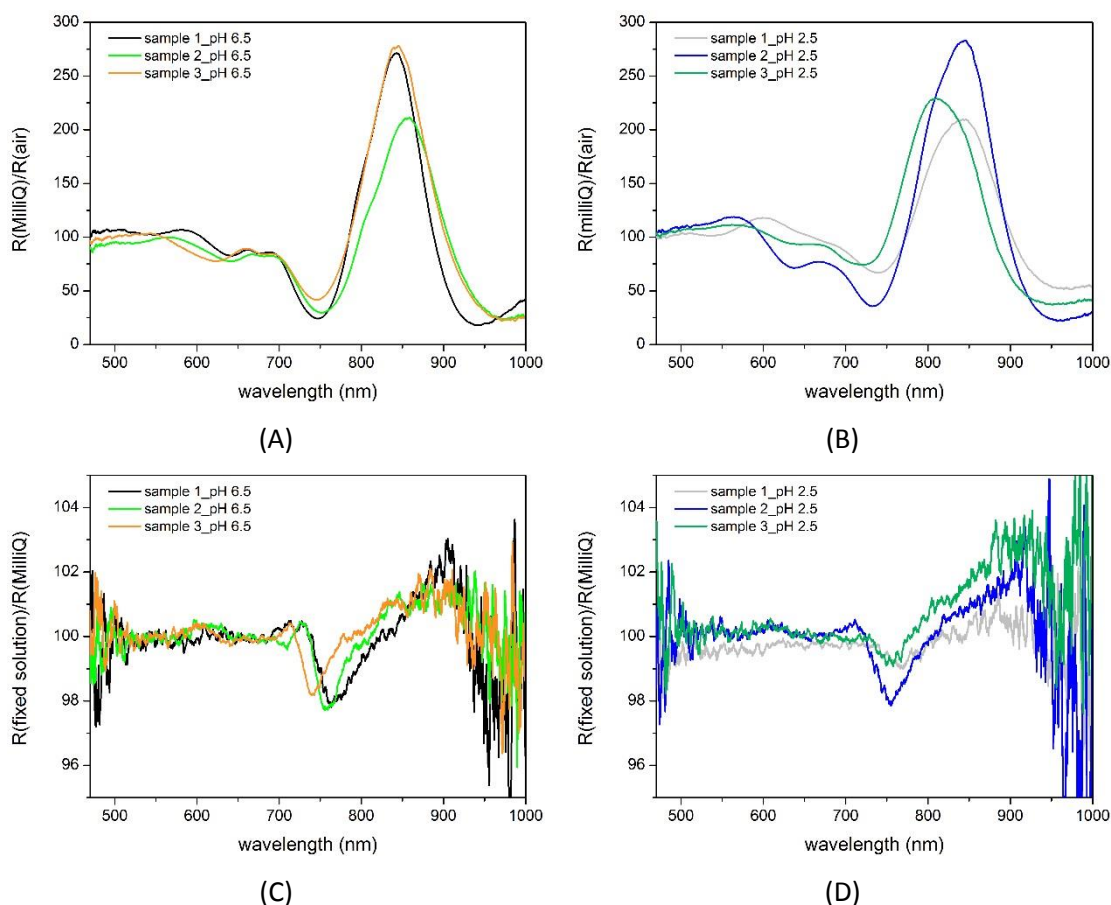


Figure 4. 4 – Reproducibility study through the ratio of the reflectance spectra related to different refractive index changes and pH conditions in 3 samples (500 nm pitch). (A) Milli-Q/air, pH 6.5; (B) Milli-Q/air, pH 2.5; (C) fixed solution/Milli-Q, pH 6.5; (D) fixed solution/Milli-Q, pH 2.5.

The results of the bulk sensitivity in combination with the improved stability of the ppAA layer make the selection of standard LB subphase (pH=6.5) more appropriate for the fabrication of plasmonic surfaces.

4.2 INFLUENCE OF THE ETCHING PROCESS

4.2.1 POLYMER PILLARS

Several batches of samples were produced by nanostructuring a layer of ppAA (150 nm in thickness) with a colloidal mask of PS 500 nm beads. First of all, the effect of different O₂ etching time (3', 4', 5', 6') was tested and the reduction of the particle diameter was measured (Figure 4.5). After 3' and 4' of etching the diameter reduces to 350 and 255 nm, respectively. For longer etching time the etching rate is lower and results in 230 and 218 nm when 5' and 6' are applied.

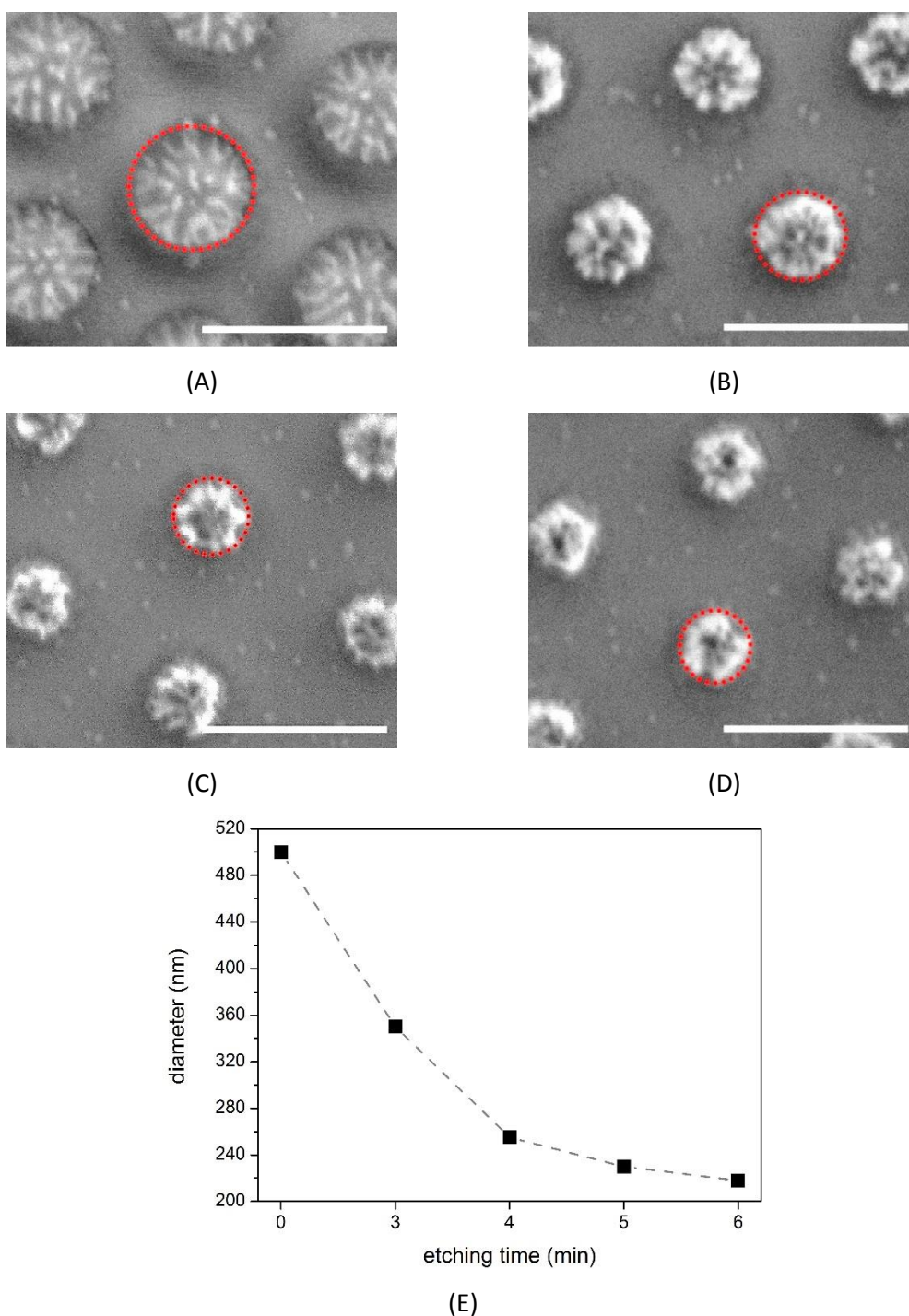


Figure 4. 5 – PS 500 nm beads after 3' (A), 4' (B), 5' (C), 6' (D) of O_2 plasma etching and related plot of diameter reduction as a function of the etching time (E).

SEM and AFM images in Figure 4.6 show the top and tilted view and the related profile of ppAA pillars obtained with 4', 5' and 6' of etching. In particular, in order to consider a more realistic shape of the pillar edges, the SEM images in tilted view are useful to complement the AFM profile, where the effect of the AFM tip has to be considered. The sample made with lowest etching time has a quite cylindrical base with a small rounded tip on top. At intermediate etching time, the pillar shape is quite similar to the previous one but slightly more conical with less steep

edges. At the highest etching time, the pillars are characterized by a more truncated cone shape with a flat top, likely due to the effect of an over-etching.

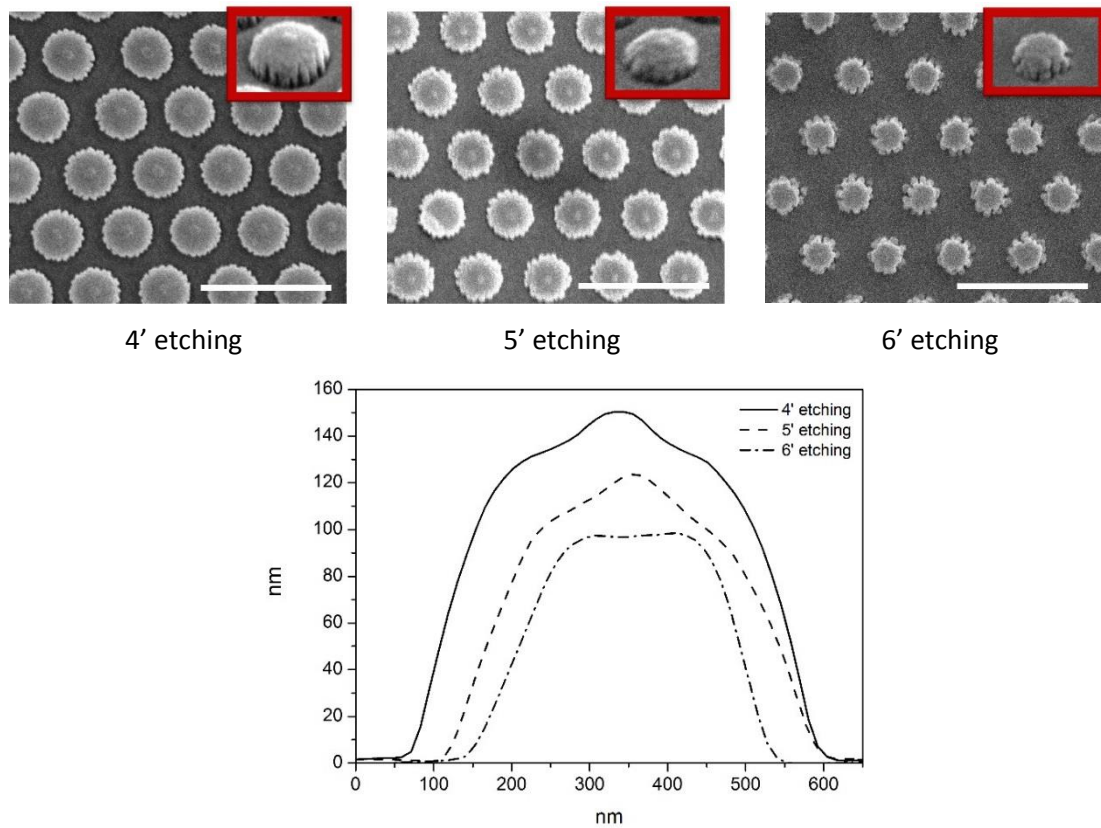


Figure 4. 6 – SEM images of top and tilted view of ppAA pillars after 4', 5' and 6' of O₂ plasma etching (top) and related profiles measured by AFM (bottom). The scale bar corresponds to 1 μm , while, the width of the inset in tilted view in the SEM images corresponds to 560 nm.

Once the etching step was calibrated, the fabrication process was completed with the deposition of a gold layer and the final lift off of the particle residuals. Figure 4.7.A reports the reflectance spectra in air and the relative spectra in Milli-Q water of ppAA nanostructures made with 4', 5' and 6' of etching. The optical behaviour of the plasmonic surface is strictly related to the pillar shape [142, 143]. Indeed, as the etching time increases and the pillar changes from tapered to truncated cone, the position of the localized mode moves from 980 to 880 nm. On the opposite, the delocalized mode related to the gold glass SPP, which mainly depends on the grating period, does not significantly shift, but keeps its position around 700 nm. The ratio of the reflectance spectra in Milli-Q to reflectance spectra in air shows that all the surfaces are sensitive to refractive index changes, with better performances when an intermediate etching time is considered (Figure 4.7.B).

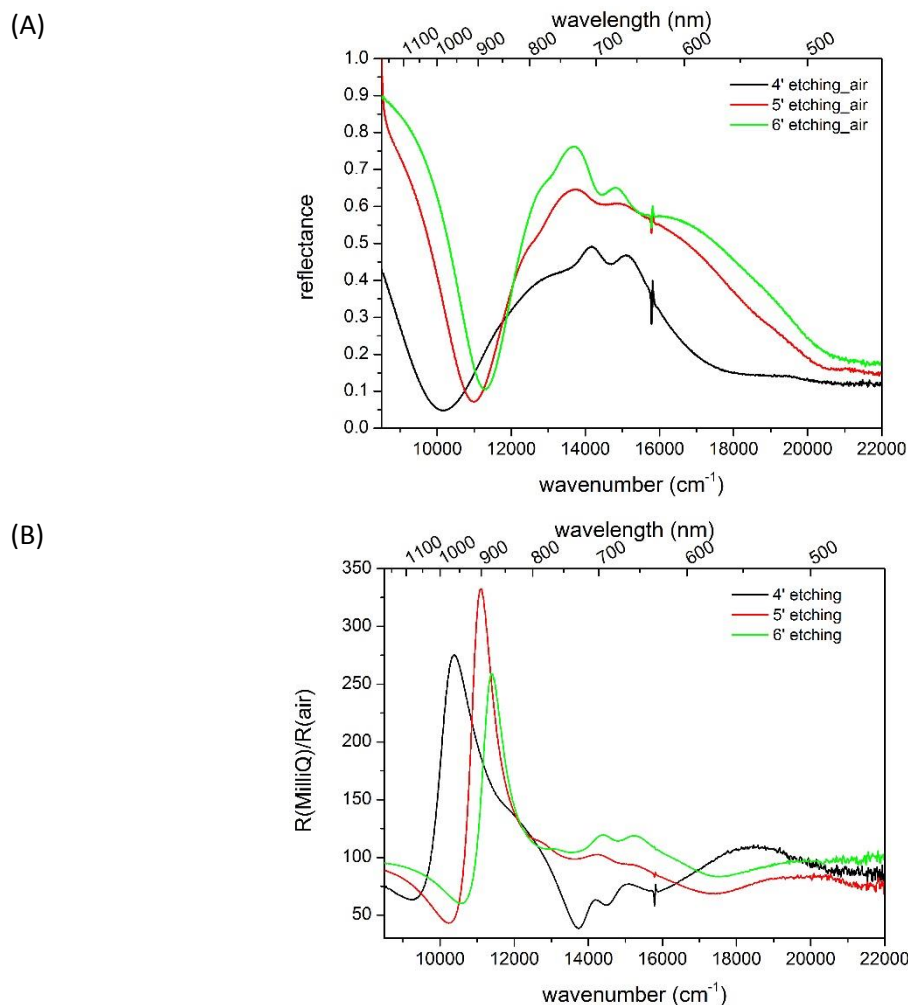


Figure 4. 7 - Spectra in air of samples (500 nm pitch) made with 4', 5' and 6' of O₂ plasma etching (A) and ratio of the reflectance spectra in Milli-Q to reflectance spectra in air (B).

SEM images support the explanation of the reflectance measurements: in Figure 4.8 it is possible to observe the plasmonic surface obtained with 5' (left) and 6' (right) of etching.

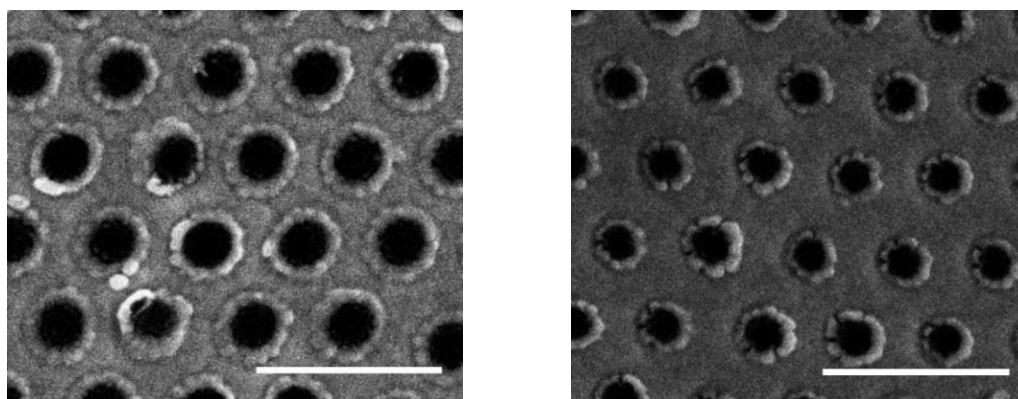


Figure 4. 8 – SEM images of plasmonic surfaces related to ppAA nanostructures (500 nm pitch) obtained with 5' (left) and 6' (right) of O₂ plasma etching. Scale bar: 1µm.

The pitch is the same for the two images and the gold deposition has the effect of reducing the aperture at the top of the pillar and leading to a gold corona around it, especially in case of

tapered pillars. The thin gold layer at the top of the pillar acts as a plasmonic nano-antenna which forces the resonance of the electromagnetic field and results in the electric field localization and enhancement [143].

4.2.2 SiO₂ PARTICLES AND SILICON PILLARS

As an alternative to etching masks made of polystyrene beads, colloidal monolayers of SiO₂ particles were considered. These monolayers were transferred on silicon substrates, according to the procedure described in Chapter 3. Indeed, the higher resistance of these sacrificial masks to etching processes allows nanostructuring harder substrates and offers the possibility to play with etching parameters and obtain tuned pillar shapes with different optical behaviour.

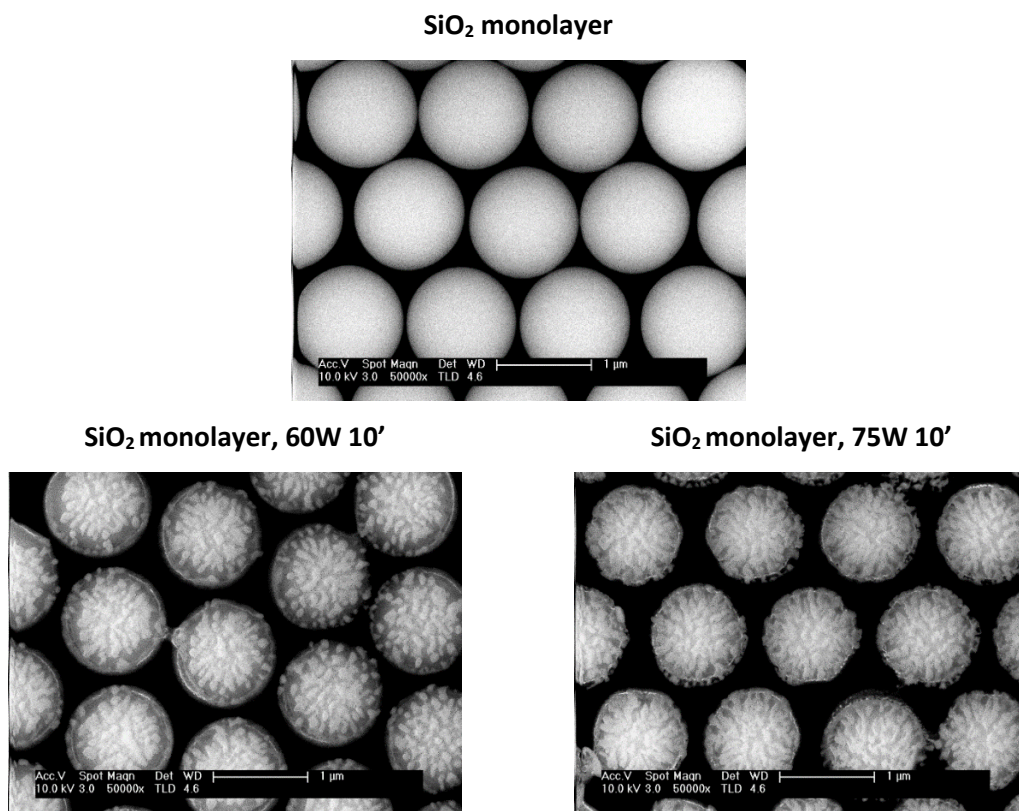


Figure 4.9 – SiO₂ 1000 nm bead monolayers before (top) and after two different etching processes of 10' at 60 W and 75 W (bottom left and right, respectively).

Figure 4.9 shows two SiO₂ colloidal monolayers on Si wafer (nominal particle diameter= 1000 nm) after the LB transfer (top) and after the conditioning with CF₄/Ar plasma etching (bottom). The etching parameters were selected in order to obtain a proper nanostructure within the substrate without an excessive damage of the particle mask, which could negatively affect the final lift off step. In particular, the process power was set to 60 W (Figure 4.9, bottom left) and 75 W (Figure 4.9, bottom right) and, in both cases, the gas mixture was 25 sccm CF₄/ 5 sccm Ar, the pressure 25 mTorr and the etching time was set to 10'. From the analysis of SEM images, it

is possible to notice a diameter of circa 1130 nm for the bare SiO₂ particles and a reduction to 1070 nm and 1020 nm when a plasma power of 60 W and 75 W is applied, respectively.

As a final step a gold layer was deposited by means of a sputtering process with a nominal thickness of approximately 310 nm. After the lift-off of the particle residuals, the surfaces were characterized by angle resolved reflectance measurements with light impinging from the surface side. SEM images in Figure 4.10 (A-D) show well-ordered patterns with different aspect ratio of Si pillars obtained with different etching power.

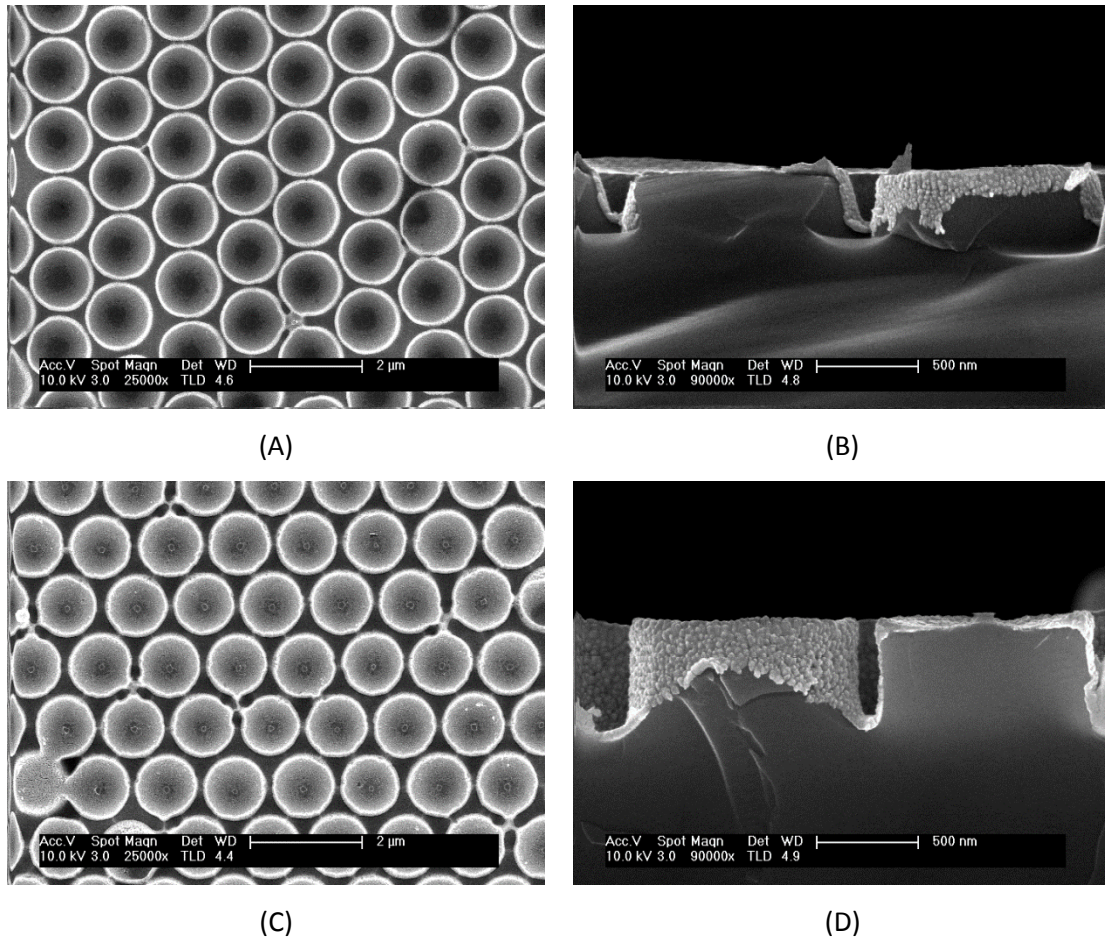


Figure 4. 10 – Top view and cross section of gold/Si pillar structures made at 60 W (A-B) and 75 W (C-D).

When a power of 60 W is applied (Figure 4.10 A-B), the pillar shape is more similar to a truncated cone with a height of 290 nm and top and bottom diameter of 990 and 1120 nm, respectively. On the other hand, when a power of 75 W is applied (Figure 4.10 C-D), the pillar shape is more cylindrical with a height of 480 nm and a diameter of 1000 nm. Since the deposition of the gold is limited by the presence of particle residuals during the sputtering, it results in a thin layer of circa 50 nm around the pillars. A very thin layer of gold is also present on top of the pillar when stronger etching conditions are applied.

Figure 4.11 reports reflectance spectra and the related intensity map of reflectance for the samples prepared by means of the two conditions (A, B: 60 W; C, D: 75 W) and measured by

varying the incidence angle from 5° to 60° . In particular, the reflectance map offers a better visualization of the dispersion modes of the reflectance features.

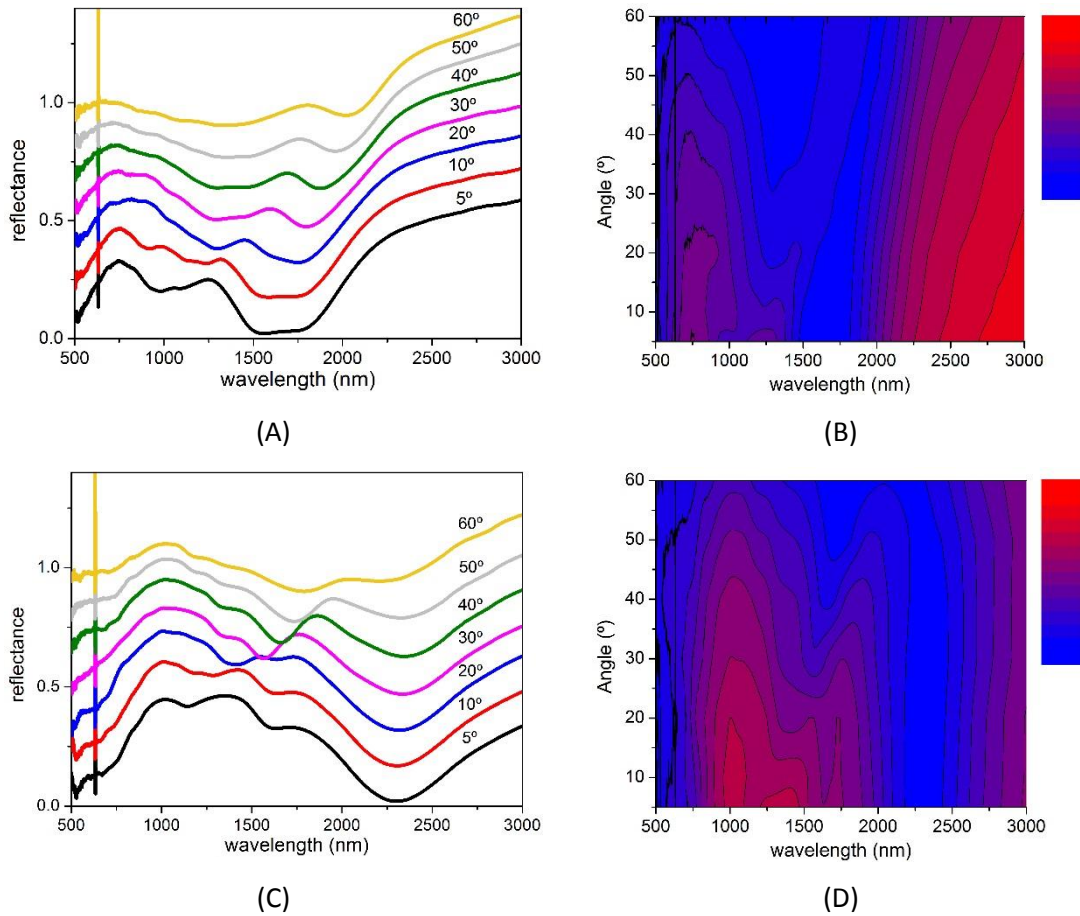


Figure 4. 11 - Reflectance spectra and related intensity map of reflectance of the gold/Si pillar samples prepared with two etching power conditions (A, B: 60 W; C, D: 75 W) and measured by varying the incidence angle from 5° to 60° . The curve at 5° is the real measured spectrum, the other curves are vertically stack for a better comparison. The scale of the maps is red for higher reflectance and blue for lower reflectance.

For the sample made at 60 W, three main reflectance minima are observed. The lower energy valley becomes narrower and shifts from 1640 to 2000 nm when the angle of incidence varies from 5° to 60° ; the intermediate minimum moves from 1100 to 1340 nm and the higher energy valley from 970 to 1080 nm. Moreover, these last two peaks become broader and less pronounced. For the sample made at 75 W, three main reflectance minima are again observed, but they are all shifted towards lower energies with respect to the previous ones and show higher values of relative reflectance according to a more effective presence of gold. The lower energy minimum shifts from 2340 to 2250 nm when the angle of incidence varies from 5° to 60° ; the intermediate minimum becomes more pronounced and moves from 1630 to 1560 nm when the angle of incidence varies from 5° to 30° and then shifts back to 1780 nm for higher incidence angle. The higher energy dip, instead, becomes less pronounced and moves from 1140 to 1360

nm when the angle of incidence varies from 5° to 60° . In addition, for angles higher than 50° a new weak spectral feature appears around 1170 nm. All these features can be likely correlated with the dispersion behaviour of surface polaritons at the gold interface and their interplay with the localized plasmon resonances.

4.3 THE EFFECT OF POLYMER AND GOLD LAYERS

4.3.1 INFLUENCE OF POLYMER THICKNESS

The influence of the polymer thickness was tested by using the standard fabrication protocol, but varying the deposition time of the ppAA layer. The gold layer was deposited at the same nominal thickness of the polymer. In particular, thicknesses of 150 and 200 nm were selected, since a gap of 50 nm should be enough to avoid the spectroscopic data to be affected by the deposition non-uniformity of the ppAA layer, which could be in the order of 5-10 nm.

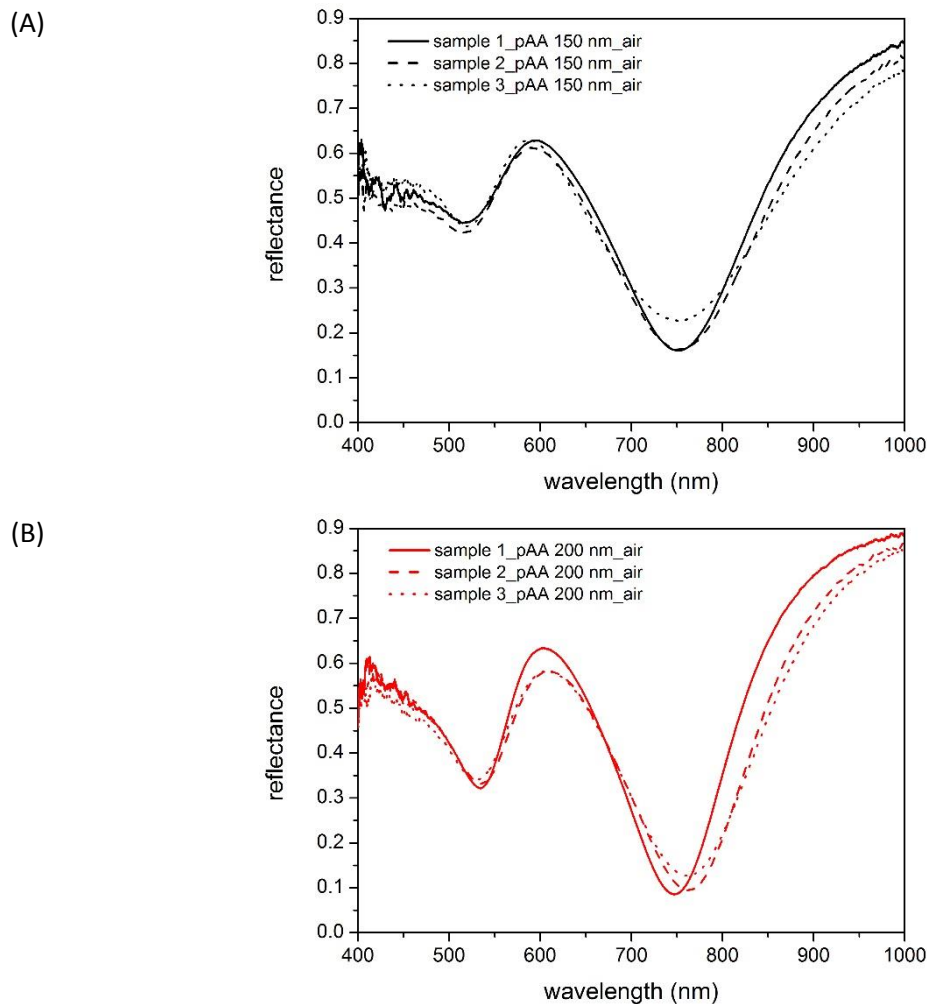


Figure 4. 12 – Polymer thickness reproducibility study through the reflectance spectra in air of nanocavity samples (3x) fabricated with 400 nm pitch and obtained with two different ppAA thicknesses: (A) 150 nm and (B) 200 nm.

All the samples were transferred with a colloidal mask of 400 nm PS beads. For each batch, three samples have been considered to show the reproducibility of the optical response (Figure 4.12). In both cases, the main minimum is centred at around 750 nm with good reproducibility, slightly better in case of 150 nm ppAA (Figure 4.12 A). Nevertheless, the peaks are better defined when a thickness of 200 nm is considered (Figure 4.12 B).

This behaviour results in a better sensitivity to small refractive index changes for samples made with 200 nm ppAA when spectra in fixed solution and Milli-Q are considered (Figure 4.13.A-B). In fact, the combination of higher polymer thickness and constant etching time leads to tapered pillars and consequently more sensitive surfaces, according to results exposed in section 4.2.1.

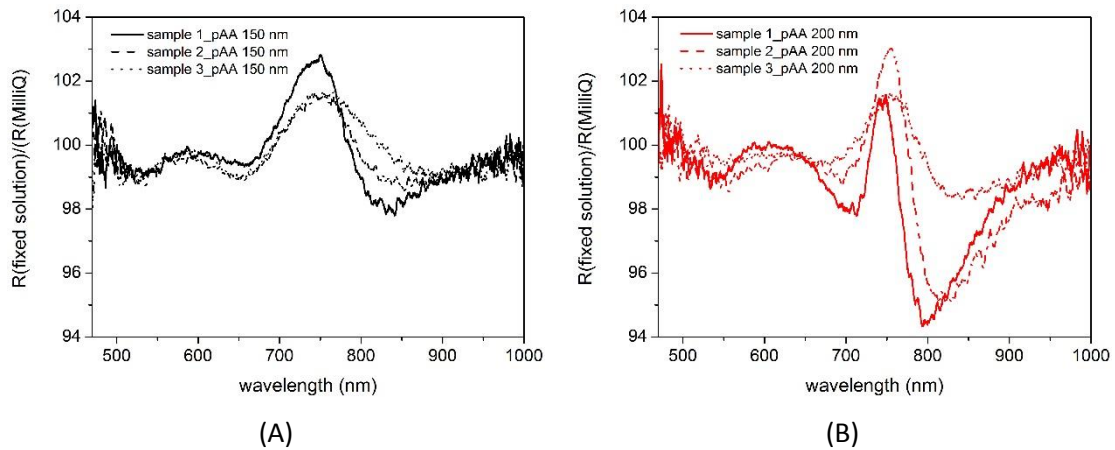


Figure 4. 13 - Ratio of the reflectance spectra in fixed solution to reflectance spectra in Milli-Q, related to different ppAA thickness in 3 samples (400 nm pitch). (A) ppAA 150 nm; (B) ppAA 200 nm.

4.3.2 COMPARISON OF DIFFERENT POLYMER SUBSTRATES

The choice of a proper polymeric layer affects the final surface, because a different resistance to the etching process will lead to different pillar shapes and different sensitivity of the final surface. In this investigation, ppAA and PMMA were compared as deposited by PE-CVD and spin coating, respectively. The deposition by spin coating offers the possibility to productively coat big areas with good control over the thickness uniformity, which can be a useful advantage when the industrial scalability of the process is considered. On the other hand, PE-CVD allows a uniform deposition, but the area is limited by the dimension of the reactor chamber. The lack of an online control could additionally affect the batch to batch reproducibility. Both polymeric layers were characterized by ellipsometry in order to get information such as thickness, uniformity and optical constants. A Cauchy model was adopted to analyse the experimental data from the polymeric layer, according to Equations 2.14-2.15 introduced in Chapter 2. We fixed the extinction coefficient amplitude α to 0, the exponent factor β to 1.5 and the band edge γ to 4000 μm . For the ppAA layer, fitting results provided the following thickness (d) and Cauchy dispersion parameters: $d = 159.92 \text{ nm} \pm 3.74\%$ non-uniformity, $A = 1.54$, $B = 0.00957$, $C = 0$; while

for the PMMA layer the values were: $d = 160.45 \text{ nm} \pm 4.63\%$ non-uniformity, $A = 1.48$, $B = 0.00408$, $C = 0$. The behaviour of the optical parameters n and k of the two layers are reported in Figure 4.14.

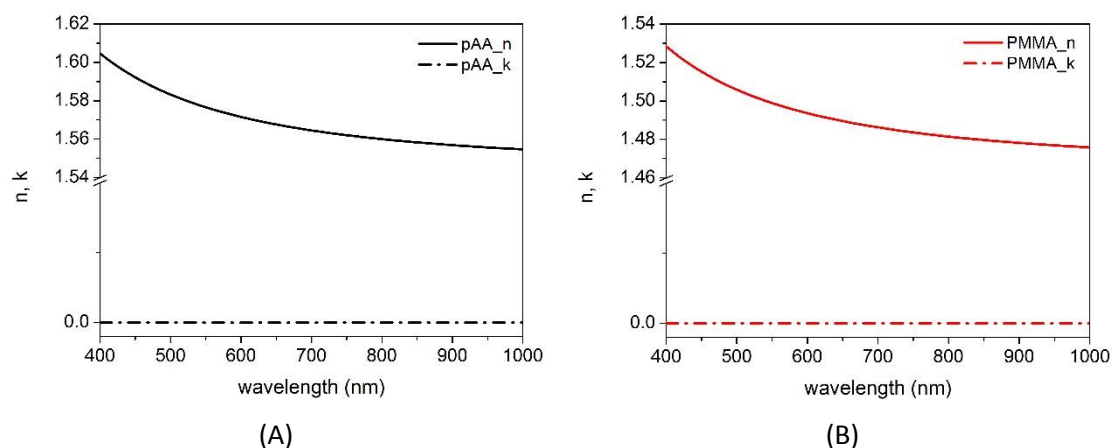


Figure 4. 14 – Optical parameters (n , k) extrapolated from the Cauchy fit for the ppAA (A) and PMMA (B) layers.

The sensitivity to the etching process is slightly different for ppAA and PMMA. The pillars were obtained by depositing 150 nm of polymer, a colloidal mask of 500 nm PS beads and an O_2 plasma etching of 4'. If the particles are lifted off just after the etching step (Figure 4.15), the ppAA pillars (Figure 4.15 A) appear a bit larger than the PMMA ones (Figure 4.15 B) and less damaged due to a higher resistance to O_2 etching, which also influences the adhesion of the colloidal mask.

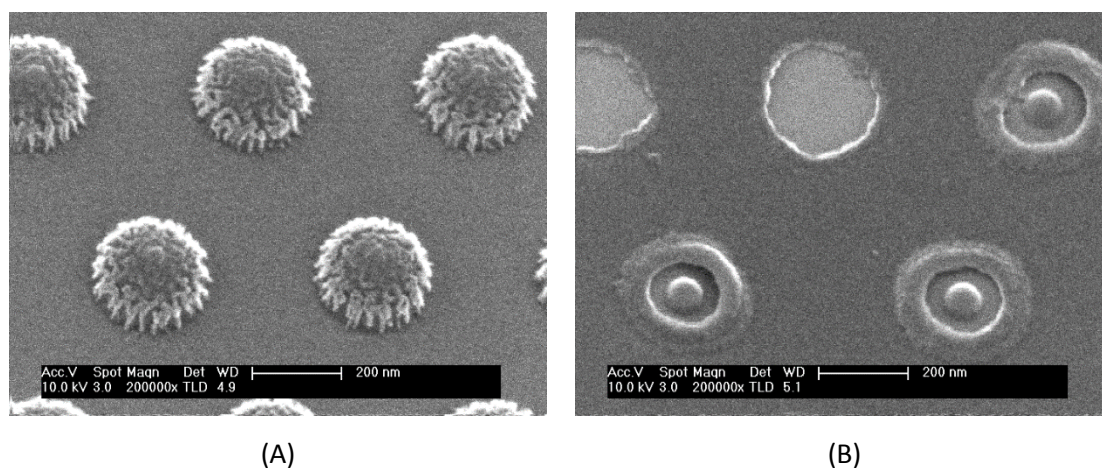


Figure 4. 15 – Pillars made of ppAA (A) and PMMA (B) after 4' of etching (colloidal mask: PS particles, $\phi = 500 \text{ nm}$).

Consequently, the deposition of the same nominal thickness of gold leads to cavities with a different superficial feature for each polymer. Figure 4.16 shows a gold corona over the edge of the bulk gold layer in case of ppAA pillars and a corona under that edge in case of PMMA pillars (Figure 4.16 A and B, respectively). An annealing treatment at 300°C after the lift of the particles

makes the bulk gold more compact and positively affects the features of the gold corona, leading to a more open cavity (Figure 4.16 C and D for ppAA and PMMA, respectively).

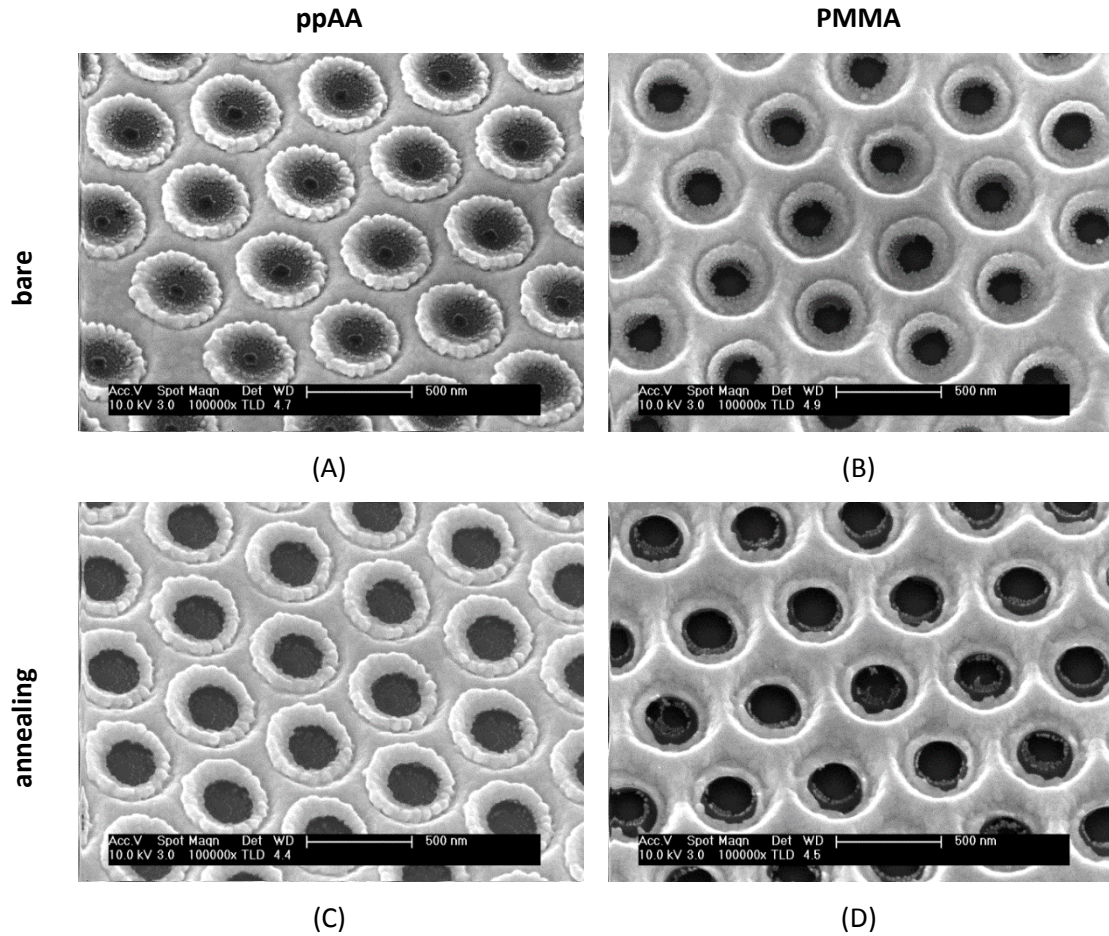
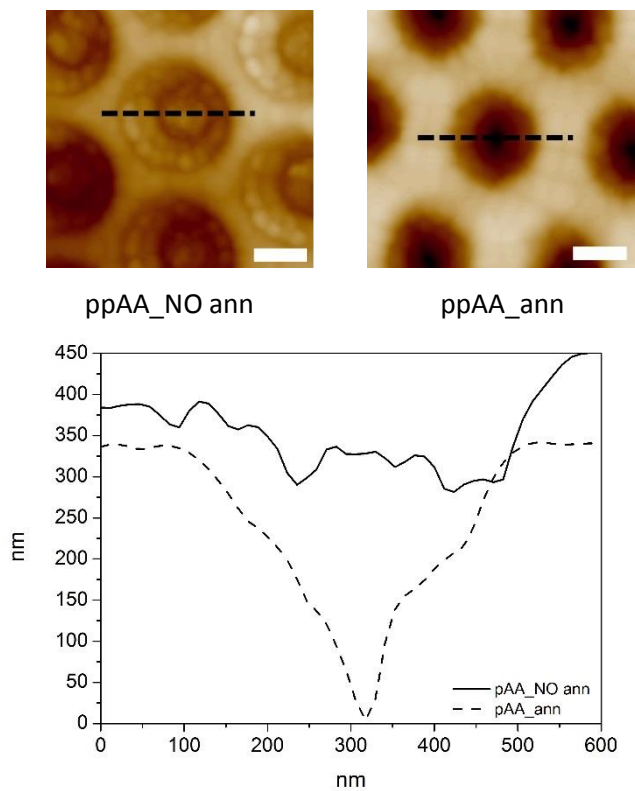
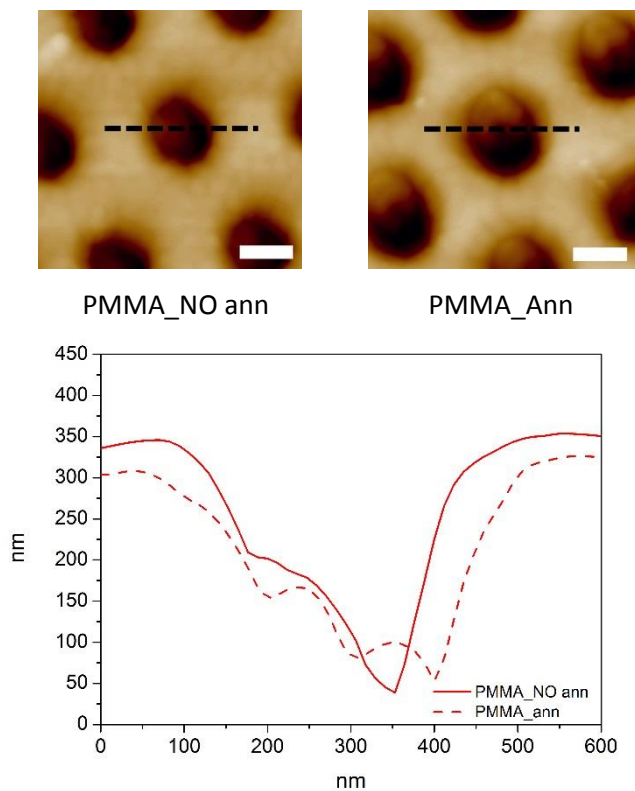


Figure 4. 16 – Plasmonic surface made of gold/ppAA and gold/PMMA (500 nm pitch) before (A, B) and after (C, D) thermal annealing of the gold layer.

AFM images in Figure 4.17 show a better detail of the cavity profile. In case of gold/ppAA structures, the polymer pillar inside the cavity is at a comparable height to the gold layer in spite of the pronounced gold corona at the edge, but after the annealing treatment the pillar is modified and the cavity is partially empty with an internal V-shaped valley, as deduced from the plot of the cavity profile (Figure 4.17.A). Bare gold/PMMA structures present a corona at the edge of the gold film. After the annealing, the gold corona is slightly modified but it is not possible to appreciate a remarkable difference of the pillar height inside the cavity (Figure 4.17.B).



(A)



(B)

Figure 4. 17 – AFM images and profiles of gold cavities (500 nm pitch) made with (A) ppAA and (B) PMMA structures (ann: thermal annealing). The white scale bar corresponds to 200 nm.

The optical behaviour in air of samples made with gold/ppAA and gold/PMMA (Figure 4.18. A and B, respectively) are quite different since the former surface has lower reflectance and less pronounced peaks. The spectra become comparable, especially around the main minimum observed at around 850 nm when the annealing is considered.

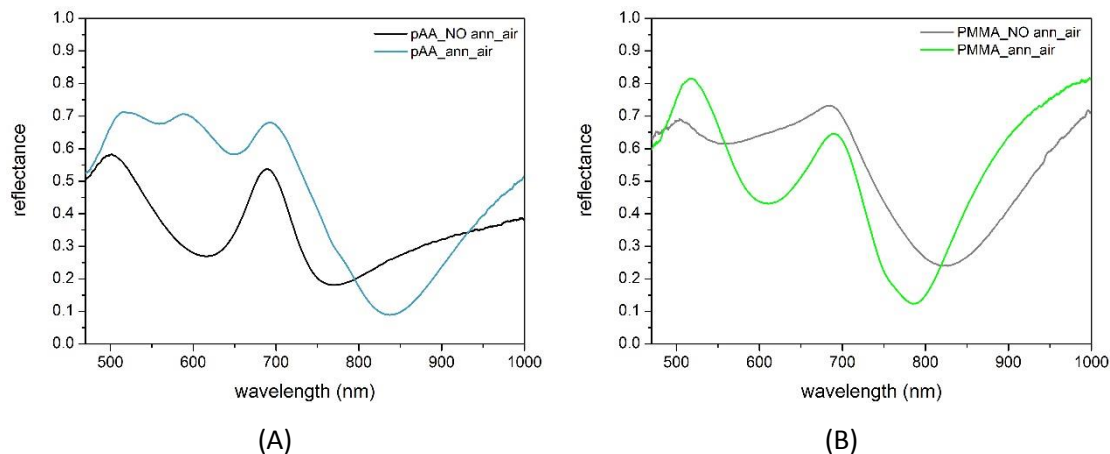


Figure 4. 18 – Reflectance spectra in air of samples obtained with gold/ppAA (A) and gold/PMMA (B) structures (500 nm pitch), without and with thermal annealing (ann: thermal annealing).

In both cases, it is possible to obtain surfaces sensitive to small refractive index changes (Figure 4.19), with higher improvement after annealing treatment, especially in the case of gold/PMMA structures, as derived from the increase of the derivative of the spectra at the low energy side of the 850 nm minimum.

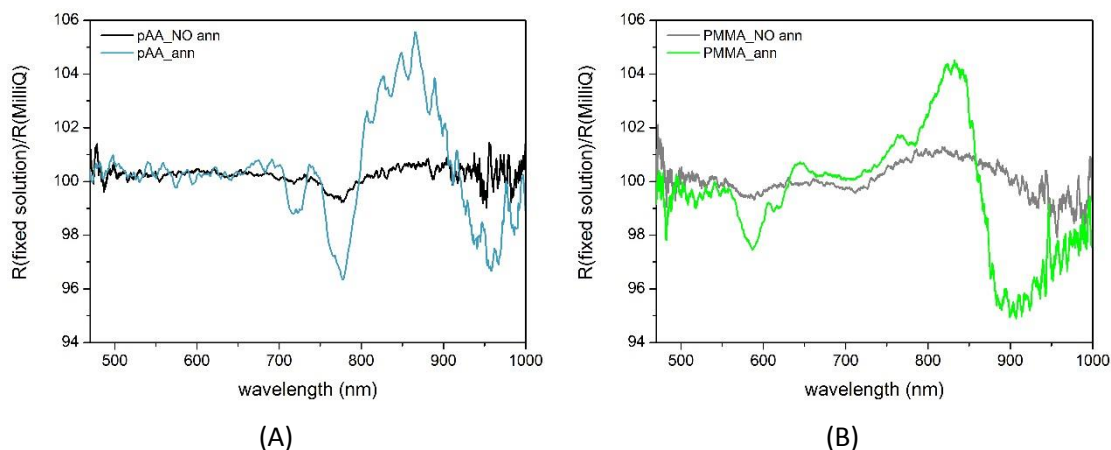


Figure 4. 19 - Ratio of the reflectance spectra in fixed solution to reflectance spectra in Milli-Q of samples obtained with gold/ppAA (A) and gold/PMMA (B) structures (500 nm pitch), without and with thermal annealing (ann: thermal annealing).

The annealing treatment also affects the hydrophilicity of the surface. Measurements of water contact angle (WCA) reported in Table 4.1 show a value of $76 \pm 3.5^\circ$ and $84 \pm 1.2^\circ$ for the bare gold/ppAA and gold/PMMA structures, respectively. After annealing, both surfaces become more hydrophobic with a contact angle of $93 \pm 2^\circ$ and $93 \pm 4.2^\circ$, respectively. It is relevant that in spite of the differences in surface chemistry (ppAA vs PMMA) and topography (i.e. internal

cavity roughness), the WCAs are very similar for both structures, especially after annealing. In view of these results, we studied the potential optimization of the optical signal with further post-treatments, which are described in the following section.

Table 4. 1 – Contact angles of samples made with gold/ppAA and gold/PMMA structures (500 nm pitch), before and after thermal annealing (ann: thermal annealing).

Sample	Contact angle
ppAA_NO ann	$76 \pm 3.5^\circ$
ppAA_ann	$93 \pm 2^\circ$
PMMA_NO ann	$84 \pm 1.2^\circ$
PMMA_ann	$93 \pm 4.2^\circ$

4.3.3 INVESTIGATION OF SURFACE POST-TREATMENTS

As introduced in the previous sections, a surface treatment sequential to the particle lift off can be considered to further improve the optical response of the Au cavity structures. In view of the aforementioned easier fabrication and sensitivity of the PMMA motives, only the results related to gold/PMMA structures are reported herein, but analogous preliminary results were obtained with gold/ppAA structures. The samples were fabricated with 150 nm PMMA layer, PS 500 nm colloidal mask, 4' O₂ plasma etching and 150 nm of gold. Then, two different batches were taken into account, each one made of three samples, as resumed in Table 4.2.

Table 4. 2 – Sample overview of gold/PMMA structures (500 nm pitch) made with different surface post-treatments (ann: thermal annealing, KI: wet gold etching, pe: O₂ plasma post-etching).

	Sample	Surface treatment		
		Annealing	Wet etching	O₂ post-etching
Batch 1	PMMA_NO ann			
	PMMA_NO ann_KI		✓	
	PMMA_NO ann_KI_pe		✓	✓
Batch 2	PMMA_ann	✓		
	PMMA_ann_KI	✓	✓	
	PMMA_ann_KI_pe	✓	✓	✓

An annealing treatment was evaluated to give more stability to the Au layer and to contribute to a better definition of the surface motives around the cavity top. A gentle and controlled wet gold etching was studied to clean the surfaces from possible contaminations by eliminating the more superficial gold layer. Finally, an O₂ plasma post-etching was introduced for a better cleaning of the surface and to adjust the height of the pillar inside the cavity and the wettability

of the surface. The different surface post-treatments were investigated as single process or as a combination of different steps.

We started by studying with more detail the effects of the annealing treatment at 300°C. SEM images in Figure 4.20 show a plasmonic surface without and with annealing (Figure 4.20 A and B, respectively). In both cases, the samples are made of a well-ordered array of cavities as visible from the top view images in the insets. The tilted view images at higher magnification offer a better detail of the cavity features. The bare surface without annealing presents a pronounced cavity with a thin layer of gold on top made of small particles. The annealing treatment favours a de-wetting of these particles and results in a decreased number of bigger particles (circa 25 nm in diameter). Bulk gold also appears smoother and made of larger and more compact grains.

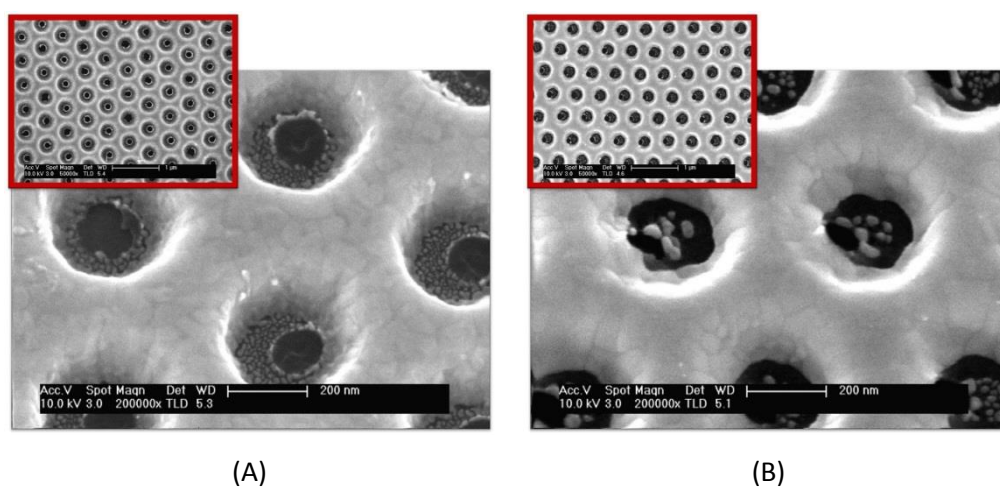


Figure 4. 20 - Plasmonic surfaces made of gold/PMMA structures (500 nm pitch), without (A) and with (B) thermal annealing.

XPS measurements, performed on nanostructured gold/PMMA substrates without and with thermal annealing (Figure 4.21 A and B, respectively), show a different deconvolution of the core level spectra of the C1s peak. Indeed, in case of samples made without annealing, the C1s peak presents four components: the main contribution relates to the C-C binding around 285.0 eV, while the other ones to the C-OR, C=O and O=C-OR groups around 286 eV, 289 eV and 291.50 eV, respectively. In case of thermal annealing, the component at higher binding energy related to the O=C-OR groups disappears, while the component C-OR becomes more significant. The O=C-OR binding mainly relates to the O=C-OCH₃ typical of the PMMA layer and its modification indicates that the thermal annealing not only affects the gold layer but also the polymeric layer.

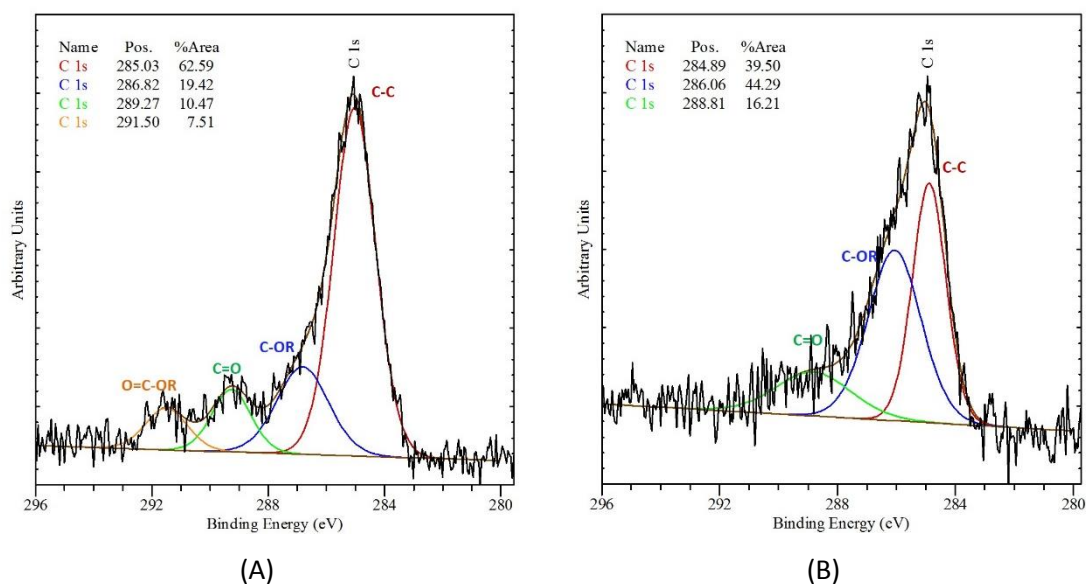


Figure 4. 21 - XPS C 1s core level spectra of nanostructured gold/PMMA samples (500 nm pitch) made without (A) and with (B) thermal annealing.

The Au cavity surfaces were further conditioned by trying to homogenize their structure by using wet etching. This treatment is done by using a commercial product (Gold etchant, Sigma Aldrich) based on a KI solution in water. A dilution of 1:640 from the stock solution was chosen in order to clean the superficial layer of gold and gently affect the thinner layer of Au around the top of the cavity. This leads to a wider cavity aperture and more defined gold grains, as shown in Figure 4.22 for a bare sample before (Figure 4.22 A) and after wet etching (Figure 4.22 B). As a drawback, the KI solution can partially infiltrate the Au layer even after deep washing in water, making the surface less resistant to ageing.

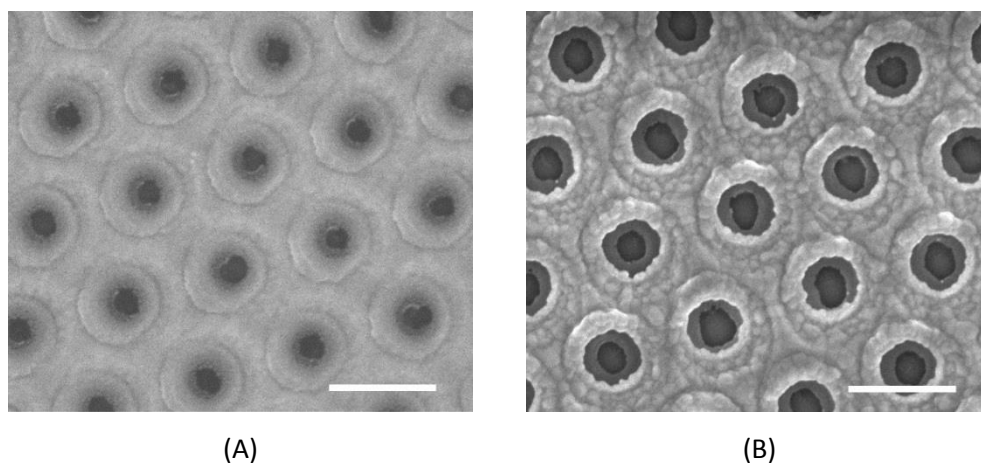


Figure 4. 22 - Plasmonic surfaces made of gold/PMMA structures (500 nm pitch), without (A) and with (B) wet etching.

Finally, an O₂ plasma post-etching of the whole structure was also considered to influence the optical response of the Au cavity surfaces. The AFM profile of the surface after post-etching shows a more open cavity and a lower height of the pillar inside the cavity (Figure 4.23).

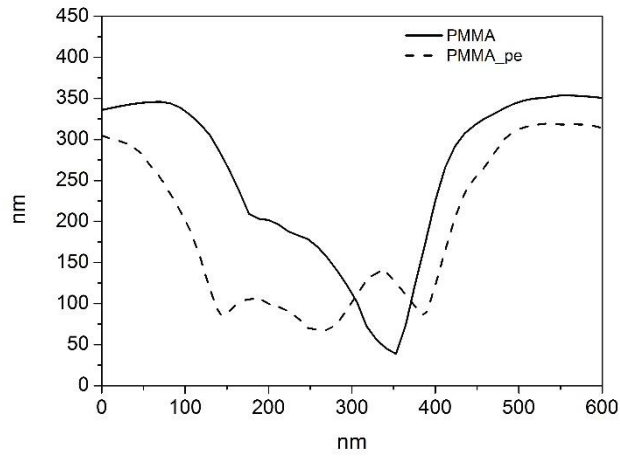


Figure 4. 23 - AFM profile of bare gold/PMMA structures (500 nm pitch) before (solid line) and after (dashed line) O_2 plasma etching (pe: O_2 plasma post-etching).

Figures 4.24-4.25 show the reflectance spectra of the two series of samples with gradual post-processing steps as analysed in air and in the fixed solution.

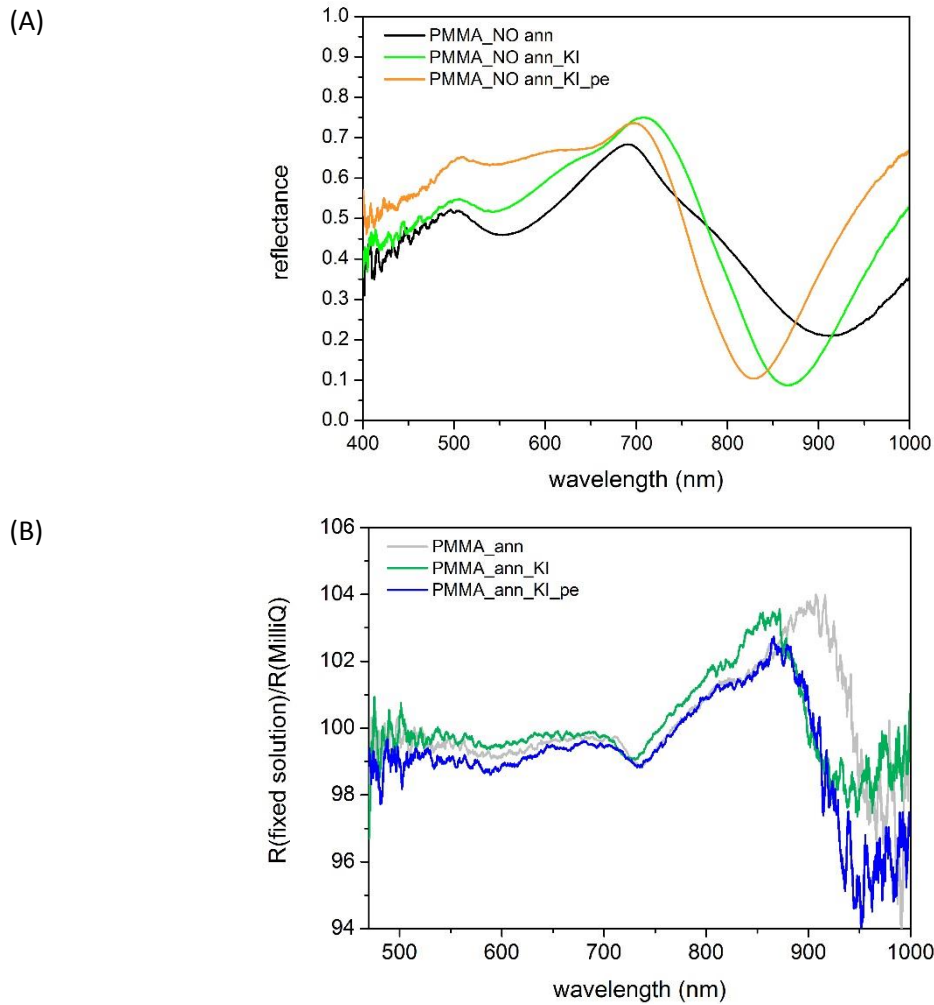


Figure 4. 24 - Reflectance spectra in air of samples obtained with gold/PMMA structures (500 nm pitch), without (A) and with (B) gold annealing and sequential surface post-treatments (ann: thermal annealing, KI: wet gold etching, pe: O_2 plasma post-etching).

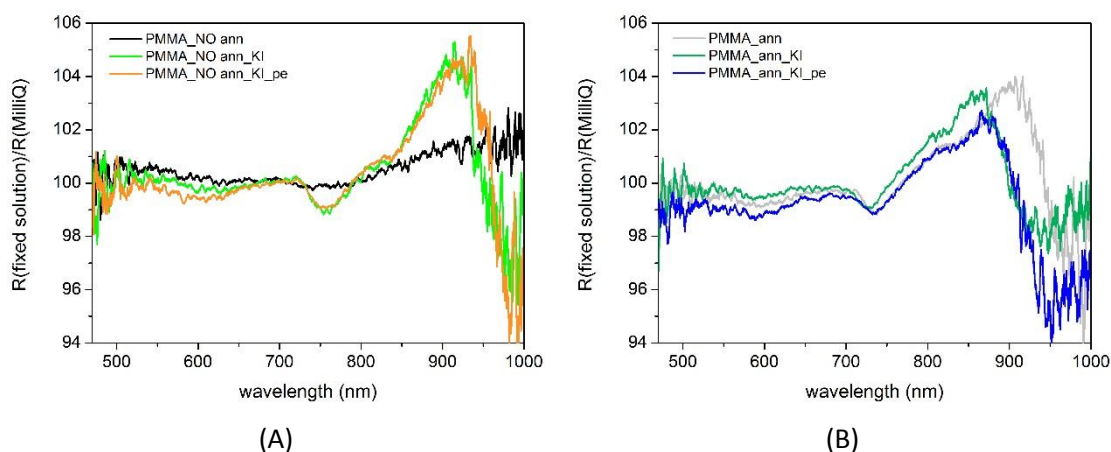


Figure 4. 25 - Ratio of the reflectance spectra in fixed solution to reflectance spectra in Milli-Q of gold/PMMA structures (500 nm pitch) after different surface post-treatments, without (A) and with (B) thermal annealing (ann: thermal annealing, KI: wet gold etching, pe: O₂ plasma post-etching).

Spectra in air of samples made without thermal annealing (Figure 4.24 A) present a deep minimum, which becomes more pronounced and moves towards lower wavelength when a new surface treatment is added. Indeed, the bare surface after particle lift off has a minimum around 920 nm, which shifts to 860 and 830 nm when wet etching and O₂ post-etching are, respectively, performed. This variation of the localized plasmonic mode is strictly related to a strong modification inside the polymeric cavity and has a positive effect on the improvement of the surface sensitivity. After etching post treatments, the surface shows higher sensitivity to small refractive index changes when the fixed solution is tested (Figure 4.25). The thermal annealing has also the effect to move the minimum towards lower wavelength (around 850 nm), as noticed in the corresponding spectra of Figure 4.24 B. If other treatments are added after surface annealing, the spectra in air appear quite stable with only a slight shift towards lower wavelength in the order of 10-15 nm. The surface is already sensitive after the annealing and the optical behaviour in response to small refractive index changes is comparable to what observed by adding the additional etching.

The measurement of the contact angle gives an indication of the effect of the post treatments on the surface wettability. The ageing of the samples was also investigated in order to evaluate the effect on the modification of the WCA. In particular, this study was done on nanostructured samples made without thermal annealing, but post-treated with a combination of wet and plasma etching and monitoring the recovery of the WCA. Figure 4. 26 shows the evolution of the contact angle over one week of ageing for three samples processed under the same conditions.

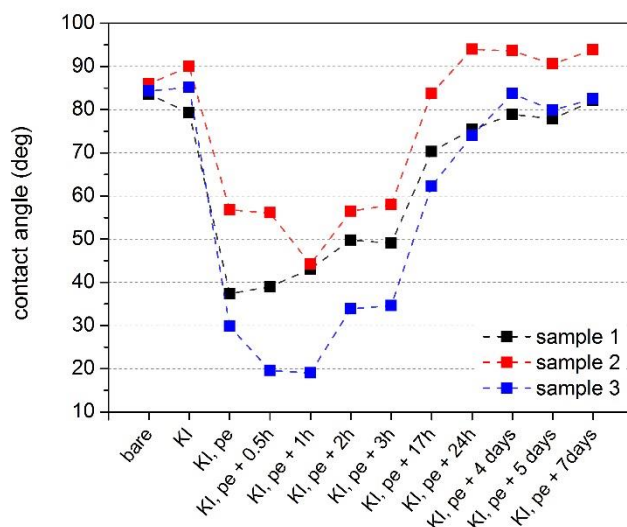


Figure 4. 26 – Evolution of the contact angle for three samples over one week monitoring after post-treatments (KI: wet etching, pe: O₂ plasma post-etching). Joining dashed lines included to guide the eye.

All the three samples start with a similar WCA around 85°. The wet etching by means of a KI dissolution does not affect significantly the WCA, which stays quite hydrophobic in a range between 80° and 90°. The plasma post-etching makes the surfaces hydrophilic, but with high variability among the three samples. This variability is kept during the monitoring of the first three hours after the post-treatments and can be ascribed to a limit of the WCA methods in case of highly hydrophilic surfaces: indeed, the spreading of the water droplet makes difficult a proper definition of the contact angles and measurement artefacts appear. After 17 hours all the samples start to recover a partial hydrophobicity and after one day of ageing, the value of WCA tends to stabilize and to recover a value close to the initial one. This result is particularly useful to select the proper wettability of the surface in view of a specific application.

In Table 4.3 it is possible to observe the WCAs of gold/PMMA plasmonic surfaces after different surface post-treatments, made without and with thermal annealing. In general, after annealing the surface appears more hydrophobic. This results is in good agreement with the aforementioned XPS results and can be ascribed to the disappearance of the O=C-OR binding after thermal annealing. On the other hand, the wet etching does not affect significantly the surface hydrophobicity. The O₂ post etching makes the surface extremely hydrophilic and the WCA measured one hour after the treatment is very low, especially when the annealing is performed. The WCA recovery after 1 day shows a faster rise to a more hydrophobic value for the sample without annealing ($68 \pm 2^\circ$) if compared to the one with thermal treatment ($20 \pm 1.9^\circ$).

Table 4. 3 – Contact angles in water for gold/PMMA plasmonic surfaces (500 nm pitch) after different surface post-treatments (ann: thermal annealing, KI: wet gold etching, pe: O₂ plasma post-etching).

Sample	Contact angle
PMMA_NO ann	84 ± 1.2°
PMMA_NO ann_KI	84 ± 5.3°
PMMA_NO ann_KI_pe	19 ± 3.5°
PMMA_NO ann_KI_pe, 1 day recovery	68 ± 2°
PMMA_ann	93 ± 4.2°
PMMA_ann_KI	87 ± 7°
PMMA_ann_KI_pe	< 10°
PMMA_ann_KI_pe, 1 day recovery	20 ± 1.9°

An additional sample was fabricated to investigate the influence of the annealing as last treatment, sequential to wet and plasma etching. As a starting point a plasma post-etched sample, after 3 hours of ageing, was considered. Reflectance spectra in air and sensitivity to small refractive index changes (Figure 4.27) do not show any significant change of the localized plasmonic mode centered at around 800 nm, even if an ulterior O₂ plasma etching is performed.

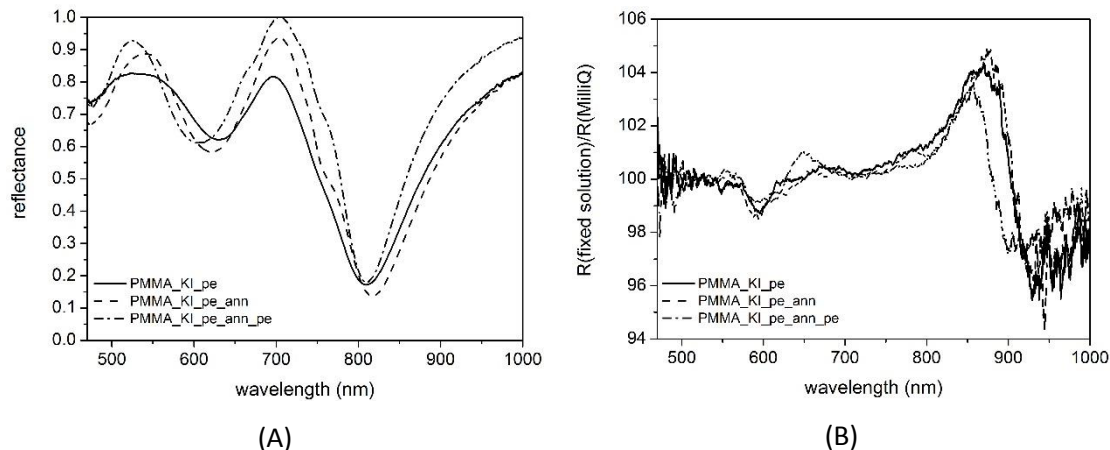


Figure 4. 27 - Reflectance spectra in air of a sample obtained with gold/PMMA structures (500 nm pitch) and annealing process sequential to wet and plasma etching (A) and ratio of the reflectance spectra in fixed solution to reflectance spectra in Milli-Q (B).

The WCAs collected in Table 4.4 reconfirm that the annealing treatment affects the surface hydrophobicity but the contact angle reaches a lower value if performed after the etching process (69 ± 6°). On the opposite, it is also possible to notice that a further O₂ plasma etching significantly modifies the surface features resulting in a really hydrophilic surface even after one day of ageing.

Table 4. 4 - Contact angles in water of gold/PMMA plasmonic surfaces (500 nm pitch) made with annealing process sequential to etching post-treatments (ann: thermal annealing, KI: wet gold etching, pe: O₂ plasma post-etching).

Sample	Contact angle
PMMA_KI_pe	47 ± 3.4°
PMMA_KI_pe_ann	69 ± 6°
PMMA_KI_pe_ann_pe	<10°
PMMA_KI_pe_ann_pe, 1 day recovery	24 ± 7°

4.3.4 STUDY OF DIFFERENT GOLD DEPOSITION METHODS

The purpose of this section is to describe the effect of a different gold deposition method and the most appropriate surface post treatments to improve the optical response of the nanocavity structures. In particular, magnetron sputtering deposition (MSD) and thermal evaporation (TE) were considered as deposition methods, while annealing or a combination of annealing and wet/O₂ plasma etching were studied as surface post-treatments. The samples issuing from this study are resumed in Table 4.5. The samples labelled as MSD correspond to the samples obtained with the standard fabrication protocol, indicated as 'PMMA' in the previous sections.

Table 4. 5 - Sample overview of Au cavities (500 nm pitch) made with different gold deposition methods (MSD: Au magnetron sputtering deposition, TE: Au thermal evaporation, ann: thermal annealing, KI: wet gold etching, pe: O₂ plasma post-etching).

	Sample	Surface treatment		
		Annealing	Wet etching	O ₂ post-etching
Batch 1: MSD	MSD			
	MSD_KI_pe		✓	✓
	MSD_ann	✓		
	MSD_ann_KI_pe	✓	✓	✓
Batch 2: TE	TE			
	TE_KI_pe		✓	✓
	TE_ann	✓		
	TE_ann_KI_pe	✓	✓	✓

All the samples were made with a PMMA layer of 150 nm, a colloidal mask of 500 nm PS beads, 4' of O₂ plasma etching and a nominal gold thickness of 150 nm. A different gold deposition method leads to different features of the cavities (Figure 4.28).

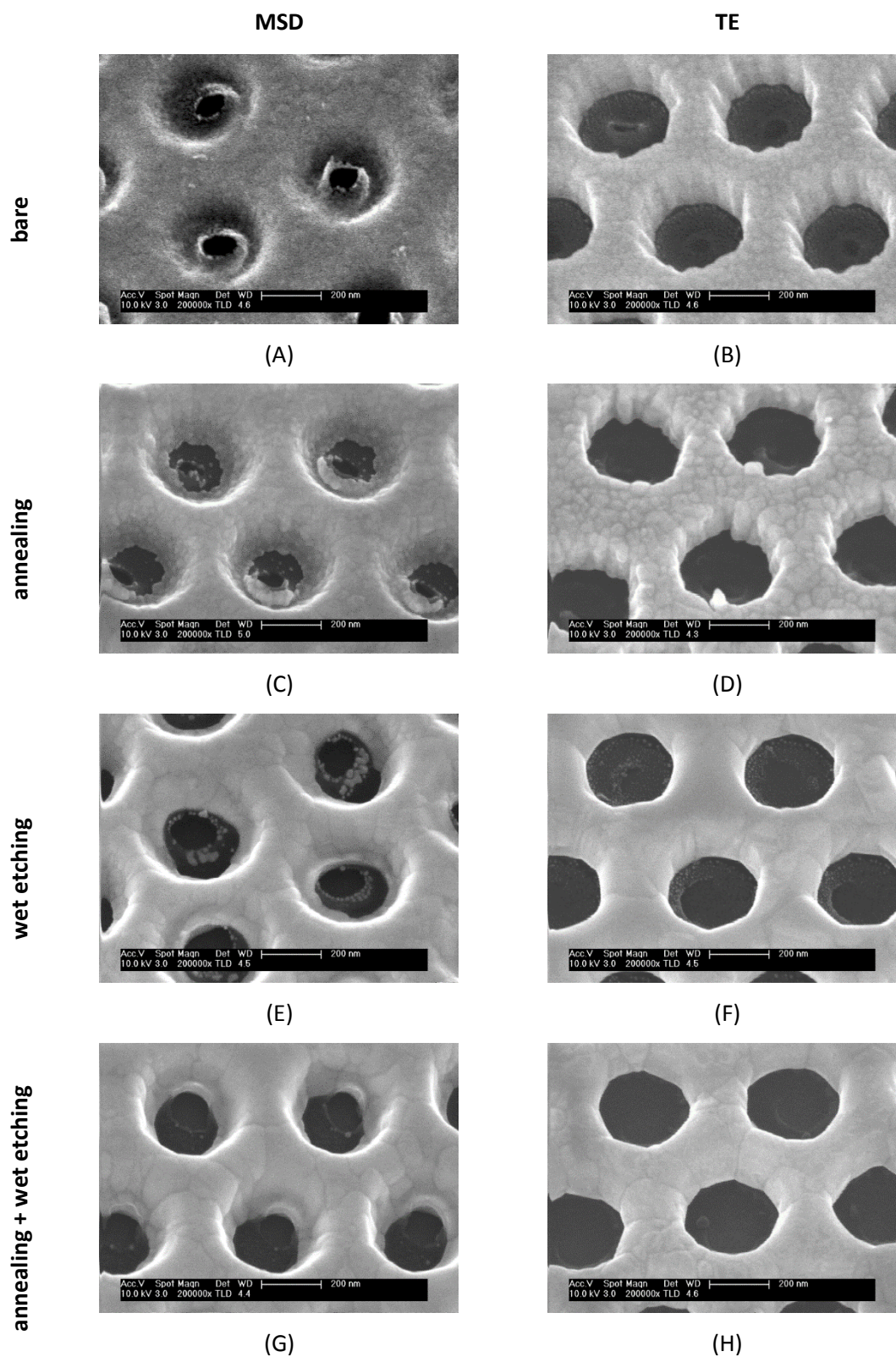


Figure 4. 28 – Au cavities (500 nm pitch) made with different gold deposition (MSD: magnetron sputtering deposition, TE: thermal evaporation) and surface post-treatments. (A) MSD, bare; (B) TE, bare; (C) MSD, wet etching; (D) TE, wet etching; (E) MSD, annealing; (F) TE, annealing; (G) MSD, annealing + wet etching; (H) TE, annealing + wet etching.

When sputtering is applied, a thin layer of gold is deposited inside the cavity, resulting in a gold corona around the top of the polymeric pillar. On the other hand, when thermal evaporation is applied, the deposition is more directional and leads to cavities with cylindrical walls and just few gold particles are visible on top of the polymeric pillars (Figure 4.28 A-B). A sequential wet etching by means of a KI dissolution has a double effect: it gently erodes the thin gold layer/particles on top of the polymeric pillars, opening the cavities and affects the bulk gold, making the grain boundaries more evident (Figures 4.28 C-D). In Figures 4.28 (E-F) it is possible to notice the influence of the thermal annealing: in both samples, the bulk gold appears smoother, more compact and made of bigger grains. In addition, for samples made by sputtering, the de-wetting of the thin gold layer inside the cavity is visible. A wet etching sequential to the annealing process has just a limited effect (Figures 4.28 G-H), since it just erodes the small particles inside the cavities, but the effect on the main gold structure seems negligible.

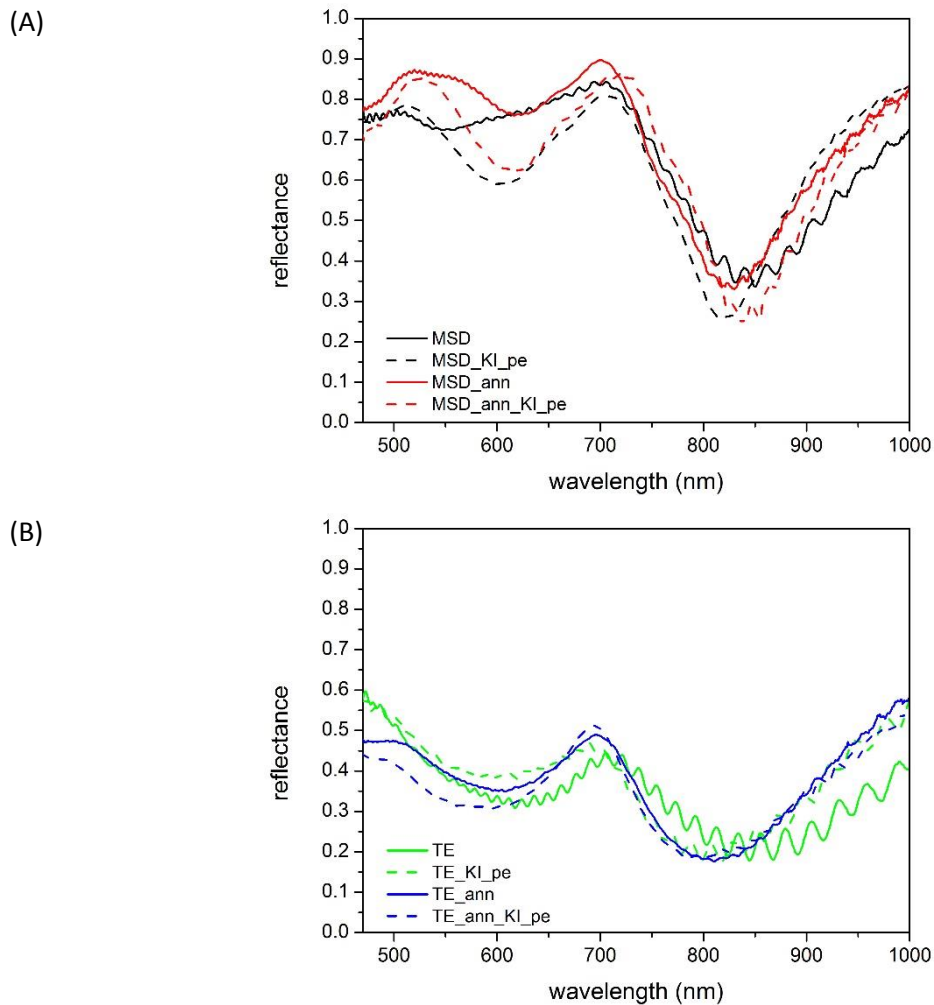
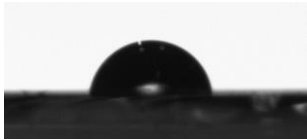
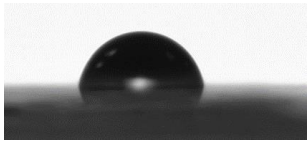

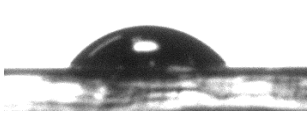
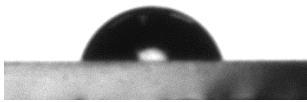
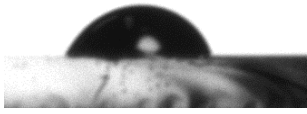
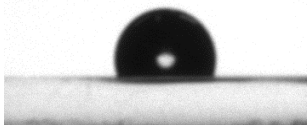
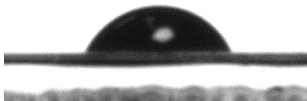


Figure 4. 29 – Reflectance spectra in air of samples (500 nm pitch) made by MSD (A) and TE (B) after different post-treatments (MSD: Au magnetron sputtering deposition, TE: Au thermal evaporation, ann: thermal annealing, KI: wet gold etching, pe: O₂ plasma post-etching).

A different cavity profile gives rise to a different optical behaviour of the surface (Figure 4.29). The higher level of gold filling with MSD results in higher reflectance in air and better defined spectral features. Samples made with TE show a wider minimum and an overall lower reflectance. In all cases, in good agreement with results exposed in the previous paragraph, a surface post-treatment (either annealing or wet/ O_2 plasma etching) moves the minimum at circa 850 nm towards lower wavelength.

Table 4. 6 - Contact angles of Au cavities (500 nm pitch) made by different Au deposition and surface post-treatments (MSD: Au magnetron sputtering deposition, TE: Au thermal evaporation, ann: thermal annealing, KI: wet gold etching, pe: O_2 plasma post-etching).

Sample	Contact angle	
MSD	$84 \pm 1.2^\circ$	
MSD_KI_pe, 1 week recovery	$86.1 \pm 6.7^\circ$	
MSD_ann	$93 \pm 4.2^\circ$	
MSD_ann_KI_pe, 1 week recovery	$55 \pm 3^\circ$	
TE	$78 \pm 3^\circ$	
TE_KI_pe, 1 week recovery	$70 \pm 5.5^\circ$	
TE_ann	$109 \pm 1.3^\circ$	
TE_ann_KI_pe, 1 week recovery	$65.5 \pm 4.4^\circ$	

The WCAs (Table 4.6) after MSD and TE are moderately hydrophobic ($84 \pm 1.2^\circ$ and $78 \pm 3^\circ$, respectively) and after the annealing treatment the hydrophobicity increases for both surfaces ($93 \pm 4.2^\circ$ and $109 \pm 1.3^\circ$, respectively). The values related to samples subject to wet and O_2 plasma etching are measured after one week of hydrophobic recovery and lead to slightly more hydrophilic surfaces, especially if these treatments for MSD samples are performed after the annealing.

4.4 CONCLUSIONS

In order to obtain a high-performance nanostructured surface (in terms of morphology, size and spacing) to be applied as plasmonic biosensing platform, we investigated several parameters. Indeed, the efficient flexibility of the fabrication process results in a wide range of selection of plasmonic surfaces with tailorable properties depending on the desired interaction with target biomolecules.

The use of polystyrene colloidal monolayers made of different particle diameters allows one to define a different pitch of the plasmonic crystals and consequently a different position of the plasmonic peaks. Small pitch (400 and 500 nm) sensing surfaces show higher sensitivity to refractive index change in the Vis-NIR range, which makes them particularly suitable for the integration into optical systems. Moreover, the use of monolayers of SiO_2 particles allows the efficient and tailorable nanostructuring of harder substrates, such as silicon.

A different combination of the polymeric layer, plasma etching process and gold layer deposition also acts as an effective tool for a flexible tuning of the structural features of the surface motives, which are strictly related to the optical behaviour of the plasmonic modes. Samples made by tapered PMMA pillars and gold deposited by means of magnetron sputtering present better control over reproducibility and higher sensitivity to refractive index changes.

A further investigation of the surface properties in terms of stability, topographic definition, wettability and cleaning was studied by introducing different post-treatments. In particular, we evaluated the single and combined effect of an annealing treatment (at $300^\circ C$), a wet etching of the gold layer and an O_2 plasma post-etching. The thermal annealing improves, at the same time, surface stability and sensitivity. The wet etching gently cleans the superficial Au layer, while the O_2 plasma post-etching positively affects the polymeric cavity, leading to more sensitive surfaces with controllable wettability.

CHAPTER 5

APPLICATION OF PLASMONIC SURFACES

This chapter aims at presenting two examples of application of the plasmonic surface based on gold nanocavities on polymer pillars described in Chapter 4. In the first example, the nanostructured chip is used as a sensing and label-free multiplexing platform in the Imaging Nanoplasmonics device (iNPx™), an SPR imaging system developed in-house by Plasmore Srl and tailored to read the chip response [137]. The other example relates to the application of the plasmonic gold/polymer nanocavities as optimized substrate for SERS [139].

5.1 SPR IMAGING APPLICATION

5.1.1 CHIP CHARACTERIZATION

The sensing chip consists of a hexagonal lattice of polymeric pillars (ppAA thickness 150 nm, pitch 500 nm) embedded in an optically thick gold film deposited on a glass substrate. The fabrication process is based on a combination of colloidal lithography and plasma processes as described in Chapter 4 and in previous papers [141-143]. As a result, the optical response of the final surface can be described in terms of plasmonic excitation localized inside the ppAA pillar (the main resonance is shown as a reflectance minimum at circa 850 - 900 nm) and delocalized modes around 550 nm related to SPPs propagating at the film interfaces. Moreover, the localized modes enable the coupling between the SPPs supported by the opposite film interfaces (gold/air and gold/glass), even if the gold film is relatively thick (~100 nm) and allows the detection of a refractive index change at the free surface of the chip by measuring reflectance spectra with light coming from the substrate side.

The optical characterization of the sensor chip was carried out by reflectance measurements, performed using a commercial Fourier transform spectrometer (FT-66, Bruker) equipped with a homemade variable angle micro-reflectometer. In addition, a prototypal device of the biosensor setup was developed by assembling a Xenon lamp as a light source, a beam splitter to send the light to the sample and a compact CCD spectrometer (OceanOptics) to collect the reflected

beam. High-sensitivity detection was performed by a double beam UV-VIS-NIR spectrometer (Varian Cary6i), working in the spectral range of 400 to 1250 nm with TM polarized light radiating the samples from the substrate side and equipped with a sample holder coupled to a home-made cell allowing the solution to flow on the chip surface.

First of all, the chip response was evaluated in terms of changes to small refractive index variations; in particular, refractive index variations from $4 \cdot 10^{-3}$ refractive index units (RIU) down to 10^{-6} RIU (which defines a response unit or 1 RU) with respect to water have been explored. Different concentration ranges of several aqueous solutions have been tested: [0.0004 – 2] wt. % of NaCl, [0.0004 – 3] % of glycerol, and between [0.006 - 3.16] % of ethanol. An Abbe refractometer (Zeiss) was used to directly measure the refractive index of the more concentrated solutions, while the lowest concentrations were extrapolated from those measured. Then, reflectance measurements were performed by making first pure water flow in the cell and then the contrast solution at a given concentration, followed by a final step of rinsing in milliQ water. Figure 5.1 shows the measured refractive index change with respect to milliQ water for the three solutions at different concentrations and the related chip response. The signal amplitude of the chip response is independent of the solution used, indicating that the signal variation depends mainly on the refractive index change and not on the eventual chemical species absorbed by the nanostructured surfaces.

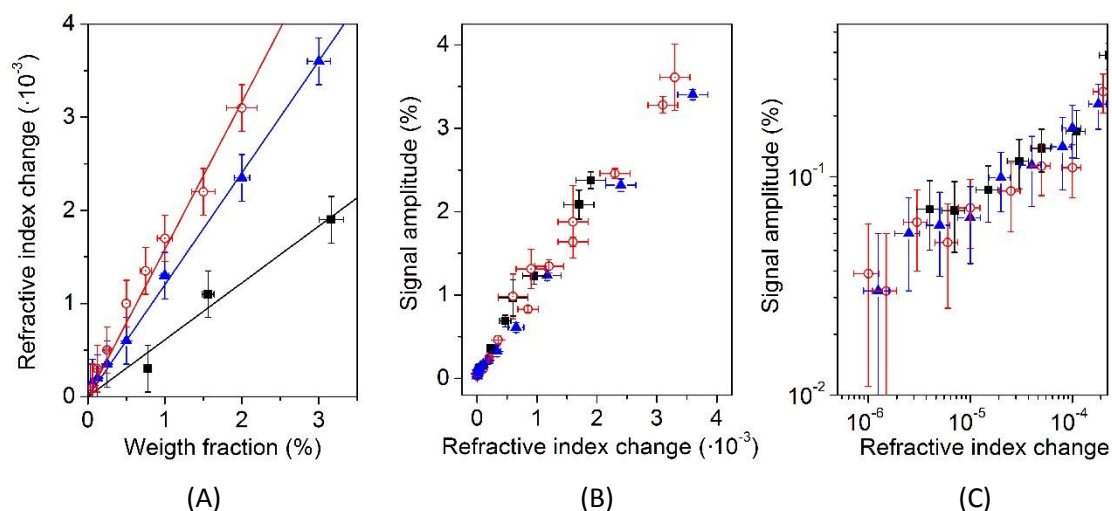


Figure 5. 1 – (A) Refractive index change with respect to milliQ water for NaCl (open circles), glycerol (filled triangles) and ethanol (filled squares) as a function of the solution concentration. (B) Chip response to NaCl (open circles), glycerol (filled triangles) and ethanol (filled squares) for high concentration data and (C) low concentration data in logarithmic scale.

The sensitivity in the region close to the top of the gold/polymer nanocavities, strictly related to the decay of the plasmonic field profile above the surface, has been measured by the evaluation of the chip response to the sequential adhesion of nanometric layers made of polyelectrolyte solutions of poly(diallyldimethylammonium chloride) (PDDA, Sigma Aldrich) and poly(sodium 4-

styrenesulfonate) (PSS, Sigma Aldrich) diluted at 2% in water. Figure 5.2 reports PDDA and PSS layers alternately deposited on plasmonic surfaces and the characterization of the reflectance response. Ellipsometric measurements performed after each deposition step allowed monitoring the polyelectrolyte film thickness and the nominal refractive index, which was found to be of 1.5 in agreement with literature [52]. To evaluate the growth on different substrates, polyelectrolyte layers were deposited on a ppAA-coated, as well as on a gold-coated flat silicon surface. In all cases, the chip was first coated with the positively charged PDDA layer and then a negatively charged PSS layer was sequentially deposited, adding a rinsing step of milliQ water after each polyelectrolyte deposition to remove the residual unbound material and repeating the process for at least 30 times. The thicknesses of polyelectrolyte layers grown on ppAA substrate are in agreement with the nominal values during the first 10 deposition steps (1 and 3 nm for PDDA and PSS, respectively) but after these, the film total thickness increases by ~ 2 nm/layer, likely due to a non-linear and/or non-uniform density of the polyelectrolyte chains which results in a less uniform adhesion of the layers. A similar behaviour is observed when gold is used as a substrate, except for the deposition of the first PDDA layer, since its measurement is equal to zero, indicating that the first stable layer that adheres to the gold surface is made of PSS. The comparison of the spectrum in milliQ water and after the first PDDA deposition (Figure 5.2 A) shows a shift of the plasmonic resonances related to both localized and delocalized modes centered at around 900 and 590 nm, respectively, with a signal amplitude of 1.8%. After rinsing with water, the localized signal decreases, while the signal related to the SPP modes disappears. Indeed, the PDDA is not deposited on the flat gold but only on the ppAA pillar top (negatively charged), where the localized plasmon modes are mainly effective due to the distribution of the electric field. The sequential adhesion of PSS molecules to the sample surface induced an additional shift of the main spectral features and a larger amplitude of the signal (16.5%), related to the plasmonic modes and due to the higher thickness of the PSS layer. After rinsing in water, the signal decreases but the SPP mode did not disappear since PSS molecules could also adhere to the gold portion of the chip surface. During the third deposition step, the PDDA molecules adhere to the PSS layer, which covers the whole sensor area, leading again to a slight decrease of the signals related to both localized (Figure 5.2 B) and delocalized modes after water rinsing. The evolution of the signal amplitude after several successive depositions and recorded after the water rinsing for both localized and delocalized modes is illustrated in Figure 5.2 C. It is important to notice that the signal amplitude of the localized mode (confined inside the dielectric pillar top) is plotted as a function of the layer thickness calibrated by ellipsometry on the flat ppAA surface, while the SPP mode signal amplitude (supported by the gold surface) is plotted as a function of the layer thickness measured on flat gold. After 20 deposition steps,

corresponding to a layer thickness of ~ 50 nm, the signal amplitude related to the localized mode exhibits a saturation behaviour, while the signal related to the SPP mode keeps an almost linear growth. The saturation behaviour of the localized mode allows one to infer the penetration depth of the electric field in proximity of the chip surface, which is proportional to the effective electric field intensity at the exposed surface, by fitting the equation:

$$y(x) = A(1 - e^{-x/L}) \quad (5.1)$$

where A is a constant related to the saturation value, x is the thickness of the whole polyelectrolyte layer and L is the electric field penetration depth. The best fit gives a value for the penetration depth of ~ 34 nm, in good agreement with the value reported in the literature for localized plasmon modes, normally in the order of tens of nanometers [7, 43]. On the other hand, the curve related to the delocalized mode does not show any tendency towards saturation, indicating a larger penetration value in the order of hundreds of nanometers, again in good agreement with literature [7, 43]. The simultaneous presence of localized and delocalized plasmonic resonances makes the investigated surface sensitive to two different length scales and paves possibility of detecting small molecules.

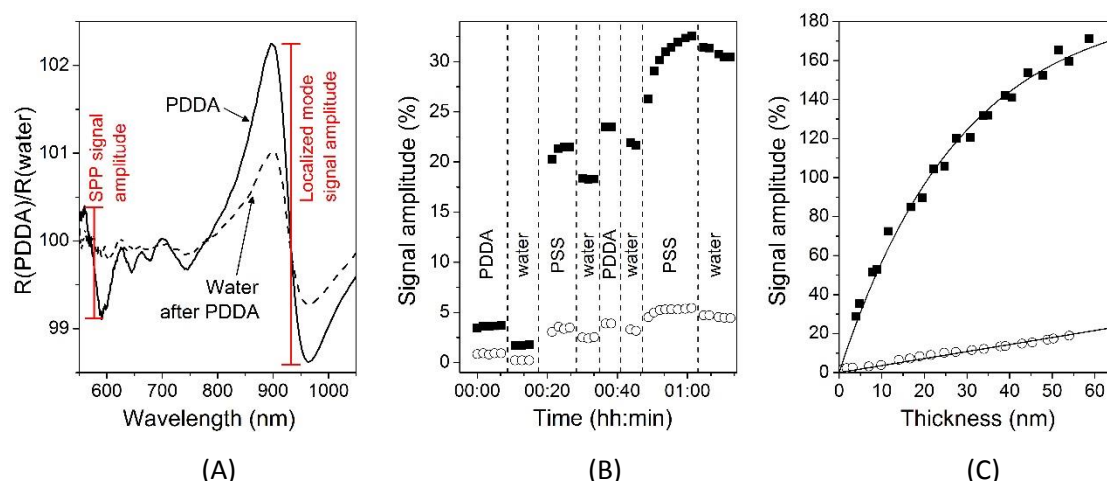


Figure 5. 2 – (A) Reflectance variation with respect to milliQ water, after the deposition of the first PDPA layer before (solid line) and after (dashed line) the rinsing with pure water. (B) Signal evolution around 900-950 nm during the first four steps of the polyelectrolyte deposition, relative to the shift of the localized (filled squares) and SPP (open circles) modes. (C) Signal amplitude of localized (filled squares) and SPP (open circles) modes after rinsing for each deposition step, as a function of the thickness of the deposited polyelectrolyte films.

5.1.2 iNPx CHARACTERIZATION

The iNPx™ device is a plasmonic microscope developed by Plasmore Srl and consists of a stand-alone, portable, multiplexing, label-free imaging system with integrated optics, fluidics, electronics, and computing as detailed in Chapter 2.

First, the sensitivity of the device to small refractive index changes has been assessed by testing glycerol solutions [0.0004 – 3 %], as done in the previous section for the characterization in spectroscopic mode. A calibration curve of the instrument is shown in Figure 5.3, where it is possible to notice a limit of detection down to 4 RU (1 RU = 10^{-6} RIU), in concurrence with alternative commercially available instrumentation[7].

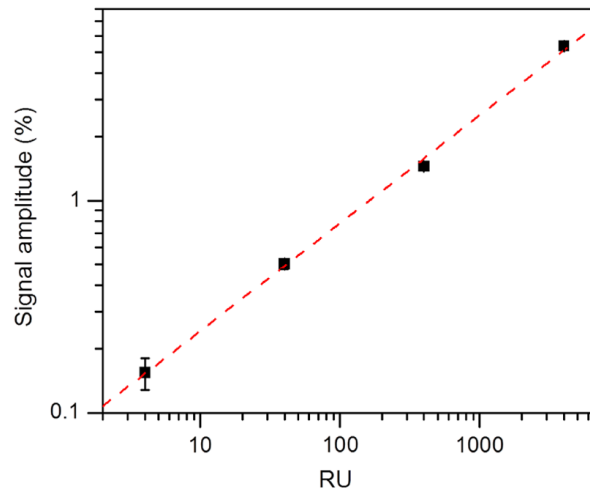


Figure 5. 3 – Calibration curve with glycerol solutions for the iNPx™ instrument.

5.1.3 DIAGNOSTIC ASSAY

As a proof of concept in a real diagnostic application, the biosensing performance of the iNPx™ has been tested for the detection of the long pentraxin PTX3. This molecule plays an important role in innate immunity and in the regulation of inflammation [144, 145]. Indeed, under physiological conditions, normal PTX3 blood levels are < 2ng/ml, but in case of sepsis they can increase to 200-800 ng/ml [144]. The PTX3 is characterized by a long, unrelated N-terminal domain associated to the C-terminal pentraxin-like domain [146], leading to a possible interaction with different ligands (such as microorganisms, the complement system, dead cells, modified plasma proteins, cellular receptors, extracellular matrix components, and growth factors). Indeed, several studies are in progress to evaluate the role of PTX3 as an effective biomarker involved in multiple biological events, including cardiovascular diseases, infections, tissue damages and tumors [146-152].

The performed biosensing assay involved the covalent immobilization of antibodies raised against PTX3 (Ab-PTX3) on mercaptohexadecanoic (MHD) acid monolayers previously self-assembled on the nanostructured chip surface and activated via EDC/NHS binding. A custom-made microcapillary pump consisting of seven independent microchannels and made of polydimethylsiloxane (PDMS) was used for the selective surface functionalization and immobilization: all the seven channels were activated using EDC/NHS protocol, then four of them (from top: channels 1, 3, 5, 7 in the optical image in Figure 5.4 A) were loaded overnight

with Ab-PTX3 (10 $\mu\text{g}/\text{ml}$ in 10 mM acetate buffer, pH= 5), while three of them were loaded with acetate buffer (channels 2, 4, 6 in the optical image in Figure 5.4 A) as negative control. After surface functionalization, the chip was mounted in the liquid cell and inserted in the iNPxTM reader. Figure 5.4 B shows the initial plasmonic image of the surface in air, where the index contrast between air ($n= 1$) and the PDMS ($n= 1.5$) gasket of the liquid cell in contact with the surface is well visible. The PBS buffer (pH= 7.4, Invitrogen) was then continuously dispensed to the liquid cell by the microfluidic system at a constant rate of 30 $\mu\text{l}/\text{min}$ and after the stabilization of the baseline, a 1% BSA solution in 1x PBS buffer was injected into the cell as a blocking agent for unreacted chemical groups on the surface. The difference image between the frame at $t= 600$ s and the reference image at $t= 0$ s shows a strong reflectance contrast between the different regions of the surface (Figure 5.4 C). In particular, the negative control channels show a higher reflectance and result brighter in the image compared to the Ab-PTX3 functionalized channels.

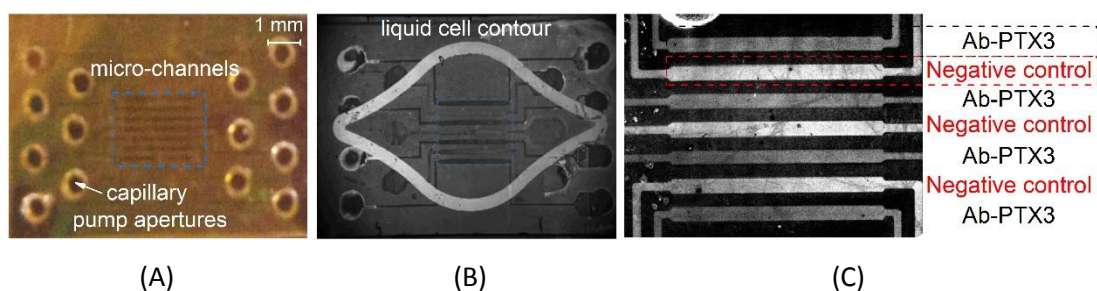


Figure 5. 4 - (A) Optical image of the microcapillary pump mounted on the plasmonic chip for surface functionalization. (B) Plasmonic image of the patterned chip inserted in the iNPxTM liquid cell. (C) Difference image between the frame at $t = 600$ s and $t = 0$ s for the blocking step (darker channels: Ab-PTX3, brighter channels: negative control).

As a next step, a new reference image was recorded and PTX3 diluted in 1x PBS buffer at 100 ng/ml was injected in the cell for 10 min. The surface was then rinsed by the reference buffer, to remove the excess of unbound/not-specifically immobilized PTX3 molecules. Finally, secondary antibodies at a concentration of 10 $\mu\text{g}/\text{ml}$ were used for a further amplification of the antigen/antibody signal. The sensorgram in Figure 5.5 A shows a higher reflectance within the channels related to the Ab-PTX3 immobilization with respect to the negative control channels, which is representative of a high affinity and specific antigen/antibody recognition, stable also after buffer rinsing and corresponding to a 0.1% variation of reflectance. Despite of this, a small non-specific binding of molecules can be seen in the negative control. When the secondary antibody is injected and after the rinsing with the buffer, the reflectance change with respect to the baseline rises to $\sim 0.3\%$ of the plasmon band intensity, confirming the specificity of the PTX3 recognition. Figure 5.5 B reports the difference image between the image at $t = 1600$ s and the

image at $t = 900$ s: the higher reflectance inside the Ab-PTX3 functionalized channels confirms the homogeneity of the signal and the successful specific recognition of the PTX3 molecule.

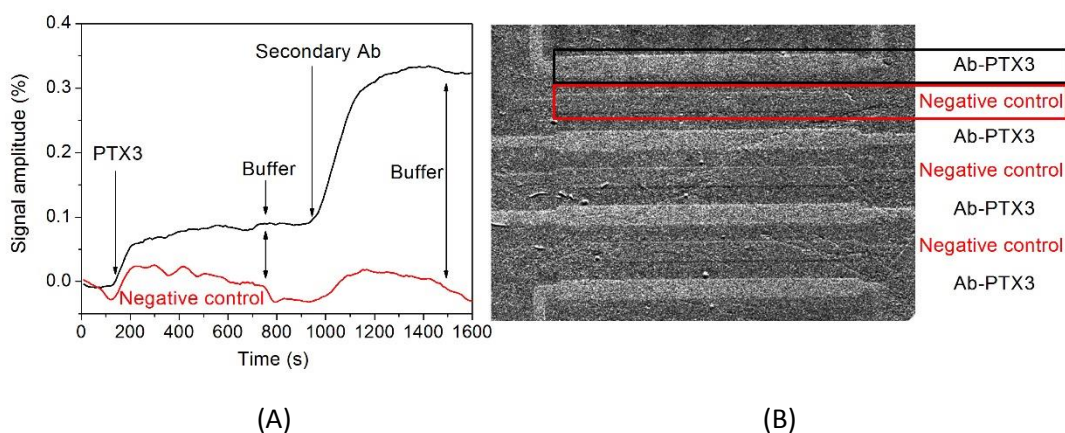


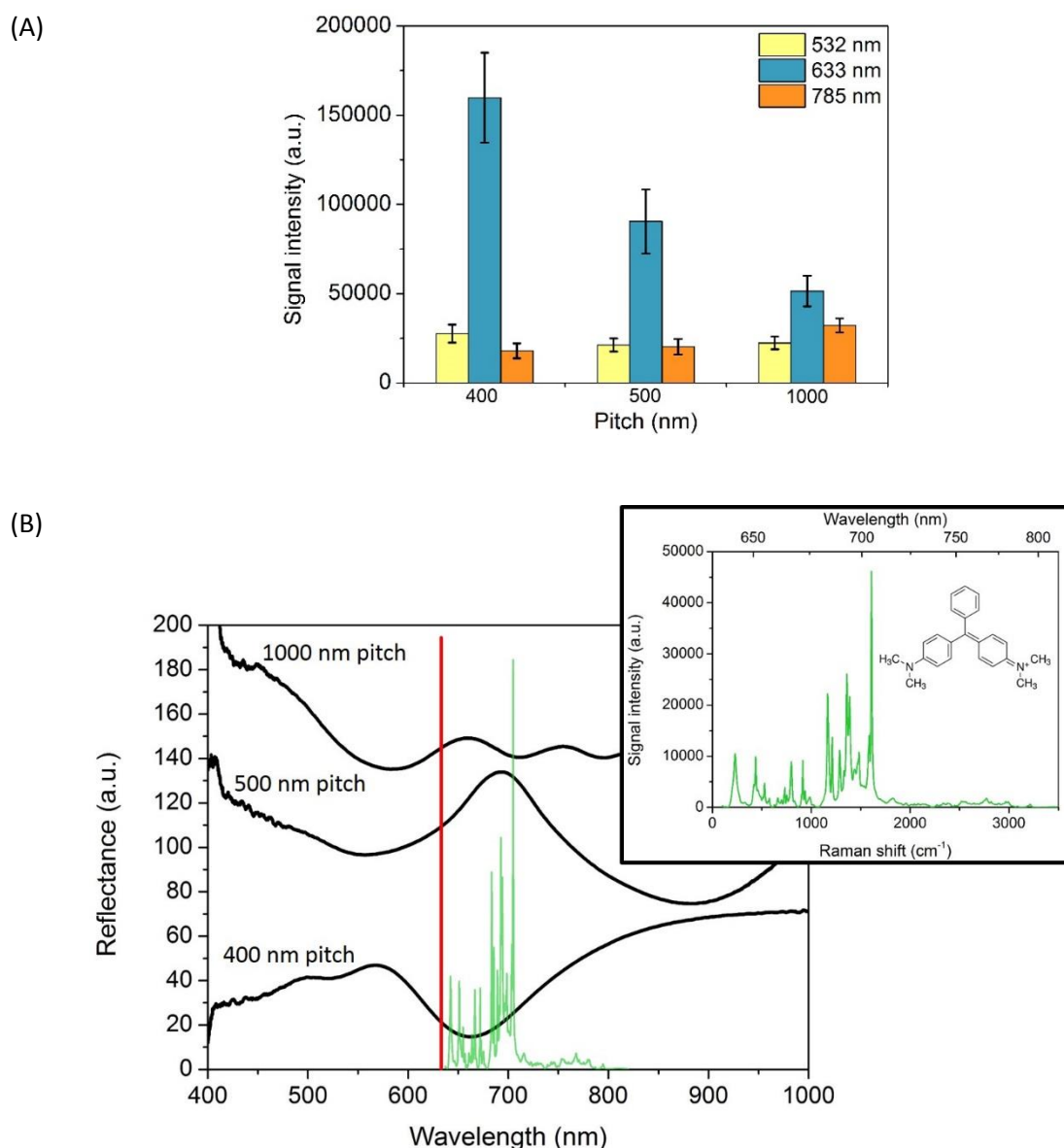
Figure 5.5 - (A) Sensorgrams representative of one Ab-PTX3 functionalized channel (black curve) and a negative control channel (red curve). (B) Image showing reflectance variation measured after secondary antibody injection and buffer rinsing (brighter channels: PTX3 detection, darker channels: negative control).

5.2 SERS APPLICATION

5.2.1 SURFACE OPTIMIZATION

The optimization of the surface features involved the investigation of different pitches (400, 500 and 1000 nm) and was carried out by using different colloidal monolayers as sacrificial masks. Different thickness (from 90 to 200 nm), both for the polymer and gold layer have been tested as described in Chapter 4. Raman spectra of the samples were acquired using an Aramis microscope (Horiba) equipped with three laser lines with different wavelengths of 532, 633, and 785 nm. The sample was positioned under the Raman microscope with the nanostructured surface facing up to acquire a single spectrum from a specific point of the chip (about 1.5 μm diameter). As already mentioned, the main parameters affecting the plasmonic properties are the geometric features (pitch and hole diameter), film thickness and composition. In our first experiment, the gold thickness was fixed to 150 nm and the dependence between surface pitch and laser excitation wavelength was studied. Figure 5.6 A shows that in the case of 532 and 633 nm excitation wavelength, a pitch of 400 nm provides the most intense Raman signal with an enhancement factor up to 10^4 , while the 785 nm laser gave the best results with the 1000 nm pitch sample. If reflectance measurements in air are considered (Figure 5.6 B), it is possible to notice that the 400 nm pitch samples show a well-defined reflectance minimum at around 660 nm, 500 nm pitch samples have one deep and a less strong minimum at around 878 and 557 nm, respectively, while the 1000 nm pitch samples have a broadened spectral curve with three

similar local reflectance minima at 590, 700, and 790 nm. A comparative analysis of the Raman signals and reflectance spectra shows that the most intense Raman signals are collected when the reflectance minimum of the substrate lies between the wavelength of the incoming laser light and the wavelength of the analyte's fingerprint region (the 1000-1700 cm^{-1} range in the Raman spectrum of malachite green corresponds to wavelengths between 675 and 710 nm using a 633 nm laser, as shown in the inset of Figure 5.6 B), in good agreement with literature [153]. In particular, best results in terms of higher signal intensity of the malachite green analyte were obtained with 400 nm pitch samples and 633 nm laser light.



Then, 400 nm pitch samples with various gold thicknesses were used to test the effect of the thickness of the structure on Raman signal enhancement, while the excitation wavelength was fixed at 633 nm. In addition, since the glass substrate allows the detection from the two sides (Figure 5.7 A), the effect of a different substrate orientation was studied by placing the sample under the microscope with the nanostructure facing up (“Up” mode) and facing down (“Down” mode). A different sample orientation is particularly useful in view of integration of microfluidic components. Best results were obtained in “Up” mode (Figure 5.7 B), where a gradual improvement of the signal was registered with increasing gold (and polymer) thickness. Despite of the good results obtained with 200 nm gold thickness, the fabrication process of these samples needs a special care because they are at a limit edge for a successful removal of the colloidal mask residuals. Indeed, an incomplete bead removal can limit the geometrical tunability of the 2D nanopillar arrays and negatively affect the extraordinary transmission related to the localized SPR. When the samples are analysed in “Down” mode (Figure 5.7 B), the collected signal changes only slightly with the gold thickness and is very similar to the signal collected from the air side up to 130 nm. If the gold thickness increases, the signal detected in “Down” mode decreases significantly when compared to the one in “Up” mode.

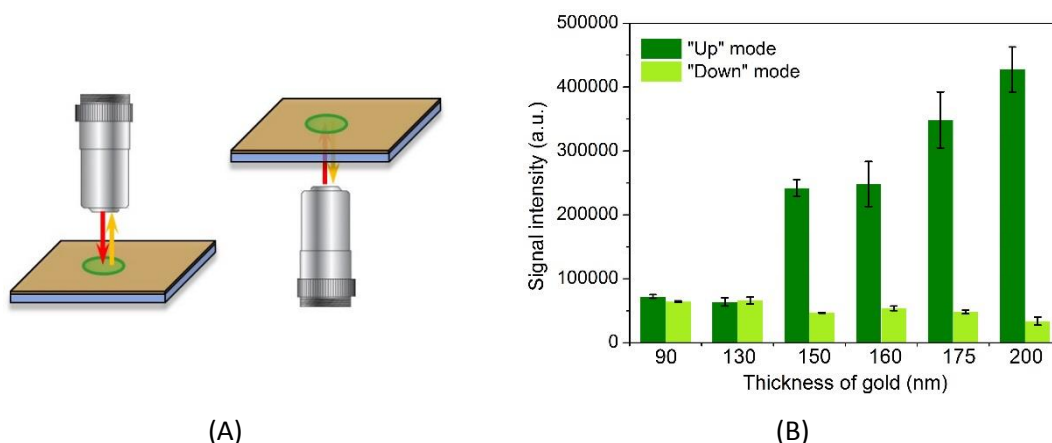


Figure 5. 7 - (A) Schematic of the excitation (red arrow) and detection of light (yellow arrow) from the air side (“Up” mode, left) and from the support side (“Down” mode, right). (B) Malachite green SERS signal intensity on the chip surface measured in “Up” mode (dark green bars) and “Down” mode (light green bars) for 400 nm pitch samples at 633 nm excitation wavelength.

In order to assess the repeatability of the results and decrease the signal intensity deviations caused by surface inhomogeneity, the samples were also scanned with the DuoScan function of the Raman microscope, which allows one to acquire spectra in mapping mode. The laser spot is continuously moved by a combination of scanning mirrors on an area having a defined shape and size. As a preliminary step, Raman spectra of a monolayer of malachite green isothiocyanate adsorbed on the gold surface were measured by performing 36 different acquisitions fixed on a single point (1.5 μm diameter) and distributed on an area of (50 x 50) μm^2 . The results in Figure

5.8 A show a general good homogeneity of the surface with a standard deviation of about 13% calculated on the average signal of the peak at 1168 cm^{-1} . Then, the samples were scanned in DuoScan acquisition mode: signals from 36 different contiguous square regions ($8 \times 8\text{ }\mu\text{m}^2$) were collected, thus covering the signal from the entire area of $(50 \times 50)\text{ }\mu\text{m}^2$ by spatial averaging the spectra. Figure 5.8 B shows a standard deviation of about 4% on the average signal, but the average intensity appears to be lower due to the decreased laser density on the surface.

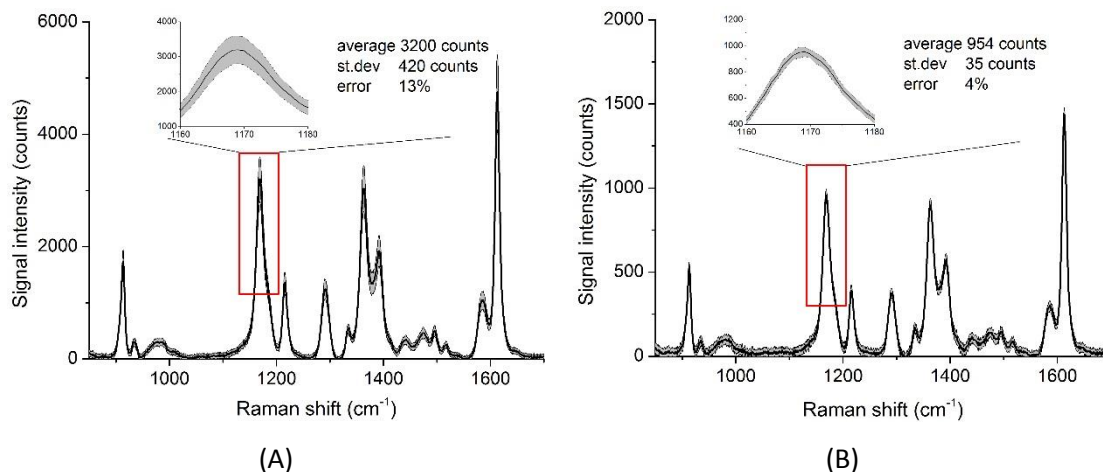


Figure 5. 8 - SERS spectra of a monolayer of malachite green isothiocyanate adsorbed on the SERS substrate acquired using the standard configuration of the microscope (A) and the DuoScan acquisition mode (B). The full line is the average of the 36 measurements used for the analysis and the grey shadow represents the standard deviation. Insets in the two graphs show the peak at 1168 cm^{-1} used to calculate the error.

The better reproducibility of results in DuoScan mode (i.e., the lower standard deviation) is strictly due to the relation between the surface pitch and the dimension of the laser spot. Indeed, when the acquisition is fixed in a single point, a different number of polymeric pillars can be illuminated by the laser depending on its position. Differently, in DuoScan mode, the illuminated area is much larger and the number of analyzed pillars is quite constant, resulting in an improved reproducibility.

5.2.2 DNA RECOGNITION AND MICROARRAY ASSAY

The framework of the application relates to the study of minimal residual disease (MRD) in patients affected by acute myeloid leukemia, a situation in which, after the chemotherapeutic treatment, a complete recovery is limited by residual cancer cells still able to proliferate and often with new mutations that lead to the artificial selection of drug resistance. Indeed, there is a relevant interest in studying novel analytical solutions for the sensitive, fast, and multiplexing detection of several MRD and drug resistance biomarkers [154, 155]. In our assay, the Wilms tumor (WT1) DNA target was chosen as one of the most studied biomarkers for the monitoring of the MRD [156] and it is normally evaluated in relation to the expression of the housekeeping

gene ABL (control model). The P-glycoprotein (P-gp) target was selected as a model for the overexpression of multi-drug resistance protein, often induced by chemotherapeutic treatment [157].

The SERS assay used for the DNA recognition is based on the immobilization of functionalized gold nanoparticles on the nanostructured chip surface (Figure 5.9). The experiment protocol can be resumed in few steps:

- Synthesis of spherical gold nanoparticles (diameter= 35-40 nm) using citrate as reducing agent;
- Functionalization of gold particles with a target sequence of 5'-thiolated ssDNA oligonucleotide (Primm) and coupling with dye molecules by incubation with rhodamine, malachite green or eosin isothiocyanate;
- Functionalization of the chip surface with thiolated oligonucleotides (100 μ M) and passivation of the unfunctionalized regions with polyethylene glycol methylether thiol (PEG-SH);
- Dipping of the nanostructured chip in a suspension of functionalized gold nanoparticles, addition of target DNA (WT1, ABL, P-gp) and setting of a proper annealing reaction to favour the binding of complementary sequences. The efficient binding between gold nanoparticle and plasmonic surface is promoted because they were conjugated with DNA probes complementary to different portion of the target DNA sequences, allowing a specific immobilization. A negative control was prepared without the addition of target sequence;
- Scanning with the Raman microscope.

The fingerprint analysis of SERS labels offers a valuable alternative to conventional fluorescent strategies and allows one to avoid undesired photobleaching of organic fluorescent labels or quenching of quantum dots. In our functionalization protocol, the strong binding of the isothiocyanate to gold results in a structure where the free surface between the already attached thiolated oligonucleotide chains becomes filled with high Raman cross section molecules, stable in the buffer and easy to separate from unreacted material. Moreover, functionalized gold nanoparticles provide an enhancement of the Raman signal, since they offer a multiplication of the number of Raman scattering label molecules corresponding to one target oligonucleotide and they are covalently bound to the chip surface in very close proximity to the nanocavity borders (Figure 5.9 B) where the electromagnetic field is demonstrated to be particularly strong [143].

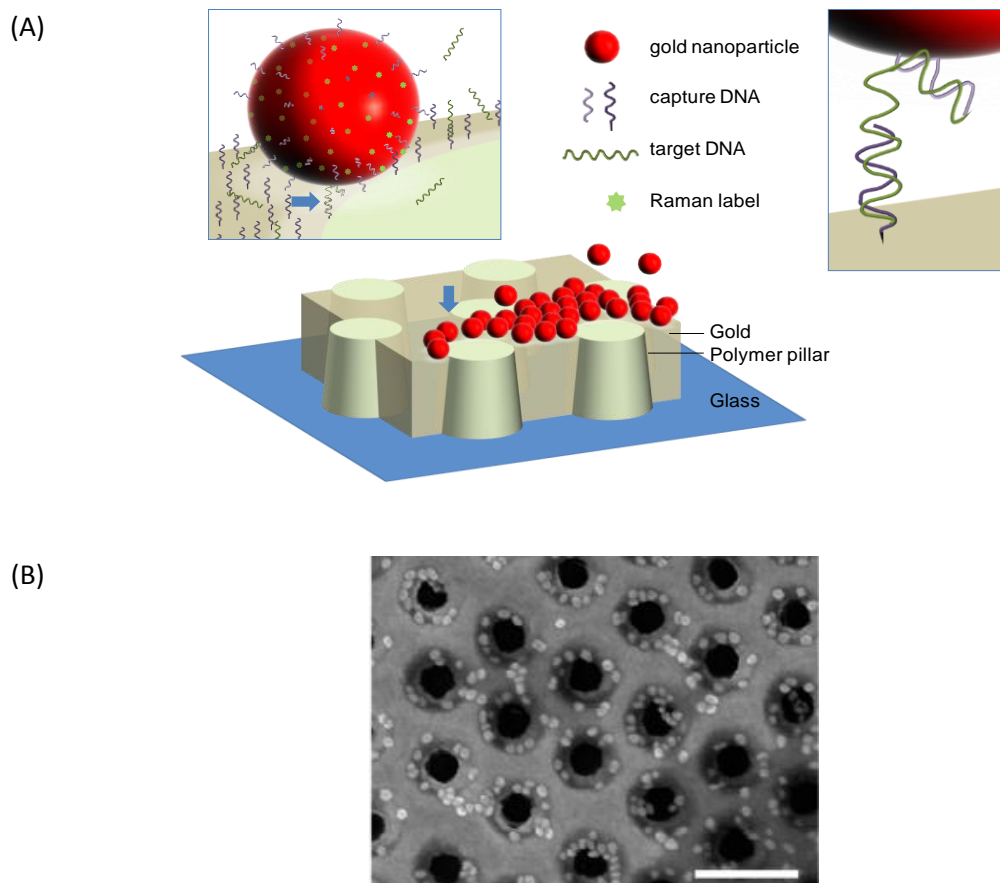


Figure 5. 9 - (A) Schematic of the DNA recognition assay. Insets: (left) non-labeled target DNA annealed with the complementary capture sequences on the chip surface and on the nanoparticles, resulting in particle immobilization on the surface; (right) annealing of complementary sequence immobilized on the gold surface of the nanoparticles. (B) SEM image of the substrate after the annealing between the sequences conjugated on the surface and on the nanoparticles. Gold nanoparticles are visible as brighter spots around the surface cavities. Scale bar: 500 nm.

The immobilized particles act as hot spots for the SERS detection of the labelling dye molecules, resulting in a 5-fold increase of the collected SERS signal in comparison to an analogous experiment performed on flat gold (Figure 5.10).

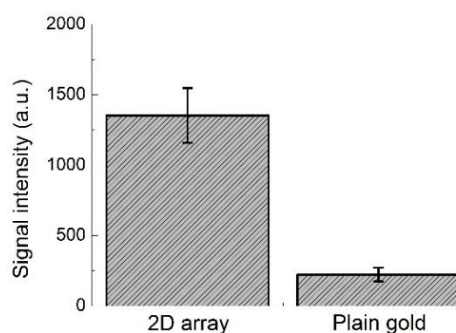


Figure 5. 10 - Signal intensity measured during a microarray experiment using the 2D plasmonic crystal (left) and plain gold (right). Target sequence concentration: 20 nM.

In order to assess the sensitivity of the surface, a one-step annealing experiment at various WT1 sequence concentrations (200, 100 and 50 nM) on a chip functionalized with a pattern of double columns of WT1-specific and ABL-specific (negative control) capture sequences was performed in a microarray format. Figure 5.11 shows the results of the detection using the DuoScan mapping mode: the brightness of the spots corresponding to the WT1 target gene presence is concentration-dependent, while the dark areas relate to the absence of the ABL control, suggesting that the unspecific binding is basically equal to the binding on PEG-passivated areas.

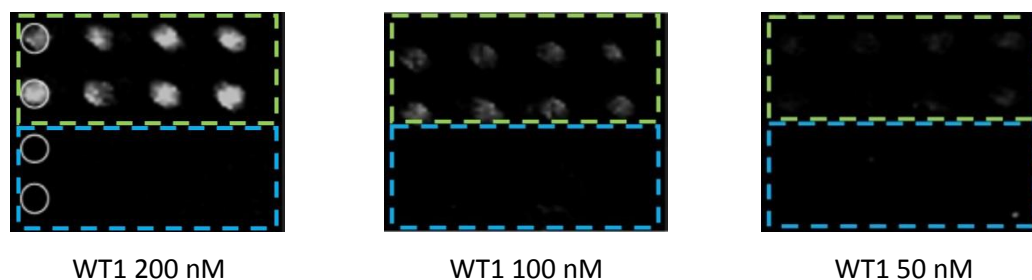


Figure 5. 11 – Brightness maps of the signal intensity detected by the Raman microscope from the chip surface functionalized with WT1 capture oligonucleotide (green dashed square) and ABL negative control capture oligonucleotide (blue dashed square) at 200, 100, 50 nM concentration of the target WT1 sequence. Circles in the first frame evidence the first column of spots.

In addition, the detection limit of the platform was tested in a one-step assay system, where target DNA and gold particles have been simultaneously put in contact with the functionalized surface. The detection limit was found to be around 2 pM (Figure 5.12).

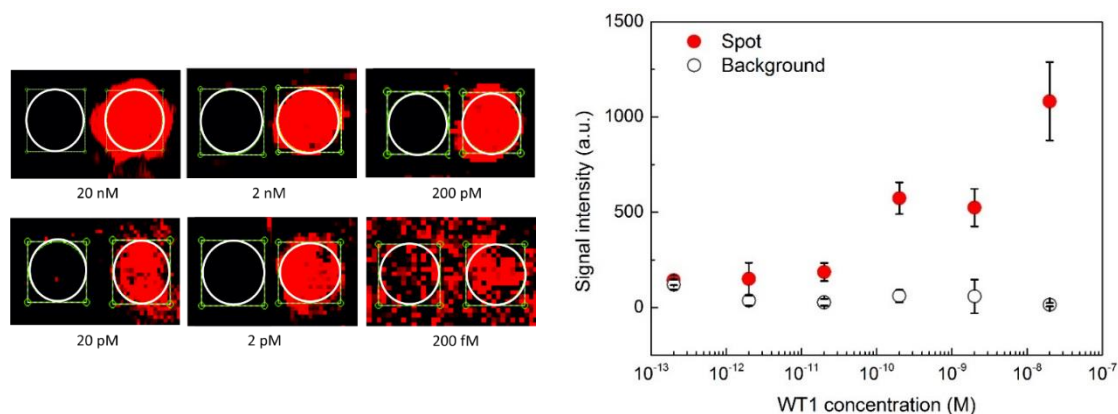


Figure 5. 12 - Raman images of the one-step assay obtained using different concentration of the target gene WT1 (left) and signal intensity at different concentration of the target sequence inside the spots (filled red circles) and in the background (open circles) (right).

Finally, the multiplexing capabilities of the system have been demonstrated by SERS fingerprint of different Raman dyes. Indeed, gold nanoparticles were functionalized with different capture DNA and covalently bound to eosin, rhodamine and malachite green isothiocyanate molecules. The chip surface was covered with a DNA array made of three different capture oligonucleotides (WT1, P-gp, and ABL), spotted at a concentration of 100 mM by means of a S3 sciFLEXARRAYER

(Scienion). Particles functionalized with the complementary sequences become immobilized on the specific spots in the presence of the target DNA strands and, since they carry different Raman dyes, the different spots can be identified by registering the SERS intensity profile of corresponding spectra after Raman mapping (Figure 5.13). Domains functionalized by different thiolated sequences can be clearly identified. It is noteworthy to underline that the spots of this experiment were about 150 μm in diameter with 500 μm pitch, which in principle could allow the deposition of 400 well-separated functionalized domains on overall area of the chip (approximately 1 cm x 1 cm), but different spotting parameters, as well as the scalability of the chip dimensions, can further improve the multiplexing and high-throughput capabilities of the detection system.

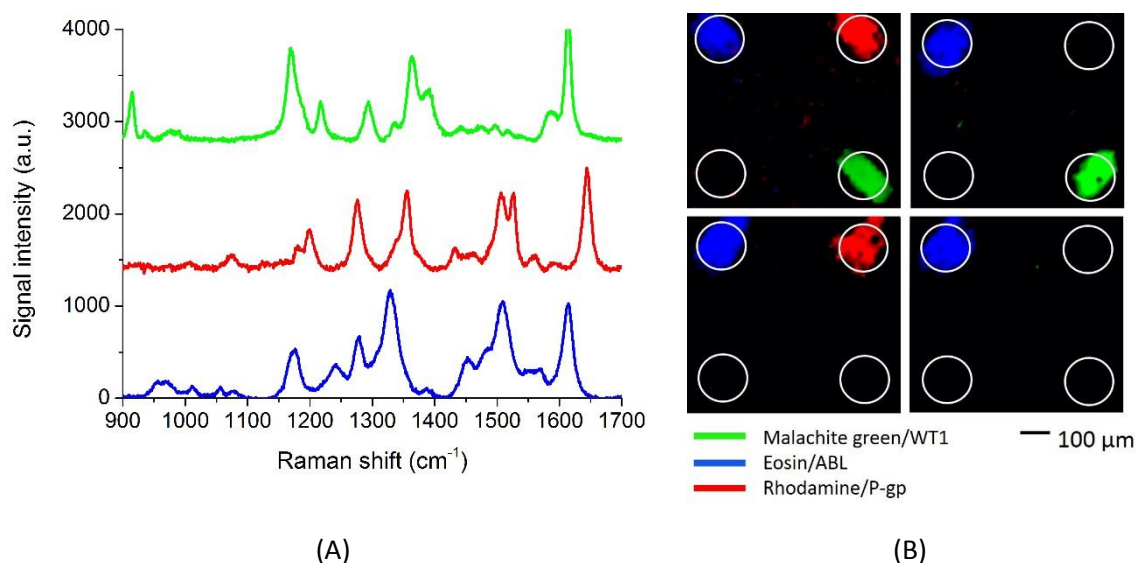


Figure 5. 13 - (A) SERS spectra of malachite green (green line), rhodamine 6G (red line), and eosin isothiocyanate (blue line) on DNA-functionalized gold nanoparticles. (B) Raman maps of DNA microarray with different capture oligonucleotides: WT1, P-gp, polyA, and ABL, after nanoparticle immobilization. Different target sequences were present in the incubation buffer: WT1, P-gp and ABL (map at the top left), ABL and WT1 (map at the top right), ABL and P-gp (map at the bottom left), ABL (map at the bottom right).

5.3 CONCLUSIONS

The bulk sensitivity of the nanostructured chip, probed by means of spectroscopic techniques, made possible to detect a refractive index variation of 10^{-6} RIU. The progressive deposition of polyelectrolyte layers showed a different sensitivity of the localized and delocalized modes (approximately eight times larger for the localized mode) and a different penetration depth of the electric field (approximately ten times lower for the localized mode).

The surfaces were tested within the iNpx™ device. The performances of the instrumentation have been characterized, especially in terms of multiplexing capabilities and sensitivity to

refractive index changes. Finally, a proof-of-concept application of the technology as a point-of-care tool for the detection of the diagnostic marker PTX3 was successfully presented.

As for the SERS application, the fabrication process was optimized in order to tailor the pitch and the spectral response of the crystal surface to the excitation wavelength of the laser light source. The successful test of these plasmonic surfaces in a biochemical assay for the simultaneous multiplexing detection of leukemia biomarkers (i.e., Wilms tumor gene), multidrug resistance and housekeeping gene expressions was demonstrated.

CHAPTER 6

CONCLUSIONS AND PERSPECTIVES

6.1 GENERAL CONCLUSIONS

This thesis aimed at the development of 2D colloidal crystals and at their integration into a multi-step nanofabrication process, in order to obtain plasmonic surfaces over large areas. We paid attention to solve a series of problems related to different topics, including colloidal lithography, thin film deposition and etching processes, as well as their effect on the optical response of the final nanostructured surface. Indeed, the flexibility of the fabrication method allowed us to tailor the spectral response of the surface by easily tuning the nanostructure features, with good control over reproducibility and high versatility in terms of materials and process parameters. All these different physical-chemical aspects have been optimized and the obtained surfaces were tested as efficient platforms for biosensing.

The main results achieved in this thesis can be regrouped in three different categories, strictly related and harmonized among each other: colloidal lithography, nanofabrication and optical response, biosensing applications.

Colloidal lithography

- The Langmuir Blodgett technique was systematically studied to obtain large-area crystalline monolayers. Indeed, this technique offered an efficient and cost-effective method to obtain 2D colloidal crystals with good control over defect formation and homogeneity, as well as high versatility in terms of particles to be transferred (polystyrene of different sizes and silica) and substrates where to transfer (polymer films, Si wafers, glass). Monolayers transferred on Si substrates were evaluated by observing the isotherm curves, collecting reflectance measurements and analysing SEM images.
- The Langmuir Blodgett isotherm curve related to the formation of 2D colloidal monolayers made of polystyrene particles was optimized by studying proper suspension-related parameters (spreading solvent, suspension volume).

- The control over the particle organization in terms of crystalline coverage and crystal domain dimensions was studied by playing with subphase-related parameters (pH, temperature). The selection of a pH of 6.5 and a temperature of 22°C during monolayer assembly and transfer represented a good compromise between well-ordered crystalline coverage and easier control over process conditions.
- Colloidal crystals made of inorganic SiO₂ particles were also studied as useful masks to nanostructure harder substrates (such as silicon and glass) due to their higher resistance to etching processes. We tested the activation with HF or HF/H₂O₂ and the functionalization with a F-silane in order to evaluate the effect of the surface modification on the particle buoyancy and, consequently, on the monolayer assembly. SEM images showed a well-ordered assembly only for particles functionalized after HF/H₂O₂ activation, but still comparable to the quality obtained with untreated particles.

Nanofabrication and optical response

- The proposed nanofabrication process was focused on a hybrid bottom up/top down approach based on a combination of colloidal lithography and plasma processes.
- The conditioning of bare SiO₂ monolayers by different etching conditions and the sequential deposition of an Au layer resulted in silicon pillars with tailorable shape and characteristic optical behaviour.
- The standard nanostructured plasmonic surface was a hexagonal lattice of polymeric pillars embedded in an optically thick gold film on a glass substrate. The use of a glass substrate made possible the energy matching of plasmonic modes at different interfaces and allowed an easier integration of microfluidic systems when light impinges from the substrate side.
- The plasmonic response is due to the contribution of delocalized and localized plasmonic modes, respectively related to the different grating interfaces and to the presence of dielectric cavities. The dependence of optical response on structural parameters was experimentally investigated by means of reflectance measurements and surface microscopy (optical, SEM, AFM).
- Different combinations of polymer film thickness, colloidal particle diameter (400, 500 and 1000 nm) and etching conditions were optimized to obtain sensitive and reproducible surfaces with different pitches.
- The calibration of the etching process allowed the reduction of the particle diameter within the colloidal mask and the modification of the pillar shape from tapered to truncated cone aspect. Reflectance measurements with light coming from the glass side proved that a tapered shape of the polymeric pillar determines a significant increase of the sensitivity due to

an improved localization of the electric field distribution close to the free surface. This effect was even more evident when a gold ring was present on the pillar top, since it acted as a metallic tip and forced the electric field resonance.

- The intermediate polymer film was engineered as first step towards tailoring of the pillar shape. This optimization involved the selection of polymer film thickness, polymer type (ppAA and PMMA) and deposition technique (PE-CVD and spin coating, respectively). In particular, spin coating offered a faster deposition and a better control over the reproducibility among batches.
- Several surface post-treatments were introduced to further improve the plasmonic performance. A thermal annealing at 300°C was proved to give more stability to the Au layer and to contribute to a better definition of the surface motives around the cavity top. A gentle and controlled wet gold etching by means of a KI solution eroded a thin superficial gold layer, cleaning the surface from possible contaminations. An O₂ plasma post-etching contributed to a better cleaning of the surface and to the adjustment of the pillar height inside the cavity; it also offered a control over the wettability of the surface, particularly useful in view of the possible surface functionalization and interaction with target biomolecules.
- Magnetron sputtering and thermal evaporation were tested as gold deposition methods. A different growth of the gold layer lead to a different cavity structure, which resulted in a higher sensitivity to refractive index changes when magnetron sputtering was considered.

Biosensing applications

- It has been possible to detect refractive index variations of 10⁻⁶ RIU, in good performance with respect to concurrent SPR instruments. The progressive adhesion of polyelectrolyte monolayers allowed us to reconstruct the decay of the electric field above the surface related to localized and delocalized modes. The higher sensitivity and lower penetration depth of the localized mode are especially promising to detect small molecules.
- The plasmonic surfaces were successfully tested within the Imaging Nanoplasmonics instrumentation (iNPX™, developed by Plasmore Srl) for the specific and multiplexing detection of the biomarker long pentraxin PTX3 in a sandwich assay format, in less than 30 minutes and with clinically relevant concentrations (100 ng/ml).
- The plasmonic surfaces were also tailored for SERS application and applied in a biochemical assay with labelled gold nanoparticles. The high enhancement of the signal was due to the hot spots given by the coupling of the localized surface plasmon present on the substrate and on the gold particles and resulted in the simultaneous multiplexing detection of leukemia biomarkers (i.e., Wilms tumor gene), multidrug resistance and housekeeping gene expressions with a detection limit (2 pM) close to the one of classical electrochemical-based approaches.

6.2 FUTURE PERSPECTIVES

Bimetallic structures

Typical nanohole arrays are made of gold films, but silver is a valuable alternative due to its lower cost, as well as to its lower absorption in the visible range and longer propagation length of the surface plasmon. As a drawback, the lower resistance to oxidative processes makes silver less stable than gold. To overcome this problem, bimetallic Ag/Au nanohole arrays are reported to protect the more chemically sensitive silver layer and to improve the enhancement by a proper matching of the plasmon bands depending on the multilayer composition. In addition, a final layer of gold offers a surface which can be easily functionalized by means of thiol chemistry. In the framework of SERS application, some bimetallic Ag/Au nanocavity arrays (1000 nm pitch, total film thickness of 400, 633 nm excitation wavelength) were investigated and, for specific bimetallic composition, resulted in better enhancing properties if compared with pure gold samples [139]. Further study is needed to identify the optimal combination between enhancement increase and chemical stability in relation with the silver proportion within the metallic multilayer. The same approach can be applied to investigate the enhancement of samples made of different pitch.

Surface functionalization

In order to improve the applicability of the proposed nanostructured chips, a further surface functionalization is under study. Once characterized and optimized, the functionalized surface will need to be tested in biochemical assays.

An ultrathin layer of silica (in the order of plasmon field penetration depth) was successfully applied to the nanostructures to tune the resonance mode and increase the sensitivity [158]. Indeed, there is a shift of the plasmon spectral position and an improvement in the slope efficiency. Moreover this layer offers encapsulation and protection of the metal phase, prevents excitation quenching and exposes a highly functionalizable surface (silica). The protocol for a reproducible deposition of the silica layer is still under optimization.

In addition, the surface patterning by means of a titania-acrylate composite can also be evaluated as an efficient lithographic technique to create specific surface properties (i.e., antifouling properties) [159].

Big area processing

The flexibility of the fabrication process paves the use of the proposed protocol to produce nanostructured surfaces on industrial scale. The substrates used in this thesis had a reduced dimension (in the range of 2-15 cm²), which made possible the parallel production of a limited

number of samples at the same time. Indeed, the main restriction relates to the dimensions of the reactor chambers and of the Langmuir-Blodgett trough, where the substrates have to fit. Preliminary results showed that the use of proper instrumentation (Langmuir-Blodgett model with a bigger trough and reactors with bigger processing chambers), together with the introduction of a final step to cut the substrate into small samples could allow working on wafer scale, resulting in a more cost-effective and less time consuming production. A proper cutting step (e.g., dicing, laser cutting) has to be evaluated in order to limit the surface damage. Moreover, the affordability of the sensitivity of the fabrication process has to be assessed in terms of homogeneity over large area and reproducibility among batches. A statistical analysis will have to be introduced in order to define proper parameters and tolerance ranges as a quality control after each step of the production protocol.

Hybrid system integration

The soft processing conditions of our fabrication protocol offer the possibility to integrate the nanostructured surfaces onto complex substrates (such as, for example, Bragg reflectors, Organic Light Emitting Transistors and Diodes) in order to obtain miniaturized, portable and low energy consuming sensing devices. The compatibility of each step has to be evaluated in terms of stability and reproducibility and, as proved in this thesis, can be easily and efficiently adapted in view of a specific application.

A proof of concept investigation related to the integration of the developed nanostructured surface and porous silicon (PSi) multilayers is under study. PSi is a well-known optoelectronic material and it has a great potential in a wide range of fields due to its tuneable effective refractive index, which can be tailored through a precise control of the formation parameters. It can be made by an easy and low cost process based on a computer controlled electrochemical etching of Si wafer in HF/EtOH electrolyte. To obtain multilayer structures, the applied current density was alternately switched between different values, resulting in low and high porosity layers. High/low porosity layer stacks result in optical multilayer interference filters, such as Bragg reflectors, with flexible selectivity of the wavelength tuning. Experimentally it has been possible to successfully grow plasmonic surfaces on top of PSi multilayers (Figure 6.1), which resulted in the coupling of their spectral response with high tunability of the optical behaviour over a wide range of wavelengths just by setting the proper fabrication parameters. Numerical simulations can be introduced to support experimental results and to refine a representative model of the hybrid system.

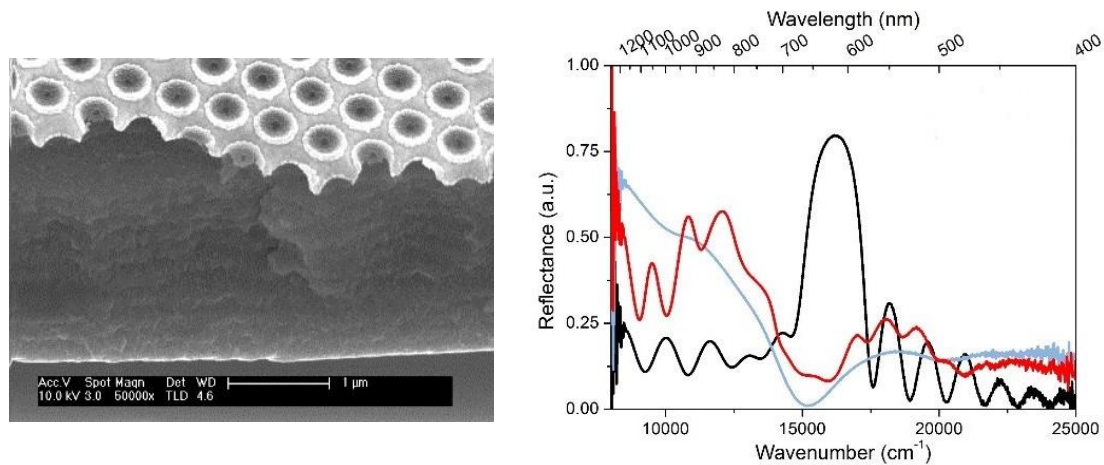


Figure 6. 1 - SEM image of the plasmonic surface grown on top of a PSi multilayer (top) and related optical response (bottom; black line: PSi multilayer, blue line: plasmonic surface, red line: hybrid system).

6.3 CONCLUSIONES GENERALES

El objetivo principal de esta tesis ha sido el desarrollo de cristales coloidales bidimensionales y su integración en un proceso de nanofabricación secuencial, con el fin de obtener superficies plasmónicas sobre grandes áreas. Se ha puesto mucha atención para solucionar una serie de problemas relacionados con temas diferentes, incluyendo litografía coloidal, deposición de láminas delgadas y procesos de ataque plasma, así como su efecto en la respuesta óptica de la superficie nanoestructurada final. La flexibilidad del método de fabricación permitió adaptar la respuesta espectral de la superficie en relación a las propiedades de la nanoestructura obtenida, con un buen control de reproducibilidad y con la posibilidad de ajustar los parámetros del proceso y de variar los materiales utilizados. Todos estos diferentes aspectos físicos y químicos han sido optimizados y las superficies obtenidas se han empleado como biosensores eficientes. Los resultados principales conseguidos en esta tesis se pueden reagrupar en tres categorías diferentes, estrictamente relacionados y armonizados entre ellos: litografía coloidal, nanofabricación y respuesta óptica, aplicaciones de biosensores.

Litografía coloidal

- Se estudió sistemáticamente la técnica Langmuir-Blodgett para obtener grandes áreas de monocapas coloidales cristalinas. De hecho, esta técnica ofreció un método eficiente y confiable de obtener cristales coloidales bidimensionales con un buen control de formación de defectos y homogeneidad, así como una versatilidad en términos de partículas coloidales (poliestireno de diferentes diámetros y sílica) y sustratos donde transferir las monocapas (capas de polímero, obleas de silicio, vidrio). Las monocapas transferidas en sustratos de silicio se evaluaron observando las isothermas de tensión superficial frente a área, recogiendo medidas de reflectancia y tratando imágenes de microscopía electrónica de barrido.

- La isoterma Langmuir Blodgett relacionada con la formación de monocapas coloidales bidimensionales hechas de partículas de poliestireno se optimizó estudiando los parámetros relacionados con la disolución de partida (porcentaje del solvente, volumen de la disolución).
- El control de la organización de las partículas en términos de cobertura cristalina y dimensiones de los dominios cristalinos se estudió jugando con parámetros relacionados con la subfase (pH, temperatura). La selección de un pH de 6.5 y una temperatura de 22⁰C, durante la formación de la monocapa y durante la transferencia sobre sustratos sólidos, representó un compromiso entre una buena cobertura cristalina y un control más fácil de las condiciones del proceso.
- Los cristales coloidales hechos de partículas inorgánicas (SiO₂) también se estudiaron como máscaras útiles para sustratos más difíciles de nanoestructurar (como silicio y vidrio) debido a su mayor resistencia al proceso de ataque plasma. Se estudió la activación de la superficie de las partículas con HF o HF/H₂O₂ y la funcionalización con un F-silano con el fin de evaluar el efecto de la modificación superficial en la flotabilidad de las partículas y, por consiguiente, en la formación de la monocapa. Las imágenes de microscopía electrónica de barrido mostraron una buena organización de dominios cristalinos para partículas funcionalizadas después de la activación con HF/H₂O₂, pero comparable a la calidad obtenida con partículas no tratadas.

Nanofabricación y respuesta óptica

- El proceso de nanofabricación propuesto está basado en una combinación de técnicas top-down y bottom-up, enfocado en el uso de litografía coloidal y procesos plasma.
- Las monocapas de partículas de SiO₂ no activadas, tras el acondicionamiento por diferentes condiciones de ataque plasma y la deposición secuencial de una capa de oro, dieron lugar a estructuras de silicio con forma controlable y comportamiento óptico característico.
- La superficie plasmónica típica obtenida está hecha por un retículo hexagonal de pilares poliméricos en una capa de oro sobre un sustrato de vidrio. El uso de un sustrato de vidrio hizo posible la correspondencia de la energía de modos plasmónicos en intercaras diferentes y permitió una integración más fácil de sistemas microfluídicos cuando la luz llega desde el propio sustrato.
- La respuesta plasmónica es debida a la contribución de plasmones deslocalizados y localizados, respectivamente relacionados con las diferentes intercaras de la estructura y con la presencia de cavidades dieléctricas. La dependencia entre la respuesta óptica y los parámetros estructurales se investigó experimentalmente por medio de medidas de reflectancia y microscopía superficial (óptica, electrónica de barrido y de fuerzas atómicas).

- Las diferentes combinaciones del grosor de la capa del polímero, del diámetro de las partículas coloidales (400, 500 y 1000 nm) y de la condición de ataque plasma se optimizaron para obtener superficies sensibles, reproducibles y con diferente periodicidad.
- La calibración del proceso de ataque plasma permitió la reducción del diámetro de las partículas dentro de la máscara coloidal y la modificación de la forma del pilar desde una estructura más afilada hacia otra con forma de cono truncado. Las medidas de reflectancia con luz incidente desde el lado del sustrato de vidrio demostraron que una forma afilada del pilar polimérico determina un aumento significativo de la sensibilidad debido a una localización mejorada de la distribución del campo eléctrico cerca de la superficie libre. Este efecto es aún más evidente cuando un anillo de oro está presente en la parte más alta del pilar, ya que actúa como una punta metálica forzando la resonancia del campo eléctrico.
- La capa intermedia de polímero fue el primer paso estudiado para controlar la forma del pilar y la sensibilidad de la superficie final. Esta optimización implicó la selección del grosor de la capa de polímero, el tipo de polímero (ppAA y PMMA) y la técnica de deposición del mismo (PE-CVD y spin coating, respectivamente). En particular, la capa obtenida por spin coating ofreció una deposición más rápida y un mejor control de la reproducibilidad entre series de muestras.
- Se introdujeron varios tratamientos superficiales sucesivos para mejorar el rendimiento de las superficies plasmónicas. Se ha demostrado que un tratamiento térmico a 300⁰C da lugar a más estabilidad a la capa de oro y contribuye a una mejor definición de los motivos superficiales alrededor de la cavidad dieléctrica. Se ha visto que, un ataque por medio de una solución de KI erosiona de manera suave y controlada la capa de oro más superficial, limpiando la superficie de posibles contaminaciones. Un post-tratamiento basado en un ataque de plasma de O₂ contribuye a una mejor limpieza de la superficie y al ajuste de la altura del pilar dentro de la cavidad; también ofrece un control del mojado de la superficie, particularmente útil en vista de una posible funcionalización e interacción con biomoléculas.
- El magnetron sputtering y la evaporación térmica se evaluaron como métodos para la deposición de la capa de oro. Un crecimiento diferente de dicha capa lleva a una diferente estructura de la cavidad, que se refleja en una sensibilidad más alta frente a cambios del índice de refracción cuando se emplea el magnetron sputtering.

Aplicaciones de biosensores

- Las superficies plasmónicas han hecho posible medir variaciones del índice de refracción de 10⁻⁶ RIU, con un rendimiento comparable con respecto a instrumentos SPR de la competencia. La adherencia progresiva de monocapas de polielectrolitos ha permitido reconstruir el decaimiento del campo eléctrico sobre la superficie, relacionado con los

plasmones localizados y deslocalizados. La sensibilidad más alta y la profundidad de penetración inferior del modo localizado son sobre todo prometedoras para detectar pequeñas moléculas.

- Las superficies plasmónicas optimizadas se utilizaron en la instrumentación de resonancia de plasmón superficial denominado Nanoplasmonics (iNPX™, y desarrollada por Plasmore Srl) para la detección específica y multi-analítica del biomarker long pentraxin PTX3 en un ensayo de tipo sandwich, en menos de 30 minutos y con concentraciones clínicamente relevantes (100 ng/ml).
- Las superficies plasmónicas también se adaptaron para la aplicación SERS y se aplicaron en un ensayo bioquímico combinado con el uso de nanopartículas de oro. La mayor intensidad de la señal se debe a los centros de campo electromagnético creados por la interacción entre los plasmones localizados en el sustrato y en las partículas de oro e implicó la detección simultánea y multi-analítica de un biomarker de la leucemia (el gen del tumor de Wilms), un biomarker de la resistencia a los medicamentos y las expresiones génicas de referencia con un límite de detección (2 pM) comparable con ensayos electroquímicos clásicos.

REFERENCES

- [1] S. Enoch, N. Bonod, *Plasmonics: from Basics to Advanced Topics*, Springer Berlin Heidelberg (2007).
- [2] S.A. Maier, *Plasmonics: Fundamentals and Applications*, Springer US (2007).
- [3] *Handbook of Surface Plasmon Resonance*, RCS Publishing (2008).
- [4] M.E. Stewart, C.R. Anderton, L.B. Thompson, J. Maria, S.K. Gray, J.A. Rogers, R.G. Nuzzo, Nanostructured plasmonic sensors, *Chemical Reviews* 108(2) (2008) 494-521.
- [5] J. Homola, *Surface Plasmon Resonance Based Sensors*, Springer Berlin Heidelberg (2006).
- [6] J. Homola, H. Vaisocherova, J. Dostalek, M. Piliarik, Multi-analyte surface plasmon resonance biosensing, *Methods* 37(1) (2005) 26-36.
- [7] M. Couture, S.S. Zhao, J.F. Masson, Modern surface plasmon resonance for bioanalytics and biophysics, *Physical Chemistry Chemical Physics* 15(27) (2013) 11190-11216.
- [8] K.S. McKeating, A. Aube, J.-F. Masson, Biosensors and nanobiosensors for therapeutic drug and response monitoring, *Analyst* 141(2) (2016) 429-449.
- [9] K.R. Rogers, Recent advances in biosensor techniques for environmental monitoring, *Analytica Chimica Acta* 568(1-2) (2006) 222-231.
- [10] C. Situ, J. Buijs, M.H. Mooney, C.T. Elliott, Advances in surface plasmon resonance biosensor technology towards high-throughput, food-safety analysis, *Trac-Trends in Analytical Chemistry* 29(11) (2010) 1305-1315.
- [11] B. Van Dorst, J. Mehta, K. Bekaert, E. Rouah-Martin, W. De Coen, P. Dubruel, R. Blust, J. Robbens, Recent advances in recognition elements of food and environmental biosensors: A review, *Biosensors & Bioelectronics* 26(4) (2010) 1178-1194.
- [12] T. Vo-Dinh, A.M. Fales, G.D. Griffin, C.G. Khoury, Y. Liu, H. Ngo, S.J. Norton, J.K. Register, H.N. Wang, H. Yuan, Plasmonic nanoproboscopes: From chemical sensing to medical diagnostics and therapy, *Nanoscale* 5(21) (2013) 10127-10140.
- [13] Y. Li, X. Liu, Z. Lin, Recent developments and applications of surface plasmon resonance biosensors for the detection of mycotoxins in foodstuffs, *Food Chemistry* 132(3) (2012) 1549-1554.
- [14] S.W. Zeng, D. Baillargeat, H.P. Ho, K.T. Yong, Nanomaterials enhanced surface plasmon resonance for biological and chemical sensing applications, *Chemical Society Reviews* 43(10) (2014) 3426-3452.
- [15] H.A. Atwater, A. Polman, Plasmonics for improved photovoltaic devices, *Nature Materials* 9(3) (2010) 205-213.

References

- [16] K.R. Catchpole, S. Mokkaapati, F. Beck, E.C. Wang, A. McKinley, A. Basch, J. Lee, Plasmonics and nanophotonics for photovoltaics, *Mrs Bulletin* 36(6) (2011) 461-467.
- [17] Q.Q. Gan, F.J. Bartoli, Z.H. Kafafi, Research Highlights on Organic Photovoltaics and Plasmonics, *IEEE Photonics Journal* 4(2) (2012) 620-624.
- [18] S. Pillai, M.A. Green, Plasmonics for photovoltaic applications, *Solar Energy Materials and Solar Cells* 94(9) (2010) 1481-1486.
- [19] D.M. Bagnall, M. Boreland, Photovoltaic technologies, *Energy Policy* 36(12) (2008) 4390-4396.
- [20] S.V. Boriskina, H. Ghasemi, G. Chen, Plasmonic materials for energy: From physics to applications, *Materials Today* 16(10) (2013) 375-386.
- [21] S. Hayashi, T. Okamoto, Plasmonics: visit the past to know the future, *Journal of Physics D-Applied Physics* 45(43) (2012).
- [22] K.A. Willets, R.P. Van Duyne, Localized surface plasmon resonance spectroscopy and sensing, *Annual Review of Physical Chemistry* 58 (2007) 267-297.
- [23] A. Haes, R. Van Duyne, A unified view of propagating and localized surface plasmon resonance biosensors, *Analytical and Bioanalytical Chemistry* 379(7-8) (2004) 920-930.
- [24] W.L. Barnes, Surface plasmon-polariton length scales: a route to sub-wavelength optics, *Journal of Optics a-Pure and Applied Optics* 8(4) (2006) S87-S93.
- [25] S. Roh, T. Chung, B. Lee, Overview of the Characteristics of Micro- and Nano-Structured Surface Plasmon Resonance Sensors, *Sensors* 11(2) (2011) 1565-1588.
- [26] X. Guo, Surface plasmon resonance based biosensor technique: A review, *Journal of Biophotonics* 5(7) (2012) 483-501.
- [27] K.R. Rogers, Principles of affinity-based biosensors, *Molecular Biotechnology* 14(2) (2000) 109-129.
- [28] A.J. Qavi, A.L. Washburn, J.Y. Byeon, R.C. Bailey, Label-free technologies for quantitative multiparameter biological analysis, *Analytical and Bioanalytical Chemistry* 394(1) (2009) 121-135.
- [29] M. Piliarik, H. Vaisocherova, J. Homola, A new surface plasmon resonance sensor for high-throughput screening applications, *Biosensors & Bioelectronics* 20(10) (2005) 2104-2110.
- [30] C. Boozer, G. Kim, S. Cong, H. Guan, T. Londergan, Looking towards label-free biomolecular interaction analysis in a high-throughput format: a review of new surface plasmon resonance technologies, *Current Opinion in Biotechnology* 17(4) (2006) 400-405.
- [31] E. Ouellet, L. Lund, E.T. Lagally, Multiplexed surface plasmon resonance imaging for protein biomarker analysis, *Methods in molecular biology (Clifton, N.J.)* 949 (2013) 473-90.

- [32] J.M. Yao, A.P. Le, S.K. Gray, J.S. Moore, J.A. Rogers, R.G. Nuzzo, Functional Nanostructured Plasmonic Materials, *Advanced Materials* 22(10) (2010) 1102-1110.
- [33] H. Im, A. Lesuffleur, N.C. Lindquist, S.H. Oh, Plasmonic Nanoholes in a Multichannel Microarray Format for Parallel Kinetic Assays and Differential Sensing, *Analytical Chemistry* 81(8) (2009) 2854-2859.
- [34] H.M. Hiep, H. Yoshikawa, E. Tamiya, Interference Localized Surface Plasmon Resonance Nanosensor Tailored for the Detection of Specific Biomolecular Interactions, *Analytical Chemistry* 82(4) (2010) 1221-1227.
- [35] C.T. Campbell, G. Kim, SPR microscopy and its applications to high-throughput analyses of biomolecular binding events and their kinetics, *Biomaterials* 28(15) (2007) 2380-2392.
- [36] O.R. Bolduc, J.F. Masson, Advances in Surface Plasmon Resonance Sensing with Nanoparticles and Thin Films: Nanomaterials, Surface Chemistry, and Hybrid Plasmonic Techniques, *Analytical Chemistry* 83(21) (2011) 8057-8062.
- [37] I. Choi, Y. Choi, Plasmonic nanosensors: Review and prospect, *IEEE Journal on Selected Topics in Quantum Electronics* 18(3) (2012) 1110-1121.
- [38] X. Fan, I.M. White, S.I. Shopova, H. Zhu, J.D. Suter, Y. Sun, Sensitive optical biosensors for unlabeled targets: A review, *Analytica Chimica Acta* 620(1-2) (2008) 8-26.
- [39] X.D. Hoa, A.G. Kirk, M. Tabrizian, Towards integrated and sensitive surface plasmon resonance biosensors: A review of recent progress, *Biosensors & Bioelectronics* 23(2) (2007) 151-160.
- [40] J. Homola, Surface plasmon resonance sensors for detection of chemical and biological species, *Chemical Reviews* 108(2) (2008) 462-493.
- [41] L.B. Sagle, L.K. Ruvuna, J.A. Ruemmele, R.P. Van Duyne, Advances in localized surface plasmon resonance spectroscopy biosensing, *Nanomedicine* 6(8) (2011) 1447-1462.
- [42] S. Unser, I. Bruzas, J. He, L. Sagle, Localized Surface Plasmon Resonance Biosensing: Current Challenges and Approaches, *Sensors* 15(7) (2015) 15684-15716.
- [43] A.P.F. Turner, Biosensors: sense and sensibility, *Chemical Society Reviews* 42(8) (2013) 3184-3196.
- [44] J. Zhao, X.Y. Zhang, C.R. Yonzon, A.J. Haes, R.P. Van Duyne, Localized surface plasmon resonance biosensors, *Nanomedicine* 1(2) (2006) 219-228.
- [45] X. Zhou, T.I. Wong, H.Y. Song, L. Wu, Y. Wang, P. Bai, D.-H. Kim, S.H. Ng, M.S. Tse, W. Knoll, Development of Localized Surface Plasmon Resonance-Based Point-of-Care System, *Plasmonics* 9(4) (2014) 835-844.
- [46] H. Sipova, J. Homola, Surface plasmon resonance sensing of nucleic acids: A review, *Analytica Chimica Acta* 773 (2013) 9-23.

References

- [47] S. Roh, T. Chung, B. Lee, Overview of plasmonic sensors and their design methods, in: B. Culshaw, Y. Liao, A. Wang, X. Bao, X. Fan, L. Zhang (Eds.), *Advanced Sensor Systems and Applications Iv*, Spie-Int Soc Optical Engineering, Bellingham (2010).
- [48] J.N. Anker, W.P. Hall, O. Lyandres, N.C. Shah, J. Zhao, R.P. Van Duyne, Biosensing with plasmonic nanosensors, *Nature Materials* 7(6) (2008) 442-453.
- [49] A. Boltasseva, Plasmonic components fabrication via nanoimprint, *Journal of Optics a-Pure and Applied Optics* 11(11) (2009).
- [50] Z. Fang, X. Zhu, Plasmonics in Nanostructures, *Advanced Materials* 25(28) (2013) 3840-3856.
- [51] T. Chung, S. Lee, E. Song, H. Chun, B. Lee, Plasmonic Nanostructures for Nano-Scale Bio-Sensing, *Sensors* 11(11) (2011) 10907-10929.
- [52] M.A. Otte, B. Sepulveda, W. Ni, J. Perez Juste, L.M. Liz-Marzan, L.M. Lechuga, Identification of the Optimal Spectral Region for Plasmonic and Nanoplasmonic Sensing, *Acs Nano* 4(1) (2010) 349-357.
- [53] P. Strobbia, E. Languirand, B. Cullum, Recent advances in plasmonic nanostructures for sensing: a review, *Optical Engineering* 54(10) (2015).
- [54] S. Scarano, M. Mascini, A.P.F. Turner, M. Minunni, Surface plasmon resonance imaging for affinity-based biosensors, *Biosensors & Bioelectronics* 25(5) (2010) 957-966.
- [55] D. Myszka, SPR biosensors as biophysical research tools, *Faseb Journal* 14(8) (2000) A1511-A1511.
- [56] E.A. Smith, R.M. Corn, Surface plasmon resonance imaging as a tool to monitor biomolecular interactions in an array based format, *Applied Spectroscopy* 57(11) (2003) 320A-332A.
- [57] R.J. Whelan, T. Wohland, L. Neumann, B. Huang, B.K. Kobilka, R.N. Zare, Analysis of bimolecular interactions using a miniaturized surface plasmon resonance sensor, *Analytical Chemistry* 74(17) (2002) 4570-4576.
- [58] C. Genet, T.W. Ebbesen, Light in tiny holes, *Nature* 445(7123) (2007) 39-46.
- [59] A. De Leebeek, L.K.S. Kumar, V. de Lange, D. Sinton, R. Gordon, A.G. Brolo, On-chip surface-based detection with nanohole arrays, *Analytical Chemistry* 79(11) (2007) 4094-4100.
- [60] M. Couture, Y. Liang, H.-P.P. Richard, R. Faid, W. Peng, J.-F. Masson, Tuning the 3D plasmon field of nanohole arrays, *Nanoscale* 5(24) (2013) 12399-12408.
- [61] C. Escobedo, On-chip nanohole array based sensing: A review, *Lab on a Chip - Miniaturisation for Chemistry and Biology* 13(13) (2013) 2445-2463.
- [62] F.J. Garcia-Vidal, L. Martin-Moreno, T.W. Ebbesen, L. Kuipers, Light passing through subwavelength apertures, *Reviews of Modern Physics* 82(1) (2010) 729-787.
- [63] L.S. Live, A. Dhawan, K.F. Gibson, H.P. Poirier-Richard, D. Graham, M. Canva, T. Vo-Dinh, J.F. Masson, Angle-dependent resonance of localized and propagating surface plasmons in

- microhole arrays for enhanced biosensing, *Analytical and Bioanalytical Chemistry* 404(10) (2012) 2859-2868.
- [64] J.F. Masson, M.P. Murray-Methot, L.S. Live, Nanohole arrays in chemical analysis: manufacturing methods and applications, *Analyst* 135(7) (2010) 1483-1489.
- [65] J. Menezes, J. Ferreira, M. Santos, L. Cescato, A. Brolo, Large-Area Fabrication of Periodic Arrays of Nanoholes in Metal Films and Their Application in Biosensing and Plasmonic-Enhanced Photovoltaics, *Advanced Functional Materials* 20(22) (2010) 3918-3924.
- [66] G. Xiang, N. Zhang, X. Zhou, Localized Surface Plasmon Resonance Biosensing with Large Area of Gold Nanoholes Fabricated by Nanosphere Lithography, *Nanoscale Research Letters* 5(5) (2010) 818-822.
- [67] Z.C. Lu, C. Liu, H.Y. Han, Two-dimensional colloidal crystal assisted formation of conductive porous gold films with flexible structural controllability, *Journal of Colloid and Interface Science* 437 (2015) 291-296.
- [68] V. Canpean, S. Astilean, Interaction of light with metallic nanohole arrays, *Nuclear Instruments & Methods in Physics Research Section B-Beam Interactions with Materials and Atoms* 267(2) (2009) 397-399.
- [69] A.G. Brolo, R. Gordon, B. Leathem, K.L. Kavanagh, Surface plasmon sensor based on the enhanced light transmission through arrays of nanoholes in gold films, *Langmuir* 20(12) (2004) 4813-4815.
- [70] H. Im, J.N. Sutherland, J.A. Maynard, S.-H. Oh, Nanohole-Based Surface Plasmon Resonance Instruments with Improved Spectral Resolution Quantify a Broad Range of Antibody-Ligand Binding Kinetics, *Analytical Chemistry* 84(4) (2012) 1941-1947.
- [71] S.H. Lee, K.C. Bantz, N.C. Lindquist, S.H. Oh, C.L. Haynes, Self-Assembled Plasmonic Nanohole Arrays, *Langmuir* 25(23) (2009) 13685-13693.
- [72] J. Martinez-Perdiguero, A. Retolaza, A. Juarros, D. Otaduy, S. Merino, Enhanced Transmission through Gold Nanohole Arrays Fabricated by Thermal Nanoimprint Lithography for Surface Plasmon Based Biosensors, in: R. Walczak, J. Dziuban (Eds.), *26th European Conference on Solid-State Transducers, Eurosens* (2012) 805-808.
- [73] J.P. Monteiro, L.B. Carneiro, M.M. Rahman, A.G. Brolo, M.J.L. Santos, J. Ferreira, E.M. Girotto, Effect of periodicity on the performance of surface plasmon resonance sensors based on subwavelength nanohole arrays, *Sensors and Actuators B-Chemical* 178 (2013) 366-370.
- [74] Y. Pang, C. Genet, T.W. Ebbesen, Optical transmission through subwavelength slit apertures in metallic films, *Optics Communications* 280(1) (2007) 10-15.
- [75] P. Colson, C. Henrist, R. Cloots, Nanosphere Lithography: A Powerful Method for the Controlled Manufacturing of Nanomaterials, *Journal of Nanomaterials* (2013).

References

- [76] D. Maily, Nanofabrication techniques, *European Physical Journal-Special Topics* 172 (2009) 333-342.
- [77] A. Biswas, I.S. Bayer, A.S. Biris, T. Wang, E. Dervishi, F. Faupel, Advances in top-down and bottom-up surface nanofabrication: Techniques, applications & future prospects, *Advances in Colloid and Interface Science* 170(1-2) (2012) 2-27.
- [78] H.H. Gatzel, V. Saile, J. Leuthold, *Micro and Nano Fabrication*, Springer (2015).
- [79] A. Santos, M.J. Deen, L.F. Marsal, Low-cost fabrication technologies for nanostructures: state-of-the-art and potential, *Nanotechnology* 26(4) (2015).
- [80] R.W. Whatmore, Nanotechnology: big prospects for small engineering, *Ingenia online* (9) (2001).
- [81] J.H. Zhang, Y.F. Li, X.M. Zhang, B. Yang, Colloidal Self-Assembly Meets Nanofabrication: From Two-Dimensional Colloidal Crystals to Nanostructure Arrays, *Advanced Materials* 22(38) (2010) 4249-4269.
- [82] S.K. Yang, Y. Lei, Recent progress on surface pattern fabrications based on monolayer colloidal crystal templates and related applications, *Nanoscale* 3(7) (2011) 2768-2782.
- [83] M. Retsch, Z. Zhou, S. Rivera, M. Kappl, X.S. Zhao, U. Jonas, Q. Li, Fabrication of Large-Area, Transferable Colloidal Monolayers Utilizing Self-Assembly at the Air/Water Interface, *Macromolecular Chemistry and Physics* 210(3-4) (2009) 230-241.
- [84] N. Vogel, M. Retsch, C.-A. Fustin, A. del Campo, U. Jonas, Advances in Colloidal Assembly: The Design of Structure and Hierarchy in Two and Three Dimensions, *Chemical Reviews* 115(13) (2015) 6265-6311.
- [85] C. Haynes, R. Van Duyne, Nanosphere lithography: A versatile nanofabrication tool for studies of size-dependent nanoparticle optics, *Journal of Physical Chemistry B* 105(24) (2001) 5599-5611.
- [86] A.Q. Chen, R.L. Miller, A.E. DePrince, A. Joshi-Imre, E. Shevchenko, L.E. Ocola, S.K. Gray, U. Welp, V.K. Vlasko-Vlasov, Plasmonic Amplifiers: Engineering Giant Light Enhancements by Tuning Resonances in Multiscale Plasmonic Nanostructures, *Small* 9(11) (2013) 1939-1946.
- [87] N. Vogel, C.K. Weiss, K. Landfester, From soft to hard: the generation of functional and complex colloidal monolayers for nanolithography, *Soft Matter* 8(15) (2012) 4044-4061.
- [88] M.A. Wood, Colloidal lithography and current fabrication techniques producing in-plane nanotopography for biological applications, *Journal of the Royal Society Interface* 4(12) (2007) 1-17.
- [89] F. Burmeister, C. Schafle, T. Matthes, M. Bohmisch, J. Boneberg, P. Leiderer, Colloid monolayers as versatile lithographic masks, *Langmuir* 13(11) (1997) 2983-2987.

- [90] H.T. Yang, N. Gozubenli, Y. Fang, P. Jiang, Generalized Fabrication of Monolayer Nonclose-Packed Colloidal Crystals with Tunable Lattice Spacing, *Langmuir* 29(25) (2013) 7674-7681.
- [91] Z.Y. Cai, Y.J. Liu, E.S.P. Leong, J.H. Teng, X.M. Lu, Highly ordered and gap controllable two-dimensional non-close-packed colloidal crystals and plasmonic-photonic crystals with enhanced optical transmission, *Journal of Materials Chemistry* 22(47) (2012) 24668-24675.
- [92] P. Jiang, Large-scale fabrication of periodic nanostructured materials by using hexagonal non-close-packed colloidal crystals as templates, *Langmuir* 22(9) (2006) 3955-3958.
- [93] Y. Lei, S. Yang, M. Wu, G. Wilde, Surface patterning using templates: concept, properties and device applications, *Chemical Society Reviews* 40(3) (2011) 1247-1258.
- [94] S. Yang, S. Jang, D. Choi, S. Kim, H. Yu, Nanomachining by colloidal lithography, *Small* 2(4) (2006) 458-475.
- [95] X. Ye, L. Qi, Two-dimensionally patterned nanostructures based on monolayer colloidal crystals: Controllable fabrication, assembly, and applications, *Nano Today* 6(6) (2011) 608-631.
- [96] R. Aveyard, J.H. Clint, D. Nees, V.N. Paunov, Compression and structure of monolayers of charged latex particles at air/water and octane/water interfaces, *Langmuir* 16(4) (2000) 1969-1979.
- [97] M. Yoldi, C. Arcos, B. Paulke, R. Sirera, W. Gonzalez-Vinas, E. Gornitz, On the parameters influencing the deposition of polystyrene colloidal crystals, *Materials Science & Engineering C-Biomimetic and Supramolecular Systems* 28(7) (2008) 1038-1043.
- [98] Z. Li, J. Wang, Y. Song, Self-assembly of latex particles for colloidal crystals, *Particuology* 9(6) (2011) 559-565.
- [99] G. Liu, Z. Wang, Y. Ji, Influence of growth parameters on the fabrication of high-quality colloidal crystals via a controlled evaporation self-assembly method, *Thin Solid Films* 518(18) (2010) 5083-5090.
- [100] M. Szekeres, O. Kamalin, R.A. Schoonheydt, K. Wostyn, K. Clays, A. Persoons, I. Dekany, Ordering and optical properties of monolayers and multilayers of silica spheres deposited by the Langmuir-Blodgett method, *Journal of Materials Chemistry* 12(11) (2002) 3268-3274.
- [101] A. Gil, F. Guitian, Formation of 2D colloidal crystals by the Langmuir-Blodgett technique monitored in situ by Brewster angle microscopy, *Journal of Colloid and Interface Science* 307(1) (2007) 304-307.
- [102] P. Masse, S. Ravaine, The Langmuir-Blodgett technique: A powerful tool to elaborate multilayer colloidal crystals, *Colloids and Surfaces a-Physicochemical and Engineering Aspects* 270 (2005) 148-152.
- [103] E. Sheppard, Tcheurek.N, MONOLAYER STUDIES .4. SURFACE FILMS OF EMULSION LATEX PARTICLES, *Journal of Colloid and Interface Science* 28(3-4) (1968).

References

- [104] J. Kumaki, Monolayer of polystyrene monomolecular particles on a water surface studied by Langmuir-type film balance and transmission electron microscopy, *Macromolecules* 21(3) (1988) 749-755.
- [105] T.N. Hunter, G.J. Jameson, E.J. Wanless, D. Dupin, S.P. Armes, Adsorption of Submicrometer-Sized Cationic Sterically Stabilized Polystyrene Latex at the Air-Water Interface: Contact Angle Determination by Ellipsometry, *Langmuir* 25(6) (2009) 3440-3449.
- [106] W. Ruan, Z. Lu, N. Ji, C. Wang, B. Zhao, J. Zhang, Facile fabrication of large area polystyrene colloidal crystal monolayer via surfactant-free Langmuir-Blodgett technique, *Chemical Research in Chinese Universities* 23(6) (2007) 712-714.
- [107] M. Bardosova, M.E. Pemble, I.M. Povey, R.H. Tredgold, The Langmuir-Blodgett Approach to Making Colloidal Photonic Crystals from Silica Spheres, *Advanced Materials* 22(29) (2010) 3104-3124.
- [108] K.U. Fulda, D. Piecha, B. Tieke, H. Yarmohammadipour, Monolayer characteristics of monodisperse core shell latex particles prepared by soap-free emulsion copolymerization, in: H.J. Jacobasch (Ed.), *Interfaces, Surfactants and Colloids in Engineering* (1996) 178-183.
- [109] K.U. Fulda, B. Tieke, Monolayers of mono- and bidisperse spherical polymer particles at the air/water interface and Langmuir-Blodgett layers on solid substrates, *Supramolecular Science* 4(3-4) (1997) 265-273.
- [110] K.U. Fulda, A. Kampes, L. Krasemann, B. Tieke, Self-assembled mono- and multilayers of monodisperse cationic and anionic latex particles, *Thin Solid Films* 327 (1998) 752-757.
- [111] A. Detrich, A. Deak, E. Hild, A. Kovacs, Z. Horvolgyi, Langmuir and Langmuir-Blodgett Films of Bidisperse Silica Nanoparticles, *Langmuir* 26(4) (2010) 2694-2699.
- [112] S. Reculosa, R. Perrier-Cornet, B. Agricole, V. Heroguez, T. Buffeteau, S. Ravaine, Langmuir-Blodgett films of micron-sized organic and inorganic colloids, *Physical Chemistry Chemical Physics* 9(48) (2007) 6385-6390.
- [113] Q.J. Guo, X.W. Teng, S. Rahman, H. Yang, Patterned Langmuir-Blodgett films of monodisperse nanoparticles of iron oxide using soft lithography, *Journal of the American Chemical Society* 125(3) (2003) 630-631.
- [114] K. Muramatsu, M. Takahashi, K. Tajima, K. Kobayashi, Two-dimensional assemblies of colloidal SiO₂ and TiO₂ particles prepared by the Langmuir-Blodgett technique, *Journal of Colloid and Interface Science* 242(1) (2001) 127-132.
- [115] L. Nagy, N. Abraham, O. Sepsi, E. Hild, D. Cot, A. Ayrál, Z. Horvolgyi, Complex Langmuir-Blodgett Films of SiO₂ and ZnO Nanoparticles with Advantageous Optical and Photocatalytical Properties, *Langmuir* 24(21) (2008) 12575-12580.

- [116] A. Valsesia, Fabrication of nanostructured surfaces for the development of advanced biointerfaces, PhD thesis (2007).
- [117] S. Giudicatti, Optical response of nanostructured surfaces supporting plasmonic resonances: towards a sensitive tool for biomolecular detection, PhD thesis (2011).
- [118] A.C. Jones, M.L. Hitchman, Chemical vapour deposition: precursors, processes and applications, Royal Society of Chemistry (2009).
- [119] L. Martinu, O. Zabeida, J.E. Klemberg-Sapieha, Plasma-enhanced chemical vapor deposition of functional coatings, Handbook of Deposition Technologies for Films and Coatings (2010) 394-467.
- [120] <http://www.microchem.com/>.
- [121] <http://www.biolinscientific.com/ksvnima/>.
- [122] E.J.W. Verwey, J.T.G. Overbeek, J.T.G. Overbeek, Theory of the stability of lyophobic colloids, Courier Corporation (1999).
- [123] H. Sholtmeijer, The Langmuir Blodgett behavior and film formation of methacrylate latex particle monolayers, PhD thesis (2005).
- [124] <https://folio.brighton.ac.uk/user/lc355/dlvo-theory>.
- [125] P.M. Martin, Handbook of deposition technologies for films and coatings: science, applications and technology, William Andrew (2009).
- [126] D.M. Mattox, Handbook of physical vapor deposition (PVD) processing, William Andrew (2010).
- [127] D.B. Murphy, Fundamentals of light microscopy and electronic imaging, John Wiley & Sons (2002).
- [128] B. Voigtländer, Scanning probe microscopy: Atomic force microscopy and scanning tunneling microscopy, Springer (2015).
- [129] M. Ohring, Materials science of thin films, Academic press (2001).
- [130] R.F. Egerton, Physical principles of electron microscopy: an introduction to TEM, SEM, and AEM, Springer Science & Business Media (2006).
- [131] <https://www.fei.com/>.
- [132] H.R. Verma, Atomic and nuclear analytical methods, Springer (2007).
- [133] Y. Yuan, T.R. Lee, Contact angle and wetting properties, Surface science techniques, Springer (2013).
- [134] <http://www.jawoollam.com>.
- [135] J.B. Bates, Fourier transform spectroscopy, Computers & Mathematics with Applications 4(2) (1978) 73-84.
- [136] <http://www.plasmore.com/>.

References

- [137] B. Bottazzi, L. Fornasari, A. Frangolho, S. Giudicatti, A. Mantovani, F. Marabelli, G. Marchesini, P. Pellacani, R. Therisod, A. Valsesia, Multiplexed label-free optical biosensor for medical diagnostics, *Journal of Biomedical Optics* 19(1) (2014).
- [138] E. Le Ru, P. Etchegoin, *Principles of Surface-Enhanced Raman Spectroscopy: and related plasmonic effects*, Elsevier (2008).
- [139] S. Picciolini, D. Mehn, C. Morasso, R. Vanna, M. Bedoni, P. Pellacani, G. Marchesini, A. Valsesia, D. Prosperi, C. Tresoldi, F. Ciceri, F. Gramatica, Polymer Nanopillar - Gold Arrays as Surface-Enhanced Raman Spectroscopy Substrate for the Simultaneous Detection of Multiple Genes, *Acs Nano* 8(10) (2014) 10496-10506.
- [140] N.B. Vargaftik, B.N. Volkov, L.D. Voljak, International tables of the surface tension of water, *Journal of Physical and Chemical Reference Data* 12(3) (1983) 817-820.
- [141] S. Giudicatti, A. Valsesia, F. Marabelli, P. Colpo, F. Rossi, Plasmonic resonances in nanostructured gold/polymer surfaces by colloidal lithography, *Physica Status Solidi a-Applications and Materials Science* 207(4) (2010) 935-942.
- [142] S. Giudicatti, F. Marabelli, A. Valsesia, P. Pellacani, P. Colpo, F. Rossi, Interaction among plasmonic resonances in a gold film embedding a two-dimensional array of polymeric nanopillars, *Journal of the Optical Society of America B-Optical Physics* 29(7) (2012) 1641-1647.
- [143] S. Giudicatti, F. Marabelli, P. Pellacani, Field Enhancement by Shaping Nanocavities in a Gold Film, *Plasmonics* 8(2) (2013) 975-981.
- [144] E. Magrini, A. Mantovani, C. Garlanda, The Dual Complexiy of PTX3 in Health and Disease: A Balancing Act?, *Trends in Molecular Medicine* 22(6) (2016) 497-510.
- [145] K. Daigo, A. Inforzato, I. Barajon, C. Garlanda, B. Bottazzi, S. Meri, A. Mantovani, Pentraxins in the activation and regulation of innate immunity, *Immunological Reviews* 274(1) (2016) 202-217.
- [146] B. Bottazzi, A. Inforzato, M. Messa, M. Barbagallo, E. Magrini, C. Garlanda, A. Mantovani, The pentraxins PTX3 and SAP in innate immunity, regulation of inflammation and tissue remodelling, *Journal of Hepatology* 64(6) (2016) 1416-1427.
- [147] A. Mantovani, C. Garlanda, A. Doni, B. Bottazzi, Pentraxins in innate immunity: From C-reactive protein to the long pentraxin PTX3, *Journal of Clinical Immunology* 28(1) (2008) 1-13.
- [148] N.S. Jenny, A.M. Arnold, L.H. Kuller, R.P. Tracy, B.M. Psaty, Associations of Pentraxin 3 With Cardiovascular Disease and All-Cause Death The Cardiovascular Health Study, *Arteriosclerosis Thrombosis and Vascular Biology* 29(4) (2009) 594-599.
- [149] R. Latini, L. Gullestad, S. Masson, S.H. Nymo, T. Ueland, I. Cuccovillo, M. Vardal, B. Bottazzi, A. Mantovani, D. Lucci, N. Masuda, Y. Sudo, J. Wikstrand, G. Tognoni, P. Aukrust, L. Tavazzi, R.

Investigators Controlled, G.I.-H.F.G.-H. Trial, Pentraxin-3 in chronic heart failure: the CORONA and GISSI-HF trials, *European Journal of Heart Failure* 14(9) (2012) 992-999.

[150] G. Vilahur, L. Badimon, Biological actions of pentraxins, *Vascular Pharmacology* 73 (2015) 38-44.

[151] M. Infante, P. Allavena, C. Garlanda, M. Nebuloni, E. Morengi, D. Rahal, M. Roncalli, S. Cavuto, S. Pesce, M. Monari, S. Valaperta, A. Montanelli, D. Solomon, E. Bottoni, V. Errico, E. Voulaz, M. Bossi, G. Chiesa, E. Passera, A. Mantovani, M. Alloisio, Prognostic and diagnostic potential of local and circulating levels of pentraxin 3 in lung cancer patients, *International Journal of Cancer* 138(4) (2016) 983-991.

[152] M. Presta, M. Camozzi, G. Salvatori, M. Rusnati, Role of the soluble pattern recognition receptor PTX3 in vascular biology, *Journal of Cellular and Molecular Medicine* 11(4) (2007) 723-738.

[153] B. Sharma, M.F. Cardinal, S.L. Kleinman, N.G. Greeneltch, R.R. Frontiera, M.G. Blaber, G.C. Schatz, R.P. Van Duyne, High-performance SERS substrates: Advances and challenges, *Mrs Bulletin* 38(8) (2013) 615-624.

[154] F.J. Sharom, The P-glycoprotein multidrug transporter, *Essays in Biochemistry: Abc Transporters* 50 (2011) 161-178.

[155] B.C. Shaffer, J.-P. Gillet, C. Patel, M.R. Baer, S.E. Bates, M.M. Gottesman, Drug resistance: Still a daunting challenge to the successful treatment of AML, *Drug Resistance Updates* 15(1-2) (2012) 62-69.

[156] J.L. Jorgensen, S.S. Chen, Monitoring of Minimal Residual Disease in Acute Myeloid Leukemia: Methods and Best Applications, *Clinical Lymphoma Myeloma and Leukemia* (2011) S49-S53.

[157] G.J. Schuurhuis, H.J. Broxterman, G.J. Ossenkoppele, J.P.A. Baak, C.A. Eekman, C.M. Kuiper, N. Feller, T.H.M. Vanheijningen, E. Klumper, R. Pieters, J. Lankelma, H.M. Pinedo, Functional multidrug resistance phenotype associated with combined overexpression of Pg-p/MDR1 and MRP together with 1-beta-D-arabinofuranosylcytosine sensitivity may predict clinical response in acute myeloid leukemia, *Clinical Cancer Research* 1(1) (1995) 81-93.

[158] F. Floris, C. Figus, L. Fornasari, M. Patrini, P. Pellacani, G. Marchesini, A. Valsesia, F. Artizzu, D. Marongiu, M. Saba, Optical Sensitivity Gain in Silica-Coated Plasmonic Nanostructures, *The Journal of Physical Chemistry Letters* 5(17) (2014) 2935-2940.

[159] M. Manso Silván, J.P. Garcia Ruiz, A. Valsesia, P. Pellacani, M.A. Parracino, G. Marchesini, Resina negativa fotosensible para escritura directa de estructuras, Patente española No. ES-2571177 B1 (2014).